Avionics and Control System Development for Mid-Air Rendezvous of Two Unmanned Aerial Vehicles

by

Sanghyuk Park

Submitted to the Department of Aeronautics and Astronautics
in partial fulfillment of the requirements for the degree of

Doctor of Philosophy in Aeronautics and Astronautics

at the

MASSACHUSETTS INSTITUTE OF TECHNOLOGY

February 2004

Author .....
Department of Aeronautics and Astronautics
November, 2003

Certified by .....
John J. Deyst
Professor of Aeronautics and Astronautics
Thesis Supervisor

Certified by .....
Jonathan P. How
Associate Professor of Aeronautics and Astronautics
Thesis Supervisor

Certified by .....
James D. Paduano
Principal Research Engineer of Aeronautics and Astronautics
Thesis Supervisor

Certified by .....
Brent D. Appleby
Principal Member of Technical Staff at Draper Laboratory
Thesis Supervisor

Accepted by .....
Edward M. Greitzer
H.N. Slater Professor of Aeronautics and Astronautics
Chairman, Committee on Graduate Students

Avionics and Control System Development for Mid-Air Rendezvous of Two Unmanned Aerial Vehicles

by

Sanghyuk Park

Submitted to the Department of Aeronautics and Astronautics
on November, 2003, in partial fulfillment of the
requirements for the degree of
Doctor of Philosophy in Aeronautics and Astronautics

Abstract

A flight control system was developed to achieve mid-air rendezvous of two unmanned aerial vehicles (UAVs) as a part of the Parent Child Unmanned Aerial Vehicle (PCUAV) project at MIT and the Draper Laboratory.

A lateral guidance logic was developed for tightly tracking a desired flight path. The guidance logic is derived from geometric and kinematic properties, and has been demonstrated to work better than the conventional aircraft guidance method in waypoint navigation.

A simple, low-order attitude estimation was developed that combines aircraft kinematics, GPS and low-quality rate gyros. It is demonstrated in simulation that the performance of the proposed method is as good as other advanced complex methods when the aircraft bank angle is relative small(<40 degrees).

The end-game control strategy for the final phase of the rendezvous was also developed, using proportional navigation guidance in conjunction with an optical sensor. The associated miss distance was analyzed with regard to the wind effect and initial conditions.

A series of flight tests was performed using two UAVs which were built as a part of the project. It was demonstrated that each individual aircraft can follow a desired flight path within a position accuracy of 2 meters (based on sensor data) while also tracking the air speed command to within 1 m/s. At the time of this thesis writing, it has been demonstrated that the developed control system can bring the two UAVs from any arbitrary initial positions into a configuration of a tight formation flight, where one vehicle trails the other with a commanded separation of 12 meters while maintaining the relative position error within 2 meters in both horizontal and vertical directions for 85% of the flight time.

Thesis Supervisor: John J. Deyst
Title: Professor of Aeronautics and Astronautics

Thesis Supervisor: Jonathan P. How
Title: Associate Professor of Aeronautics and Astronautics

Thesis Supervisor: James D. Paduano
Title: Principal Research Engineer of Aeronautics and Astronautics

Thesis Supervisor: Brent D. Appleby

Title: Principal Member of Technical Staff at Draper Laboratory

Acknowledgments

I would like to express my sincere gratitude to the following people. Without them all the excitement that I had in this project would have been impossible.

I would like to thank Professor John J. Deyst for giving me the opportunity to work on this exciting team project, and for his guidance and consistent motivation throughout my past five years at MIT. Thank you to Professor Jonathan P. How for his advice and help, especially for guiding me to think through the trajectory-tracking logic from different points of view. Thanks to his help I was able to come up with a right explanation for that. I would like to thank Professor James D. Paduano for his cordial concern and advice from the countless meetings, and also specifically for guiding me in organizing the thesis and the defense. Thank you to Dr. Brent D. Appleby. I appreciate his advice and support throughout the project, and for introducing this exciting project to MIT from Draper Laboratory.

I would like to thank Sean George, Vladislav Gavrilets, and Kyungyeol Song, who provided many valuable insights through many discussions. I would like to thank Donald Weiner and Richard Perdichizzi, who taught me how to use many interesting machines in the department work shop and helped me doing lots of experiments throughout the project. Thank you to Ruane Crummett and Mitch Buckley, our pilots, who saved our aircraft many, many times.

I would like to thank the students who have been in the project. It was a wonderful thing to have a lab-mate like Damien Jourdan for the last three years. I appreciate the friendship with Thomas Jones, who also shared many discussions and ideas throughout the project. Thank you, Francois Urbain and Jason Kepler, who built our amazing two aircraft, for their exceptional friendship. Thank you, Richard Poutrel, who worked on the communication parts and also played some tennis and soccer together. Thank you, Sarah Saleh for creating warm and friendly atmosphere in the lab during her stay. I appreciate the friendship from Alexander Omelchenko who has been with me for the last five years in the project. I would like to thank Hyungil Ahn, Anand Srinivas, Damian Toohey and Joshua Torgerson, who recently joined the project, but we had lots of fun together. I would like to thank other friends at school. Thank you Simon, Xueen, Taehong and Hyuntae.

I would like to thank my father-in-law, who showed consistent interest in what I was

doing here. Thank you, my mother-in-law, who shared many interesting and funny stories from time to time. And thank you, my sister-in-law for her cordial concern and friendly support.

I owe infinite gratitude to my family in Korea. Thank you, my Mom and Dad, and my Uncle and Aunt for their unconditional love and support. Thank you, my two brothers, Jihyuk and Jeoung-hyuck hyung for their concern and support.

Finally I would like to thank the most important person in my life, my lovely wife Jiyoon, for her exceptional understanding, concern, and support. I love you.

Contents

List of Figures

List of Tables

Chapter 1

Introduction and Overview

1.1 Background and Objective

Recently, there has been an increasing interest in solving various kinds of multiple aircraft rendezvous problems. Many valuable capabilities including aerial refueling are enabled by the rendezvous technologies. Currently aerial refueling is done manually and requires well-trained pilots, but the Defense Advanced Research Projects Agency (DARPA) has a vision that by 2008 autonomous refueling technology will be developed and applied to unmanned aerial vehicles (UAVs) or unmanned combat aerial vehicles (UCAVs) [23, Kinzer & Olinger]. Such a capability will enable greater time on station and provide greater utility and new missions for UAVs.

Formation flight is another example that requires rendezvous capability. NASA Dryden Flight Research Center has performed flight testing of autonomous formation flight of two F/A-18 aircraft, for the purpose of reducing the induced drag of the trailing aircraft. It is reported [29, Lavretsky] that the flight test experiments showed the potential for reducing drag, improving fuel consumption, and increasing range 15 to 20 percent in the trailing aircraft.

The aerial rendezvous between a large UAV such as Global Hawk or Predator and small/agile UAVs enables the following scenario: A large UAV carries small UAVs to a distant mission site and deploys them for *close-in* surveillance on the mission site. When small UAVs with little range or endurance run low on fuel, they rendezvous with the large UAV for refueling so as to continue performing the close-in surveillance mission. In other words, the *sustained close-in surveillance from stand-off distance* can be achieved. Furthermore,

after the mission is over the large UAV can retrieve the small UAVs and carry them home as a single unit.

There has been an increasing awareness of the need for the *close-in* surveillance capability instead of the traditional high-altitude, high-zoom surveillance method. Recent experience has indicated that the high tech Intelligence-Surveillance-Reconnaissance (ISR) from high altitude aircraft are dependent on weather conditions for optical and infrared imagery and are sometimes thwarted by low-tech, asymmetric adversaries such as overhead-cover concealment, decoys, foliage, underground facilities .

Motivated by these issues and also from the notion that the limitations of small UAVs (low range and endurance) and large UAVs (high cost, low bandwidth) can be mitigated by the combination of these two, a team was assembled at MIT, based on the need for the study of such a system. The four-year-project, funded by Draper Laboratory as part of the MIT/Draper Technology Development Partnership, was initiated in September, 1998. The project was named Parent Child Unmanned Aerial Vehicle (PCUAV) to describe the combination of the large and small UAVs [1]. The objective of the project was to design, develop, and test prototypes of this system-of-systems that coordinates cooperative, unmanned vehicles, having interfaces with recovery and communications systems on the ground.

During the concept study, performed in the first year of the project, the project team developed the PCUAV system concept which is a 3-tiered system with a Parent vehicle at the highest level, Mini vehicles at the middle or the ground level, and micro aerial vehicles (MAV) or micro sensors at the ground level. One typical potential mission scenario of the PCUAV system is shown in Figure 1-1, where the Parent vehicle carries the system and deploys the second and the third layer components. The Mini vehicles play the role of close-in surveillance or communication relays between the Parent vehicle and the MAVs or micro sensors. In this diagram the low range and endurance Mini vehicles are refurbished by the Parent vehicle through aerial refueling, for sustained presence of the Mini vehicles at the mission site. Thus, the PCUAV system provides *sustained close-in surveillance from standoff distances*, with rendezvous the key enabling technology. For this reason the air rendezvous has been one of the main focuses of the project.

The team constructed one large and a number of small UAVs to play the roles of the surrogate Parent and Mini vehicles. Then, the avionics for the airplanes were built, and the

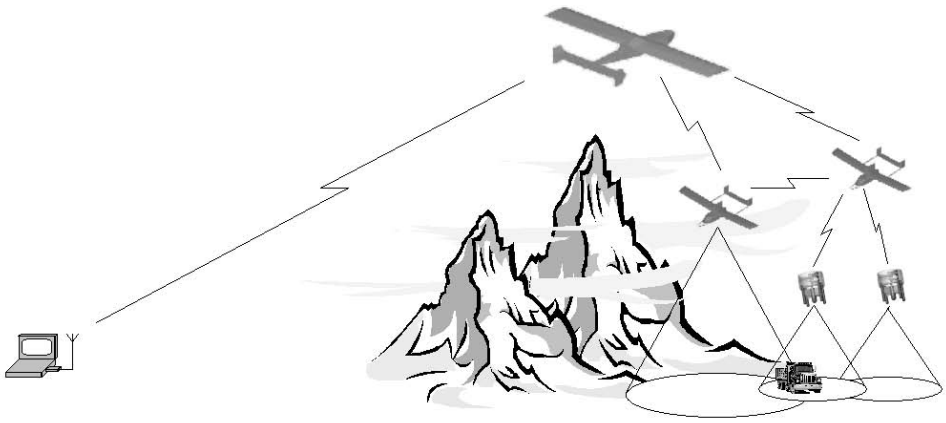

Figure 1-1: PCUAV Concept : Sustained close-in surveillance from standoff distances

controllers, estimators, and guidance planning algorithms for rendezvous were developed and implemented.

The objective of this thesis is to report the author's contributions to the control system development and the flight tests for mid-air rendezvous of two small UAVs.

Typically with manned vehicles, crew *survivability* is of prime importance [31, Luers], making these vehicles more expensive through the need for high-cost, high-quality redundant hardware components. However, in the case of unmanned vehicles, survivability can be traded off with the cost. Increased survivability is only desirable to the extent that it does not significantly drive up the cost [31, Luers]. The use of inexpensive commercial-off-the-shelf components in this project indicates the feasibility of a new class of unmanned military air vehicles, which are small, inexpensive, and attritable.

1.2 Approach and Challenges

The philosophy of the project team's approach to the rendezvous problem is to have the higher bandwidth (agile) vehicle take on challenging tasks and use control law sophistication instead of costly instrumentation. The rendezvous problem was approached by dividing the whole procedure into two phases - Phase I and Phase II. They are depicted in Figure 1-2.

Phase I is the first phase of rendezvous, where the Mini UAV approaches the Parent UAV to within 20 meters, from any initial feasible positions of the two vehicles, and flies in formation behind the Parent using stand-alone GPS as the primary navigation sensor. The

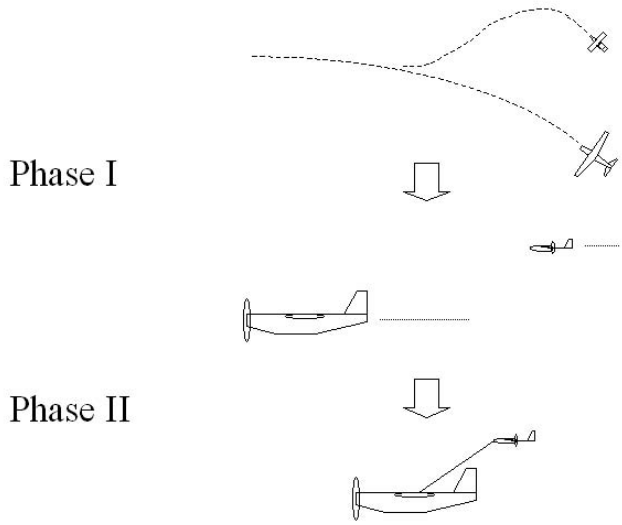

Figure 1-2: Phase I and Phase II of Rendezvous

technical challenges in Phase I are :

- A reasonable flight path should be generated for each vehicle to follow.
- Each vehicle should be controlled and guided on the desired trajectory as tightly as possible, for rendezvous and for the formation flight at the end of this phase.

In typical practice of GPS waypoint guidance [47, Whalley et.al], [36, DeBitetto et.al.] a series of waypoints are assigned for an aircraft to pass through, and the vehicle is controlled to track the straight line defined by the two local waypoints. In doing so, linear controllers are commonly used to correct the cross-track error - the separation distance between the vehicle and the straight line. This method is insufficient for Phase I because (a) desired trajectories in Phase I involves curved lines (See Chapter 3. This is inevitable if rendezvous is to be done in a confined area, especially for demonstration.) and (b) linear controllers cannot by nature perform well in following curved(=nonlinear) trajectories.

Phase II brings two UAVs even closer, to within a few meters, for refueling or docking. Additional sensor information is necessary for more accurate control in this phase. The technical challenges in Phase II are :

- Accurate sensing and estimation
- Tight control and guidance

1.3 Research Contributions

The following sections briefly summarize the research contributions of the author to successful completion of the project.

1.3.1 Theoretical Contributions

- In order to satisfy the requirement of tightly tracking a given trajectory, a new guidance logic was developed. This thesis presents the properties of this method and reports the comparison analysis with the traditional aircraft guidance method.

- An effective and simple, low-order attitude estimation method was developed that combines aircraft kinematics, GPS, and information from low quality rate gyros. The performance of this simple algorithm is as good as much more complex estimation algorithms when the vehicle bank angle remains within ± 40 degrees.

- A control/guidance strategy for the autonomous docking of the two UAVs (Phase II) is proposed. This thesis presents an approach to exploit additional control surfaces for the fast tracking capability and reports the associated miss distance analysis.

1.3.2 Experimental Contributions

- In a series of flight tests, the team demonstrated that each aircraft can be controlled with the RMS position error less than 1.6 meters in both the altitude and the lateral directions, while also tracking the airspeed command with the RMS error of 0.7 m/s, under the nominal wind condition of $5(\pm 1)$ m/s, which is more than 20 percent of nominal flight speed.

- The team successfully demonstrated the Phase I aerial rendezvous. It was shown that from any arbitrary initial positions the two vehicles followed flight paths generated by a planning algorithm, rendezvous, and then the two UAVs performed a tight formation flight with the Mini vehicle in train behind the Parent. The two aircraft held the relative separation command of 12 meters, with the RMS relative position errors of 1.4 meters in both horizontal and vertical directions. Figure 1-3 shows a photo of the two demonstration UAVs, taken during the formation flight at the end of Phase I flight demonstration. At the time of this thesis writing a total of 6 out of 7 trials of

Figure 1-3: Formation Flight during Phase I Flight Test (July 2002)

the Phase I flight tests were successful. There was one case where the procedure had to be aborted due to a malfunction of the communication link.

1.4 Thesis Outline

Chapter 2 describes the experimental setup. It first introduces the two demonstration UAVs - Mini and Parent - constructed in the project. It next gives a brief description on the onboard avionics, built out of off-the-shelf components. It then gives a brief report on the dynamic modeling of the two UAVs and the inner-loop controllers implemented on the vehicles.

Chapter 3 discusses the guidance logic for trajectory following. It reports the properties of this method and the comparison with the traditional aircraft guidance method.

Chapter 4 covers the simple and low-order attitude estimation method that combines the aircraft kinematics with GPS and low quality inertial sensors. It presents the properties of this approach and the comparison with a more complex method which is not based on

the aircraft kinematics.

Chapter 5 describes the control/guidance strategy for Phase II rendezvous. It shows how the additional optical sensor is combined with the avionics and how the additional control surfaces are used for the Phase II mid-air rendezvous. The associated miss distance analysis with regard to the wind effect is also reported.

Chapter 6 reports the flight test results. It first gives the individual flight test results for each aircraft and then provides the Phase I flight test results.

Chapter 7 summarizes the thesis with the future recommendations.

Chapter 2

Experimental Setup

This chapter gives an overview of the experimental setup, which includes demonstration vehicles, avionics, vehicle dynamic modeling, and inner-loop controllers.

2.1 Demonstration Vehicles

The purpose of this section is to introduce the two demonstration UAVs - Mini and Parent, and to point out some unique vehicle features. A detailed discussion on the vehicle design and construction can be found in the theses by Francois Urbain [45] and Jason Kepler [26].

2.1.1 Mini - Child Vehicle

The team constructed a demonstration Mini aircraft as a test vehicle to represent the mid-sized UAV, which is the second layer element in the three-tiered PCUAV system. Figure 2-1 is a picture of the Mini vehicle. The Mini vehicle has a pusher propeller propulsion system because the Mini trails the parent vehicle from behind during the air rendezvous procedure.

One of the nonconventional feature of the Mini UAV is the vertical fin on top of the fuselage near the center of gravity and its control surface which is the trailing edge portion of the fin. This can be noticed in the picture. This control surface was named "sideways control surface". The benefit of the additional control surface is its ability to generate direct side force on the vehicle, without having to bank or yaw the entire vehicle. This feature was envisioned to be beneficial during the rendezvous Phase II. But it turned out from an analysis that for this type of control surface to be effective the size should be larger than the one that was built. With the current fin size, it is estimated that it produces 0.1 g of

Figure 2-1: Mini Child Vehicle

acceleration when its control surface is deflected by 20 degrees. Though the amount of the acceleration generated from this control surface is small, it was designed to be used in the Phase II of rendezvous to augment the lateral acceleration on top of the vehicle banking. How it is included is described in Chapter 5.

For a similar reason, the Mini vehicle is equipped with a large surface area of flaperons. The flaperon on each side of the wing starts close to the fuselage and extends close to the wing tip. In differential mode they act as ailerons, and in collective mode they act as flaps. The flap mode is used in the Phase II of the rendezvous. How they are included is described in Chapter 5.

The dimensions for the Mini vehicle and other basic features are summarized in Table 2.1. A modestly high aspect ratio of 9.1 was chosen for aerodynamic efficiency. The fuselage was constructed such that the entire upper surface can be opened for easy installation of the avionics box. The vehicle was constructed mainly out of carbon fiber and balsa.

Total Weight	9.1 kg	Empty Weight	6.8 kg
Wing Span	2.54 m	Wing Area	0.71 sq.m
Wind Chord	0.28 m	Fuselage Dim.	27 x 18 x 101 cm
Height	0.53 m	Length	1.6 m
Dihedral	4 deg.	Tail Volume	0.44
Speed	18∼30 m/s	Flight Time	20 min.
Engine	O.S. 0.91 cu.in FX	Airfoil	GM-15

Table 2.1: Properties of Mini Vehicle

2.1.2 Outboard Horizontal Stabilizer(OHS) - Parent Vehicle

A very unconventional airplane configuration was chosen for the Parent UAV. Figure 2-2 shows a picture of the demonstration Parent UAV flying. It has two horizontal tail surfaces

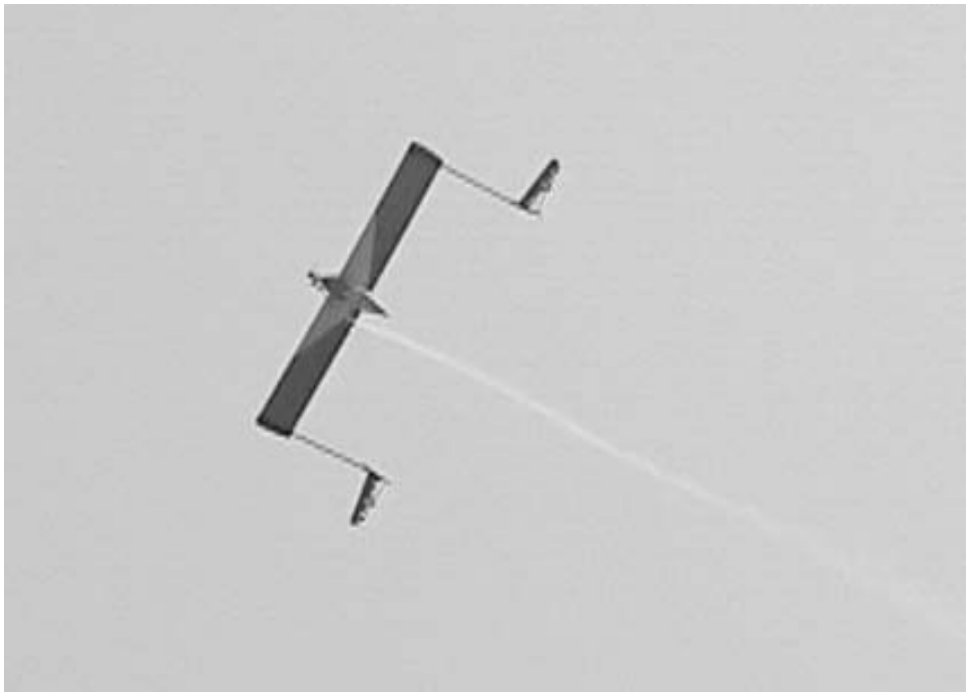

Figure 2-2: Outboard Horizontal Stabilizer(OHS) Parent Vehicle

outboard of the main-wing. Two booms extend backward from the tips of the main wing and the horizontal and vertical tail surfaces are located at the end portions of the booms. This vehicle configuration is called *Outboard Horizontal Stabilizer*(OHS). The main reason

for choosing this configuration for the Parent UAV is that it provides an open space behind, so the Mini vehicle can approach the Parent from behind without obstruction during air rendezvous.

The OHS configuration has a unique aerodynamic property. Much research on this aerodynamic configuration was previously done at the University of Calgary [25, Kentfield], [32, Mukherjee]. The aerodynamic difference between the OHS and a standard airplane configuration is that for the OHS configuration the horizontal tail surfaces experience the upwash of the trailing vortices generated by the main wing because the horizontal tail surfaces are placed outboard and behind the main wings. Moreover, if the pitch angle of an OHS aircraft is increased (nose up), then the increase in the angle of attack on the main wing produces stronger trailing vortices resulting in stronger upwash on the tail surface. Then, the corresponding increase in the angle of attack on the tail surface (i.e. not only from the pitch attitude change but also from the increased upwash) generates larger restoring pitching moment. This enhanced stability feature enables an OHS airplane to have its center of gravity positioned further rearward, as compared to a conventional airplane. Typically, the OHS can be trimmed in static stable flight with significant positive lift generated by the horizontal tail. This is the main aerodynamic benefit of the OHS configuration, compared to a standard configuration where the tail surface usually generates negative lift.

For the demonstration OHS Parent vehicle constructed by the team, the stability neutral point was estimated at 80 percent of the chord from the leading edge, and the center of gravity was chosen at 55 percent of the chord.

The main disadvantage of the OHS configuration is the structural weakness. The aerodynamic load on the tail surface is transmitted only through the tail boom. Thus, the effect of the twist of the main wing section should be carefully considered in the design phase. The design and the construction of the wing section are discussed in detail in [45, Urbain] and [26, Kepler], and the modeling for the flexibility effect of the tail boom section is described in Section B.7.

The team built a 6.1-meter tail span (distance between each tip of the horizontal tail surfaces) OHS Parent UAV. Dimensions of the demonstration OHS Parent vehicle and other basic properties are summarized in Table 2.2. In the design of the OHS Parent, the wing loading was selected to be close to that of the Mini vehicle, so that a sufficient overlap exists in the speed ranges of the two vehicles.

Total Weight	20 kg	Empty Weight	18 kg
Tail Span	6.1 m	Wing Span	4.5 m
Wing Area	2.43 sq.m	Wind Chord	0.54 m
Length	2.6 m	Fuselage Dim.	30 x 26 x 130 cm
Dihedral	2 deg.	Tail Volume	0.71
Speed	16∼26 m/s	Flight Time	30 min.
Engine	Moki 2.1 cu.in.	Airfoil	NACA2412

Table 2.2: Properties of OHS Parent vehicle

The OHS Parent is also required to carry a capturing device for a potential reintegration capability with the Mini vehicle. The capturing device was also built, and Figure 2-3 (a) shows a picture of this device at the top of a truss mounted on the fuselage. This capturing

(a) OHS Parent with Truss (b) OHS Parent inside a Dodge Caravan

Figure 2-3: Outboard Horizontal Stabilizer(OHS) Parent vehicle

device was not actually used in flight testing, but the truss has served to mount an airspeed sensor, a GPS antenna, and a light source for guiding the Mini in Phase II.

Another important requirement imposed in the design of the demonstration OHS Parent was the transportability using a van. The entire aircraft can be disassembled into five main parts - fuselage, two half wings and two tail sections. Figure 2-3 (b) shows a picture of the five main parts inside a van.

2.2 Avionics

Inexpensive, commercial off-the-shelf avionics components were used to construct the on-board avionics. They are summarized in Table 2.3. The Mini vehicle has a limited payload

Component	Price
PC104 Computer Stack	
- CPU module, Analog Data module, Utility module	$ 2,200
GPS : Marconi, Allstar GPS Receiver	$ 1,000
Inertial Sensors :	
- Crossbow 3-axis Accelerometer (Mini)	$ 350
- Tokin Ceramic Gyros (Mini)	$ 150
- Crossbow IMU (OHS)	$ 3,500
Pitot Static Probe : hand-made with Omega Pressure Sensor	$ 75
Altitude Pressure Sensor (for high frequency estimation)	$ 75
Communication : Maxstream, 9XStream Transceiver	$ 200
Total - Mini	$ 4,000
OHS	$ 7,500

Table 2.3: Commercial Off-the-Shelf Avionics Components

capability. Thus, light weight low quality inertial sensors were used for the avionics of this vehicle. For example the Tokin ceramic rate gyro used in the Mini vehicle has a typical drift rate of 5 degrees per minute.

In the series of numerous flight tests, it became routine to fly the airplanes manually in normal RC mode, without loading the avionics onboard, for the first flight of a test day. This practice of the initial manual flight serves as a chance to check the vehicle condition and also enables the pilot to regain familiarity with the flight handling for the plane. After this first manual flight, avionics are installed in the plane for the main test. To do the installation quickly and easily in the field an *avionics box* was constructed for each vehicle. This box has a bass wood main frame and includes the avionics components, which are not necessary for the pure RC control, such as the main computer stack, the inertial sensors, the GPS receiver, the transceiver, the analog conditioning board, the servo control computers, and the control panel. Figure 2-4 (a) and (b) show the avionics boxes for Mini and OHS

Parent vehicles. Each box weighes about 2.0 kg. They were designed to be easily attached

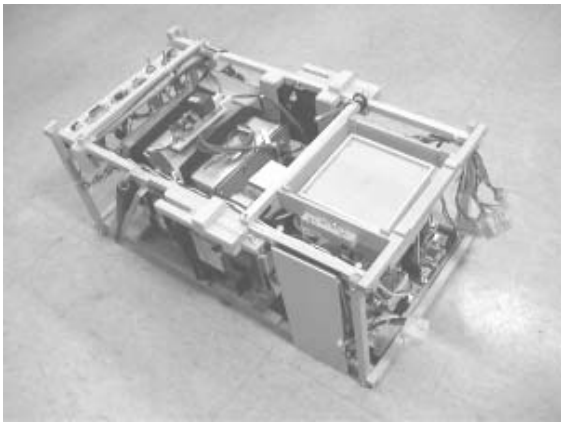

(a) Mini Avionics Box

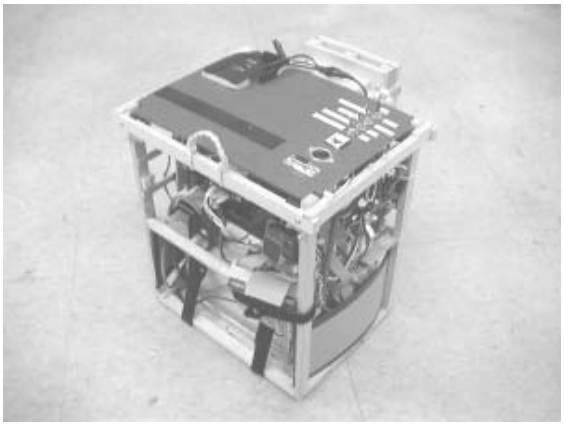

(b) OHS Avionics Box

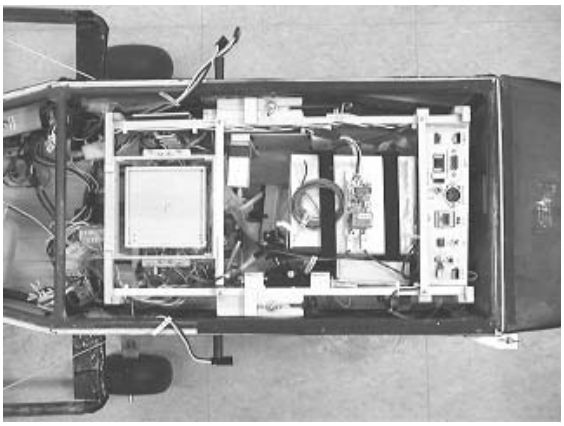

(c) Mini Avionics in Fuselage

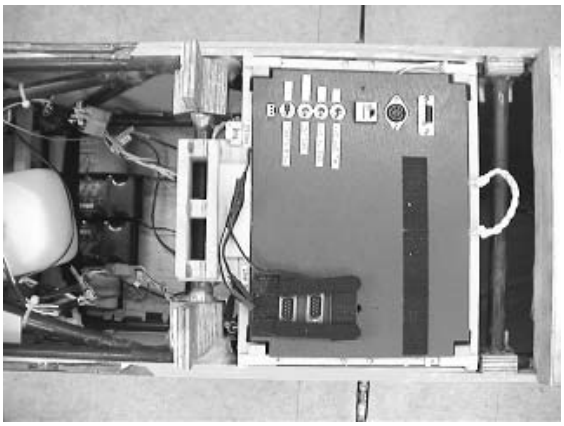

(d) OHS Avionics in Fuselage

Figure 2-4: Avionics Boxes

to the vehicle main body. Figure 2-4 (c) and (d) show the avionics boxes installed in the fuselage of the two vehicles.

A detailed report on the avionics including the hardware architecture and component descriptions are provided in Appendix A.

2.3 Modeling and Simulation

This section gives a brief summary of the dynamic modeling for the OHS Parent and the Mini vehicles. A more detailed description of the modeling effort is given in Appendix B. The modeling procedure is outlined below. First, the flight conditions for the two vehicles

during the rendezvous were estimated. This process was done based on the power v.s. speed relations [39, Raymer] for the two aircraft. The flight speed of 22 m/s was chosen as an optimal trim speed, which is the middle of the overlap of the two vehicle's speed ranges. A model of each vehicle was constructed based on the 6 degree-of-freedom(DOF) rigid body dynamics. Aerodynamic forces and moments were estimated using a Vortex Lattice method, at the chosen flight condition. For the Mini aircraft some of the aerodynamic coefficients were measured from wind tunnel tests. The dynamic simulation model for each vehicle was constructed in the Matlab Simulink environment. A linear model was extracted at the selected flight condition for use in the controller design.

Because of the OHS vehicle configuration, the flexibility of the tail section needed to be considered for the Parent vehicle. A detailed description is given in Section B.7. The model for the flexibility effect was used in simulations and the controller design phase.

Hardware-in-the-loop Simulation

Hardware-in-the-loop simulation is a critical step in the preparation of autonomous flight test. It provides an important tool for debugging the flight software. Figure 2-5 shows a diagram of the hardware-in-the-loop simulation setup for one vehicle. The flight computer

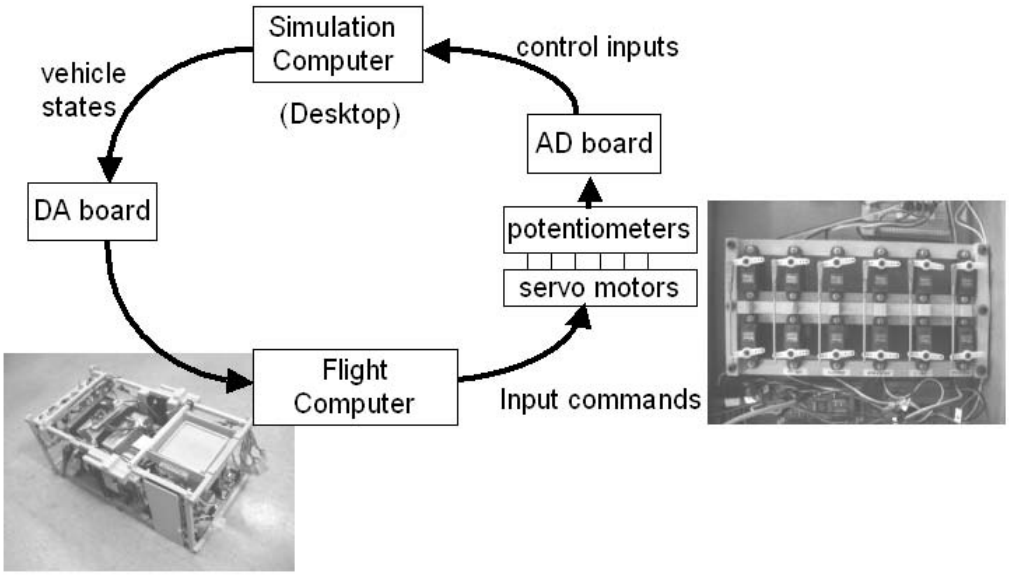

Figure 2-5: Hardware-in-the-loop Simulation

in the diagram runs the flight software, and the simulation computer provides the aircraft flight dynamics. The flight computer commands the servo motor deflections, and the deflection angles are measured by potentiometers. The servo-motor/potentiometer couplings are shown in Figure 2-5. The measurements of the potentiometers are converted by an A/D board, and are read as the control surface deflections by the simulation computer. The simulation computer solves the vehicle differential equations in real time and generates the vehicle states. Some of the vehicle states associated with the flight sensors are converted by the D/A board to voltage values. These values are read by the flight computer through the analog data board.

2.4 Controller Design and Analysis

A detailed description of the controller design and analysis is provided in Appendix C, using the Mini UAV as an example. This section gives a brief summary with the controller configurations.

2.4.1 Lateral Controller

Classical controller design techniques [5, Stevens & Lewis] were used for the vehicle lateral-directional control. Figure 2-6 shows the controller configuration. In terms of the design

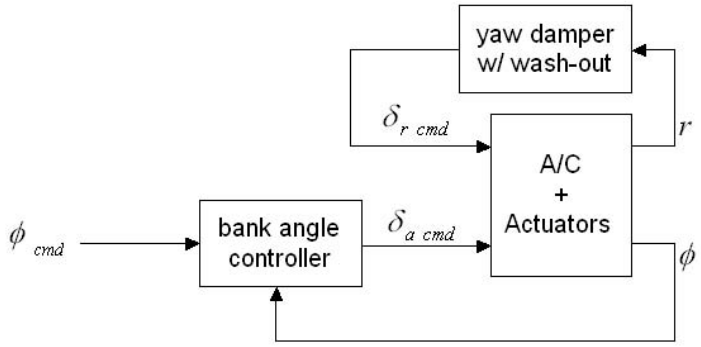

Figure 2-6: Yaw Damper and Bank Controller

procedure the yaw damper was designed first to improve the dutch-roll damping, and then the bank angle controller was cascaded. The bank angle controller will be used as a mech-

anism to generate sideways acceleration (a_s) by the relation

$$a_s \approx g \cdot \phi$$

when an acceleration command is given from an outer loop guidance logic. A detailed description on the lateral controller design is given in Section C.1

2.4.2 Longitudinal Controller

In the longitudinal airplane motion there is a significant coupling between the two control inputs (engine power, elevator) and the two main outputs (speed, altitude). Due to these interactions, a diagonal controller configuration (where one control input is used for one control output and the other control input is used for the other control output) is not expected to perform well. Therefore, a multivariable control technique was employed. A linear quadratic regulator(LQR) was used in order to take the advantage of its excellent robustness property[50, Zhou]. In order to comply with the full state feedback condition imposed by the LQR controller, the controller was designed with a reduced order model which includes only the basic longitudinal vehicle states. This means that the high frequency dynamics in the actuators and sensors were not included in the design phase. But, these missing components were included in the analysis and simulation stages.

The block diagram of the linear quadratic controller is shown in Figure 2-7. The velocity command and the altitude rate command are imposed in order to have the tracking capability for these variables. This linear quadratic controller was used as a low level controller for both vehicles and in both rendezvous phases. Different guidance loops were closed around it depending on the rendezvous phase. During phase I the altitude command is provided from the higher level path planning algorithm. In order to follow the altitude command an additional outer loop controller is cascaded around the linear quadratic controller. A lead-lag controller was used for the outer loop controller, and it generates the altitude rate command. The total longitudinal controllers on both vehicles were designed to meet

- 1 m/s of speed error
- 1$\sim$2 m of altitude error

under the nominal wind speed of 5 m/s, which is more than 20 % of the vehicle flight speed. A detailed description on the longitudinal controller design is given in Section C.2.

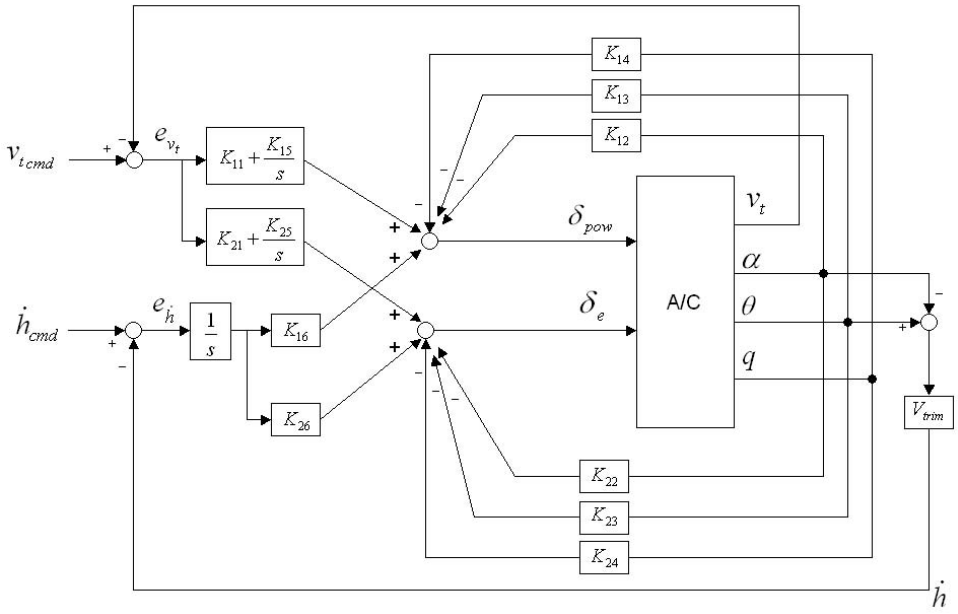

Figure 2-7: LQR Longitudinal Controller with Velocity and Altitude Rate Tracking

The associated flight test results are given in Chapter 6. The use of the linear quadratic controller during Phase II is reported in Chapter 5.

2.5 Summary

This chapter gave a summary on the flight test setup. It first reported the inexpensive commercial off-the-shelf avionics components. Then it outlined the development of the dynamic models for the two vehicles. Finally, it presented the controller configurations.

Chapter 3

Guidance for Phase I of Mid-Air Rendezvous

In performing the rendezvous Phase I, the team chose an approach where a reasonable flight path is first generated for each vehicle, and then the vehicle would be controlled to follow the desired path as tightly as possible. This chapter briefly describes the path generation algorithm, then it gives a detailed description on the guidance logic.

3.1 Phase I Path Planning

To assure that the two UAVs perform the Phase I of mid-air rendezvous without aborting the procedure it is important to establish a routine for two UAVs to follow every time. The routine in Figure 3-1 was developed by Damien Jourdan, who performed the studies on the path planning for Phase I. A detailed description on the planning algorithm can be found in his thesis [24]. A brief overview is presented here.

First, the OHS Parent is maintained in flight along a 500 meter diameter circle, with no information on the Mini vehicle. The Parent vehicle sends its position and velocity information at intervals of 0.2 seconds to the Mini vehicle throughout the flight. It also sends the information on the location of the center and the radius of the circle.

It is the Mini vehicle that schedules its path in order to meet the Parent vehicle somewhere on the circle, at a required separation. When a rendezvous command is activated, the onboard computer in the Mini vehicle generates a flight path command to follow. This path command is composed of four segments. The first segment is climb or descent. This

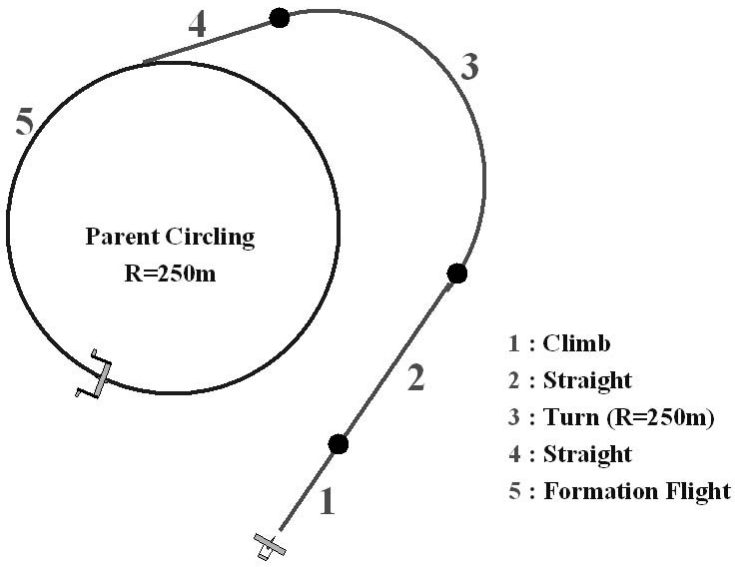

Figure 3-1: Path Planning for Phase I Rendezvous

process is to match the altitude of the Parent vehicle. The second segment is straight line. The third segment is a turn with the same radius as the Parent's circle. The final segment is another straight line, which leads the path tangentially to the circle. After the final segment, the two vehicles perform a formation flight, moving along the circle, while maintaining a position difference of 20 meters, for the next phase of rendezvous.

The outputs of the path planning algorithm are desired flight trajectories and speed commands for the two vehicles to follow. The following sections will discuss how to tightly follow the desired flight path.

3.2 Prior Work on Guidance Methods

Two approaches can be considered for the problem of trajectory tracking. One way is separating the guidance and flight control problem into an outer loop and an inner loop. In this case, the inner loop uses aerodynamic and propulsive controls to achieve a commanded attitude or velocity, which is generated by an outer loop. Well established design methods are used for the flight control inner loop, and simple strategies based on geometric and kinematic properties are used in the guidance outer loop.

Another way is an integrated approach where the inner-outer loop is designed simultaneously. Numerous research works were found reporting results using this combined approach.

In [10, Smallwood & Whitcomb] the authors report model-based trajectory tracking for underwater robotic vehicles. In [12, Johnson et.al.] the authors report neural network based adaptive flight control architecture for trajectory following. In [17, Makarov et.al.] the authors report an adaptive controller designed using the method of recursive aim inequalities. [18, Kaminer et.al.] reports a technique that reduces the trajectory tracking problem to the design of a controller for a linear-time invariant plant by utilizing a simple nonlinear transformation that inverts kinematics. In [27, Keviczky & Balas] the authors report an adaptive receding horizon technique for aircraft control to achieve aggressive maneuvering. In [33, Murray] and [34, Rathinam & Murray] the authors report a technique that utilizes differential flatness in constructing feasible trajectories.

In this research program, the first approach was taken by the project team because well established design methods are available in the aircraft inner loop control and the combined approaches involve complexity in the implementation. For the inner loop the bank angle controller was used. The relation $a_s \approx g \cdot \phi$ derived from aircraft coordinate turn was deployed to convert the lateral acceleration(a_s) command into the bank angle(ϕ) command. The acceleration command is generated from the guidance level. The following subsections summarize the previous works on the guidance strategies.

3.2.1 Cross-track Error Guidance

Linear controllers are commonly used for the guidance of an aircraft. In a traditional waypoint guidance situation as shown in Figure 3-2, the cross-track error is used for feedback control. Typically, PD (proportional and derivative) controllers are used to generate required lateral acceleration or bank angle command. The derivative control is necessary because there are double integrators in the plant model due to kinematics (from the acceleration input to the track position output). There are a number of limitations in this

Figure 3-2: Traditional Linear Controller on Cross-track Error

method. First, in following a series of waypoints, once the vehicle arrives near a waypoint, complex switching decision logic is required for a smooth transition from one waypoint to the next. Second, if this technique - feedback control with cross-track error - is used in following a curved trajectory, the performance degrades, especially under wind conditions, as will be explained in Section 3.3.4.

3.2.2 Lateral Track Control Law for Aerosonde UAV - Marius Niculescu (2001)

A nonlinear lateral track guidance logic was proposed by [35, Niculescu] for better performance in following a straight flight path between two waypoints. Figure 3-3 shows a diagram to explain the algorithm. Here, y_{track} is the cross-track error, and x_{track} is defined

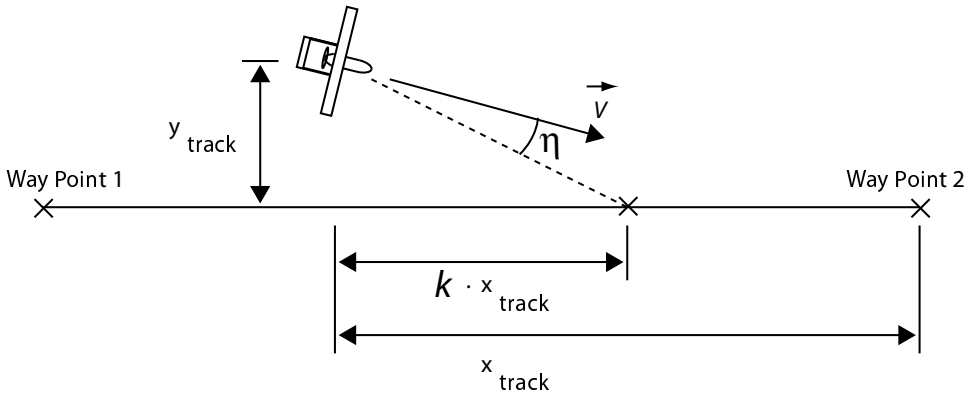

Figure 3-3: Guidance Method by Marius Niculescu (2001)

as the remaining distance to the waypoint, currently aiming at, on the straight line path. An imaginary reference point along the straight line is defined by multiplying x_{track} by a factor of k as depicted in the figure. The lateral acceleration command is generated in order to reduce the angular difference (η) between the direction of the velocity vector and that of the relative position vector from the vehicle position to the reference point. The corresponding feedback law can be expressed by

$$a_{cmd} = K_a \left(k \; x_{track} \; \dot{y}_{track} - y_{track} \; \dot{x}_{track}\right)$$

where a_{cmd} is a lateral acceleration command and K_a is a control gain.

In [35, Niculescu] the author claims that this method does not require complex switching decision logic and the aircraft is able to stably track a flight plan segment starting from any

initial conditions. However, a primary limitation of this method comes from the implied assumption that the desired path should be a straight line between two waypoints.

3.2.3 Guidance Laws for tactical Missiles

Much research has been devoted to the guidance laws for short-range tactical missiles. These guidance laws are used to command missiles during their homing phases of flight. Missile guidance laws are applicable to the purpose of trajectory following by using an imaginary point moving along the desired flight path as the target. This section provides a brief summary of missile guidance laws, and later Section 3.3.2 will show the relation between one of the missile guidance laws and the trajectory following guidance logic developed in the project.

According to [16, Warren, et.al.] and [43, Shneydor], short range missile guidance laws typically fit within the following categories:

- Line-of-sight guidance
- Pursuit guidance
- Proportional navigation
- Optimal linear guidance

Line-of-sight guidance is divided into two subsets - beam rider (BR) guidance and command to line-of-sight (CLOS) guidance. In BR guidance, a missile is controlled to fly along a beam (i.e., radar or laser) that is continuously pointed at the target from a projector usually on the ground. CLOS guidance is similar to BR guidance, except the guidance law takes the beam motion into account to improve the performance. Some of the relevant texts and papers are [48, Zarchan], [8, Clemow], [19, Kain & Yost].

Pursuit guidance has two subsets - attitude pursuit and velocity pursuit. Using the attitude pursuit method, a missile is controlled such that its longitudinal axis is directed at the target. With velocity pursuit, the missile's velocity vector is kept pointed at a target. Some of the relevant texts and papers are [30, Locke], [40, Rishel], [13, Chatterji & Pachter].

In proportional navigation guidance, a missile is controlled so that the angle of the line-of-sight between the missile and a target is to be kept constant. Formally, the guidance law

is expressed by

$$a_{\perp LOS} = N' \, V_C \, \dot{\lambda}$$

Here, $a_{\perp LOS}$ is the acceleration command perpendicular to the line-of-sight, N' is a navigation constant, is usually chosen between 3 and 5, V_C is closing speed between the missile and its target, and $\dot{\lambda}$ is the time derivative of the line-of-sight angle. Proportional navigation is known to generally provide the best performance, with less control effort, in constant-velocity intercepts and is widely accepted as the preferred method of guidance [19, Kain & Yost]. Some of the references are [48, Zarchan], [4, Blakelock].

The optimal control technique emerged in the mid-1960's, based on linear model dynamics with quadratic costs and additive Gaussian noise, was adopted in the missile guidance literature. Some of the developments based on optimal control theory are [6, Bryson], [22, Deyst & Price].

All of the methods described here could be adapted, with some modifications, to the problem of trajectory following. The trajectory following guidance logic described in the next section was motivated by the proportional navigation. The relation of the trajectory following guidance logic to the proportional navigation is described in Section 3.3.2.

3.3 Lateral Guidance Logic for Trajectory Following

Building on previous research and operational experience, this section proposes a nonlinear lateral guidance logic for tightly tracking a desired path. The guidance logic is composed of two elements. The first element is the *selection of a reference point* on the desired trajectory, and the second element is the *generation of lateral acceleration command* using the reference point.

Selection of Reference Point

The reference point at each instant is chosen

- on the desired path
- at a certain distance (L_1) from the vehicle in the forward direction

as shown in Figure 3-4.

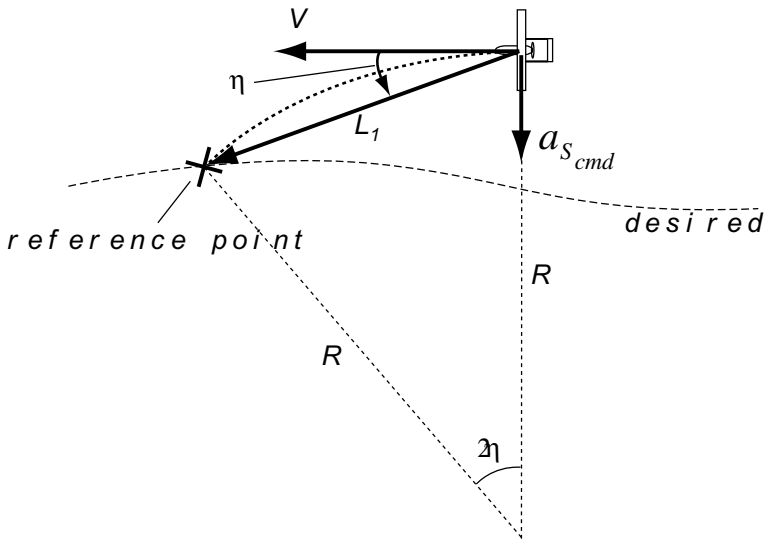

Figure 3-4: Lateral Guidance Logic

Lateral Acceleration Command

The lateral acceleration command is generated by

$$a_{s_{cmd}} = 2\frac{V^2}{L_1}\sin\eta \tag{3.1}$$

Two properties of this equation should be noted.

- The direction of the acceleration depends on the sign of η. For example, if the selected reference point is on the left side from the direction of the vehicle velocity vector, then the vehicle will be commanded to accelerate to the left, which is the case in Figure 3-4. In other words, the vehicle will tend to align its velocity direction with the direction of $\vec{L_1}$.

- At each point in time a circular path can be imagined which is defined by the position of the reference point, the vehicle position, and the vehicle velocity direction, as indicated by the dotted line in Figure 3-4. This circular segment is uniquely defined because it starts from the vehicle position, *tangential* to the vehicle velocity direction, and ends at the reference point. The acceleration command generated by Equation 3.1 is equal to the centripetal acceleration required to follow this instantaneous circular segment. This is explained by

$$L_1 = 2R\sin\eta$$

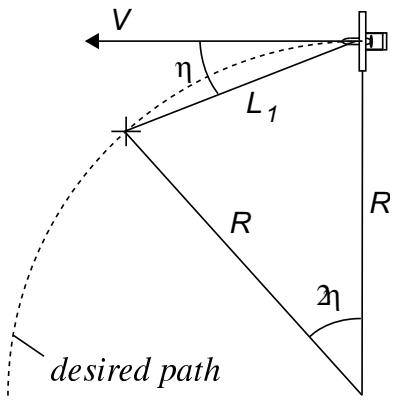

Figure 3-5: Steady Turn

So

$$\text{centripetal acceleration} \;=\; \frac{V^2}{R} = 2\frac{V^2}{L_1}\sin\eta \,(= a_{s_{cmd}})$$

If the desired path is a circle, this choice of acceleration gives zero steady-state error. For example, when the vehicle is following the desired circular path shown in Figure 3-5, the acceleration command generated by the guidance logic is the same as the associated centripetal acceleration.

3.3.1 Understanding the Mechanism of the Nonlinear Guidance Logic

In order to understand the mechanism of the nonlinear guidance logic, a discrete time step approach is taken in this section. First, Figure 3-6 shows the mechanism of the guidance logic in one time step increment. In this diagram, the reference point is to the left of the direction of the vehicle velocity. Therefore, at the next time step the velocity direction rotates counter-clockwise due to the acceleration command.

Mindful of the mechanism for the one time step increment, consider Figure 3-7, which shows the two cases where the vehicle is relatively (a) far away from or (b) close to the desired path. Given a certain length L_1 as shown in Figure 3-7, it can be inferred that

- The direction of L_1 makes a large angle with the desired path, when the vehicle is far away from the desired path.
- The direction of L_1 makes a small angle with the desired path, when the vehicle is close to the desired path.

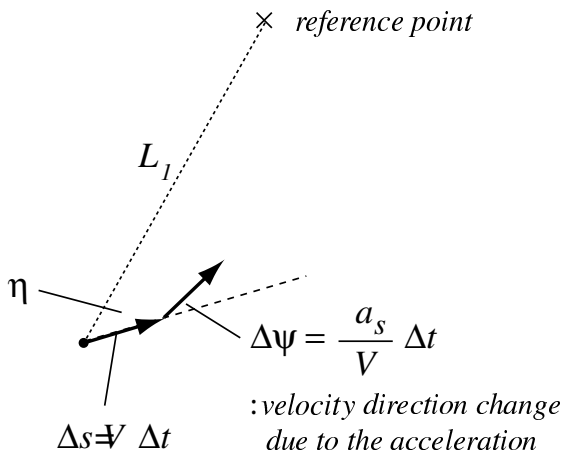

Figure 3-6: Discrete Representation : One Time Step

Therefore, if the vehicle is far away from the desired path, then the guidance logic chooses the reference point in such a way that the vehicle rotates its velocity direction to approach the desired path at a large angle. On the other hand, if the vehicle is close to the desired path, then the guidance logic chooses the reference point in such a way that the vehicle rotates its velocity direction to approach the desired path at a small angle.

Figure 3-8 shows the trajectory of the vehicle over several time steps, where the vehicle initially starts from a location far away from the desired path, and eventually converges to the desired path. It should be noted that at an appropriate point the vehicle changes its steering commands from left to right turns, which results in a smooth convergence of the vehicle to the desired flight path.

3.3.2 Relation to Missile Guidance Laws

Consider the reference point as a target and the aircraft as a missile. Then, the trajectory following guidance logic is similar to the velocity pursuit missile guidance in a sense that the angular deviation between the vehicle velocity direction and the LOS is used as a feedback variable. The sine function of the angular deviation is nonlinearly combined with the vehicle velocity and the L_1 distance in the feedback of the trajectory tracking guidance logic while the angular deviation is linearly used in the feedback of the pursuit guidance.

Another interesting similarity is found in relation to proportional navigation missile

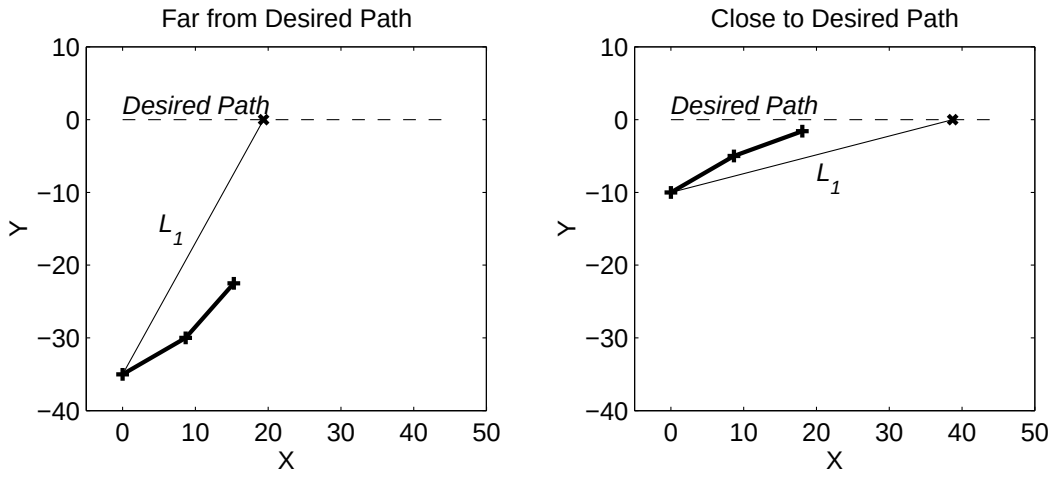

(a) (b)

Figure 3-7: Discrete Representation : Far vs. Close (Note the same L_1 distance. Δt=1, V=10, and L_1=40 are used in the simulation)

guidance. The formula

$$a_s = 2\frac{V^2}{L_1}\sin\eta$$

for the lateral acceleration command in the trajectory following guidance logic can be shown to be equivalent to the formula

$$a_{\perp LOS} = N'V_C\dot{\lambda}$$

for the acceleration command perpendicular to the line-of-sight in the proportional navigation with a navigation constant of N'=2, *under the assumption that the reference point is stationary* in the computation of the line-of-sight rate and the closing velocity. This equivalence can be shown using Figure 3-9. First, noticing that there is an angular difference between the vehicle lateral acceleration(a_s) and the acceleration($a_{\perp LOS}$) perpendicular to the LOS

$$a_{\perp LOS} = a_s\cos\eta$$

Using the acceleration command formula

$$a_s = 2\frac{V^2}{L_1}\sin\eta$$

leads to

$$a_{\perp LOS} = 2\frac{V^2}{L_1}\sin\eta\cdot\cos\eta = 2\left(V\cos\eta\right)\left(\frac{V}{L_1}\sin\eta\right)$$

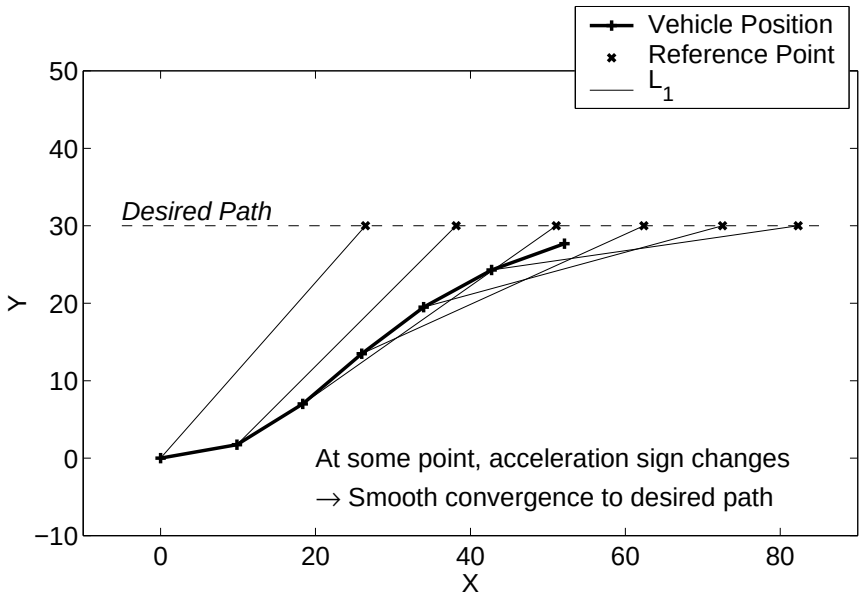

Figure 3-8: Discrete Representation : Step by Step (Δt=1, V=10, and L_1=40 are used in the simulation)

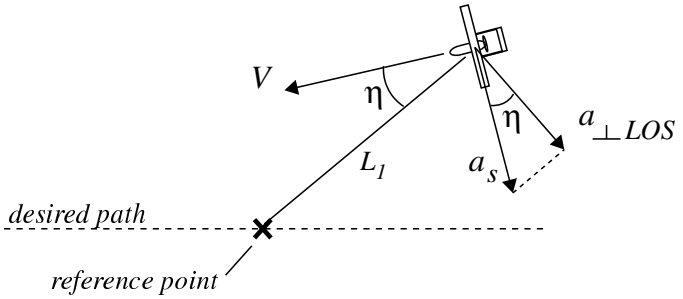

Figure 3-9: Relation with Proportional Navigation

where, assuming that the target point is stationary, the first bracket is the closing velocity (the relative velocity component in the direction of the LOS) and the second bracket is the LOS rate. Therefore, it can be shown that

$$a_{\perp LOS} = 2 \cdot V_C \cdot \dot{\lambda}$$

which is the form of the proportional navigation formula with the navigation constant equal to 2. However, the approach to explain the whole guidance logic (selection of reference point + acceleration command) only by the proportional navigation is not appropriate because the reference point is actually moving, and the closing speed between the reference point

and the vehicle is always zero (with L_1 fixed).

3.3.3 Linear Properties and Selection of L_1

The design choice in the lateral guidance logic is the distance(L_1) between the vehicle and the reference point. This value can be chosen by investigating the linear property and stability analysis.

Figure 3-10 shows a situation for the linearization. L_1 is the distance between the vehicle

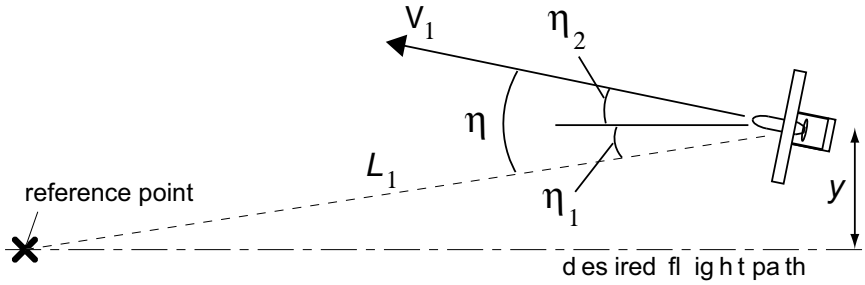

Figure 3-10: Linear Model of Phase I Guidance

and the target point, y is the cross-track error, and V_1 is a vehicle nominal speed. Assuming η is small in magnitude

$$\sin\eta \approx \eta = \eta_1 + \eta_2$$

and

$$\eta_1 \approx \frac{y}{L_1}, \qquad \eta_2 \approx \frac{\dot{y}}{V_1}$$

Combining the above with the guidance formula leads to

$$a_{s_{cmd}} = 2\frac{V^2}{L_1}\sin\eta \approx 2\frac{V_1}{L_1}\left(\dot{y} + \frac{V_1}{L_1}y\right) \tag{3.2}$$

Hence, linearization of the nonlinear guidance logic yields a PD (proportional and derivative) controller for the cross-track error. Also, the ratio of the vehicle speed(V_1) and the separation distance(L_1) is an important factor in determining the gains of the proportional and derivative controllers. For instance, a small value for L_1 would lead to a high control gain.

The separation distance is chosen by performing a stability analysis with the linear plant model and the derived linear controller. The plant model includes the vehicle dynamics with inner-loop bank angle controller and any sensor dynamics in the associated loop transmission

function. For the PCUAV demonstration system, the control gain is limited by the inner-loop bank control bandwidth (2∼3 rad/s) and the GPS time delay of 0.4 seconds. With the nominal flight velocity around 25 m/s, the choice of L_1=150 m results in the associated crossover frequency at 0.4 rad/s.

3.3.4 Comparison of the New Guidance Logic with the Traditional Linear Method

In the previous section, it was shown that the nonlinear guidance logic approximates a linear PD controller, on cross-track error, if η is a small angle. This section will compare, by simulations, the performance of the nonlinear guidance logic and the associated linear controller, for various cases of trajectories and wind conditions.

In the simulation analysis presented below, the separation distance of 150 m was used, and 25 m/s of nominal vehicle speed was used for the associated linear controller given by Equation 3.2.

Comparison 1 - Straight Trajectory Following

First, the two methods were applied for tracking a straight line. Figure 3-11 shows the simulation setup and results. The simulation results indicate that the performances of the two methods are roughly the same in following a straight trajectory, in either no wind or 5 m/s of cross wind conditions.

Comparison 2 - Curved Trajectory Following

Next, the two methods were applied for tracking a curved line. Figure 3-12 shows the simulation setup, the desired curved flight trajectory, and the associated simulation results. The aircraft is initially at level flight heading due north. The trajectory plot (a) in Figure 3-12 is the case where the linear controller was used. The PD controller resulted in a steady state error of about 40 meters. The reason for the steady state error can be explained by the system types in control theory. There are two pure integrators in the associated loop transmission with a plant model and the PD controller. The two integrators are from the kinematics of the plant model - from the *acceleration input* to the *position output*. The steady state error occurs because the position reference command for cross-track is imposed in a parabolic fashion when a desired path is a circle.

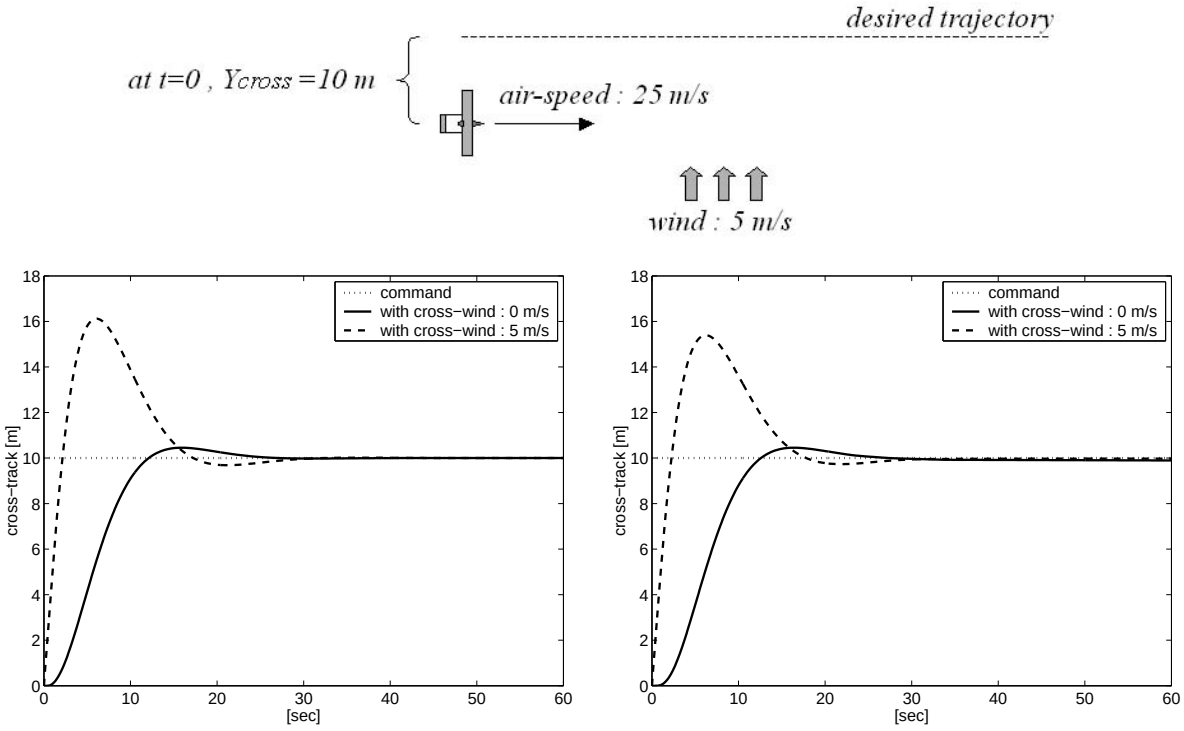

(a) PD Linear Control

(b) Nonlinear Guidance Logic

Figure 3-11: Comparison - Straight Line Following

In order to fix the error, an integrator was added. The simulation result using the resulting PID controller is now plotted in the same graph as a solid line. The steady state error is removed by adding the integration controller. But the error during the initial transition still remains.

On the other hand, the nonlinear guidance logic worked very well in following the curved path as indicated in Figure 3-12 (b).

Comparison 3 - Curved Trajectory Following with Wind

Another set of simulations were executed with similar conditions and with an additional 5 m/s steady wind. The direction of the wind was from west to east. The vehicle initial condition and the wind condition are shown in Figure 3-13. The performance of the linear controllers (PD and PID) are shown in the trajectory plot (a) in Figure 3-13.

For the PD controller, the cross-track error varied in a range between 30 m and 60 m, after the initial transition period. For the PID controller, the cross-track error varied in

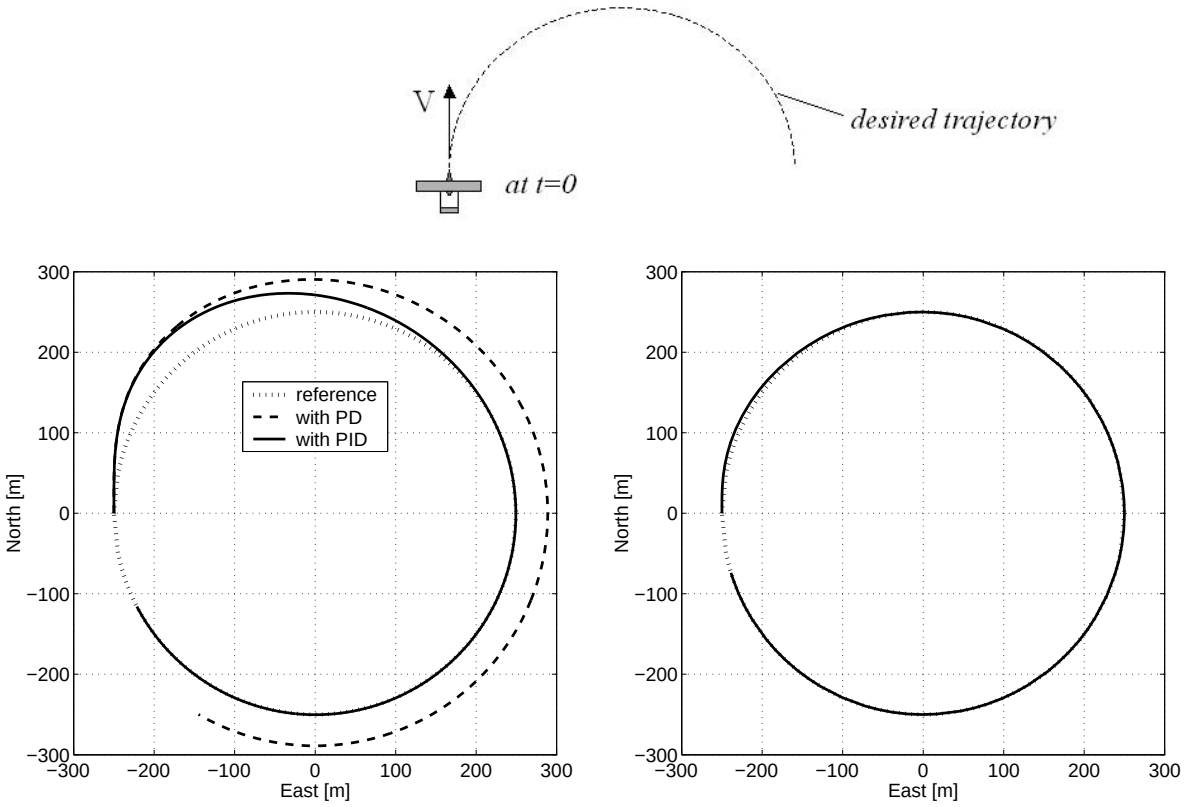

(a) PD, PID Linear Control

(b) Nonlinear Guidance Logic

Figure 3-12: Comparison - Curved Line Following

the range between -20 m and +20 m after the initial transition period. A more careful look reveals that the vehicle flies outside the circular path when it is in the downwind region, and inside the circular path in the upwind region. The reason for this phenomenon can be explained by noting that when the vehicle is in the downwind region, it moves faster with respect to inertial frame. Under this condition, the vehicle must generate a larger acceleration command (or a larger bank angle command) if it is to follow the desired circular path. The linear feedback controller with a fixed gain has an inherent limitation and cannot immediately remove the error, which is the result of an increased flight speed from the wind effect.

On the other hand, the nonlinear guidance logic method worked very well in following the curved path in the wind condition as shown in Figure 3-13 (b). The reason for the better performance in this case be understood by the formula

$$a_{s_{cmd}} = 2\frac{V^2}{L_1}\sin\eta$$

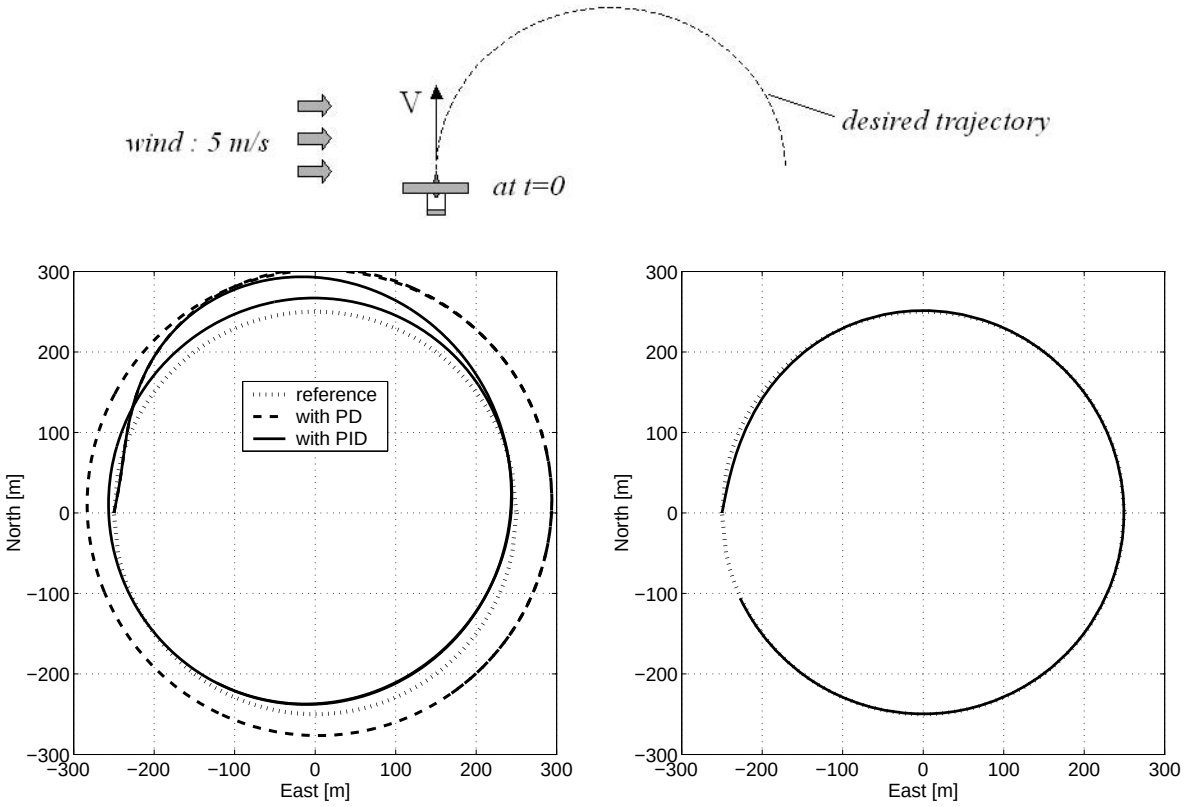

(a) PD, PID Linear Control

(b) Nonlinear Guidance Logic

Figure 3-13: Comparison - Curved Line Following with Wind

where the vehicle ground speed (as a surrogate for inertial velocity) is used for V at each instant in generating the acceleration command. In other words, the nonlinear guidance logic takes into account the inertial velocity changes due to the wind effect, and adapts to the situation accordingly.

3.3.5 Decomposition of the Angle η

Another reason for the superior performance of the nonlinear guidance logic, in following a curved trajectory, is explained below by investigating the angle of η. Figure 3-14 is a diagram showing the decomposition of this angle. It is assumed that the desired curved path segment around the current vehicle position is approximately a circular arc, represented as a dotted line in the diagram. The imaginary target point is also shown on the circular path at distance L_1 away from the vehicle. The cross-track error at this instant is indicated by the letter y. The instantaneous velocity vector is indicated by V. It should be noted

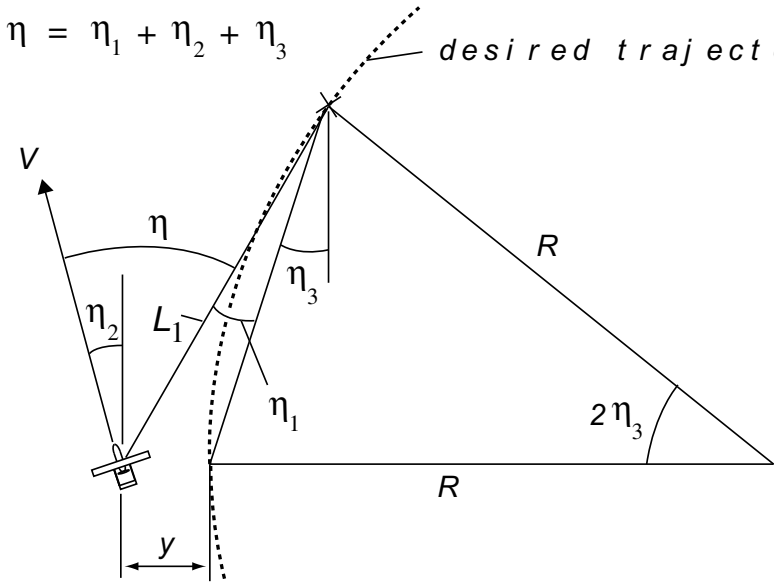

Figure 3-14: Decomposition of Line-of-Sight Rate

that

$$\eta = \eta_1 + \eta_2 + \eta_3$$

in this diagram. Then, the acceleration command is expressed as

$$a_{s_{cmd}} = 2\frac{V^2}{L_1}\sin\eta = 2\frac{V^2}{L_1}\sin(\eta_1 + \eta_2 + \eta_3)$$

First, η_1 is due to the cross-track error y, so, this term corresponds to a proportional feedback control on the cross-track error. Second, η_2 is due to the heading direction error, which means that the velocity vector is not aligned with the tangential direction of the desired flight path at this instant. Thus, the feedback of this term corresponds to a derivative feedback control on the cross-track error. Thirdly, the angle η_3 is related to the circular segment as indicated with the associated radius of curvature, R in the diagram. Thus, this term gives the preview of the desired flight path.

3.3.6 Characterization of Trajectory Error in the Nonlinear Guidance Logic

In theory, given a circle as the desired path, a vehicle is supposed to track the circular path with zero steady error under the nonlinear guidance logic no matter what the curvature is as long as the circle is large enough such that the reference point can be selected in the

forward direction of the vehicle. Indeed, the error property of the current guidance logic does not depend on the magnitude of the curvature of a desired path; instead it depends on the *change* of the curvature of a commanded path. The reason is because the reference point used to generate acceleration command at each instant is the one that is away from the vehicle. In other words, even though the guidance logic chooses a reference point on the desired path at $t = t_1$ and generates the acceleration command that would lead the vehicle to hit the point (if this acceleration were kept), whether or not the vehicle will actually hit the point depends on the shape of the desired trajectory after the reference point.

This behavior can be illustrated using another realistic case for the trajectory error that is typically encountered; that is the switch of flight paths between two straight lines with a certain angle as shown in Figure 3-15 (A).

In order to see these error properties, two prototypes were considered, and a simple analytical formula was derived for each case that relates the trajectory error with a parameter representing the change of a desired path. The analytical formula derived in this section are the results of a few approximations. Thus, they are not exact expressions. But they can be used for quick references to estimate the approximate value of the trajectory errors.

The first case is the switch of the flight paths with a certain angle as shown in Figure 3-15 (A). The desired flight path is initially a straight vertical line in the diagram and the flight path is switched to another line with the angle, θ. It is required to relate θ with the error that is defined in the diagram by the separation distance when the vehicle passes nearest the corner point of the desired path.

It is assumed that the vehicle has been following the vertical line in the diagram with zero cross-track error. Then, define $t_0 = 0$ when the vehicle is at a distance L_1 from the corner. Also define t_f is the time when the vehicle is nearest the corner point. It can be assumed that

$$t_f \approx \frac{L_1}{V}$$

The lateral acceleration obtained from the guidance logic is

$$a_s = \frac{2V^2}{L_1} \sin \eta \tag{3.3}$$

where $\eta_0 = 0$, and η at t_f will be approximately half of θ.

$$\eta_f \approx \frac{\theta}{2}$$

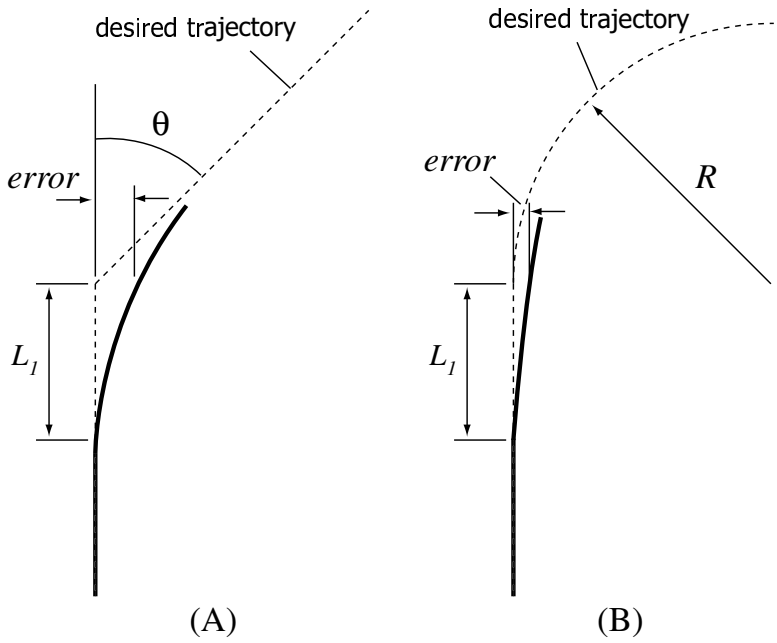

Figure 3-15: Prototype Trajectory Error Sources

Assuming

$$error << L_1$$

then η will be approximately linear with time

$$\eta \approx \frac{\eta_f}{t_f} t$$

Using this relation and performing double integrations on Equation 3.3 it can be shown that

$$error = \frac{4L_1}{\theta}\left(1 - \frac{2}{\theta}\sin\frac{\theta}{2}\right) \tag{3.4}$$

Some example cases for L_1=50, 150, 250 m are shown in Figure 3-16. The derived relation is verified by some of the simulations which are indicated by the marks 'x' in the graph for the case of L_1=150 m. The analysis indicates the smaller the L_1 distance and the smaller the θ angle, the smaller the trajectory error.

The second prototype considered here is the change of curvature in the desired trajectory. Figure 3-15 (B) shows the initial straight line path followed by a circular segment. It is required to relate the curvature($1/R$) to the error, when the vehicle is nearest the end of the first straight segment as depicted in the diagram.

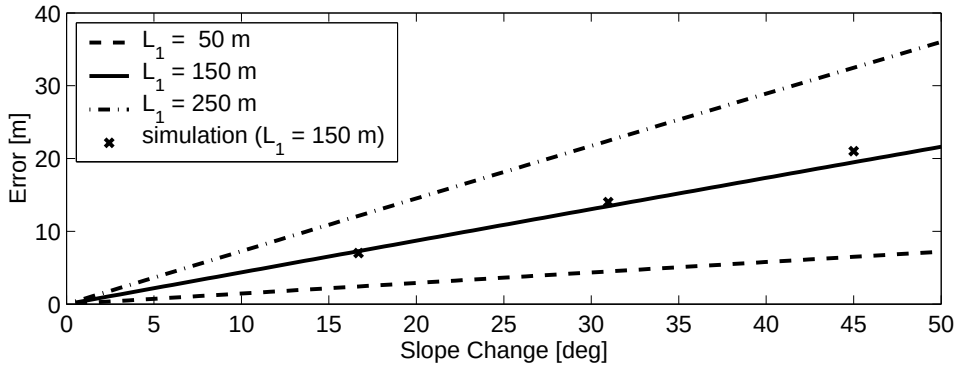

Figure 3-16: Error Properties due to Slope Change

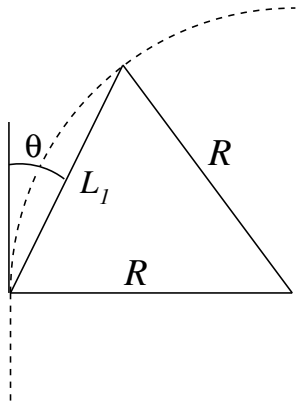

Figure 3-17: Geometry for case B

First, let $t_0 = 0$ when the vehicle is at a distance L_1 from the end of the straight segment. Let t_f be the time when the vehicle is nearest to the transition point of the desired path. As before assume

$$t_f \approx \frac{L_1}{V}$$

The acceleration from the guidance logic is

$$a_s = \frac{2V^2}{L_1} \sin \eta \approx \frac{2V^2}{L_1} \eta \tag{3.5}$$

where $\eta_0 = 0$, and it is assumed that η at t_f is approximately half of θ as shown in Figure 3-17. Thus,

$$\eta_f \approx \frac{\theta}{2} = \frac{1}{2}\left(\frac{\pi}{2} - \cos^{-1}\frac{L_1}{2R}\right)$$

Next, it is assumed that the η angle changes in parabolic fashion from $t = 0$ to $t = t_f$

(which was checked in several simulations)

$$\eta \approx \frac{\eta_f}{t_f^2} t^2$$

Using this relation and performing double integrations on Equation 3.5 it can be shown that at

$$error = \frac{L_1}{12}\left(\frac{\pi}{2} - \cos^{-1}\frac{L_1}{2R}\right) \tag{3.6}$$

Some of the example cases for L_1=50, 150, 250 m are shown in Figure 3-18. The derived

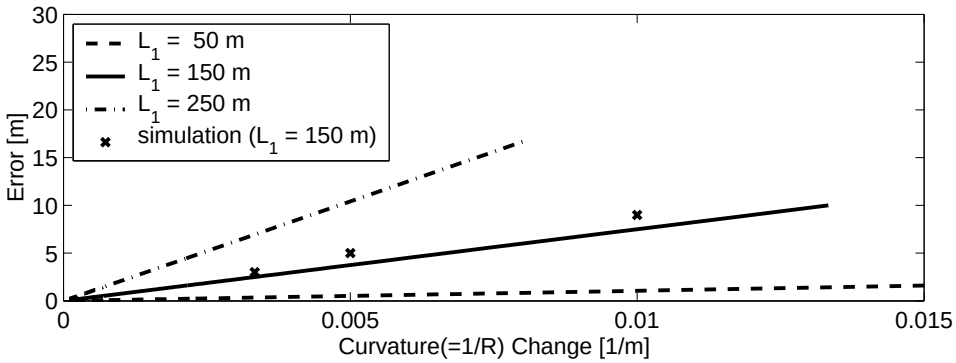

Figure 3-18: Error Properties due to Curvature Change

relation is verified by some of the simulations which are indicated by the marks 'x' in the graph for the case of L_1=150 m. The analysis indicates the smaller the L_1 distance and the smaller the curvature change, the smaller the trajectory error.

3.4 Summary

This chapter discussed a new guidance logic for trajectory following. The related flight test results are reported in Chapter 6

It showed in simulations that with the new method a vehicle follows a desired trajectory better than with the traditional linear technique. The reason for the better performance comes from the fact that the new method is based on geometry and kinematics. More specifically, it can be explained in twofold.

1. The angle η has the information on the upcoming flight path as shown in Section 3.3.5. This is a geometric factor, and it can be viewed as a kind of a feed-forward control.

2. The guidance logic uses the instantaneous vehicle speed in the computation of the acceleration command. This is a kinematic factor, and it adds the adaptive capability with respect to the change of vehicle speed due to the wind.

Another property of the new guidance logic is that it does not contain the element of the integral control. Thus, the new guidance logic is not robust to bias in the lateral acceleration measurement. In aircraft motion, the bank angle control is the mechanism to generate the lateral acceleration. Figure 3-19 shows a trajectory plots from a simulation with a 3 degrees of bank angle bias. The results shows a 9 meters of cross-track error. In

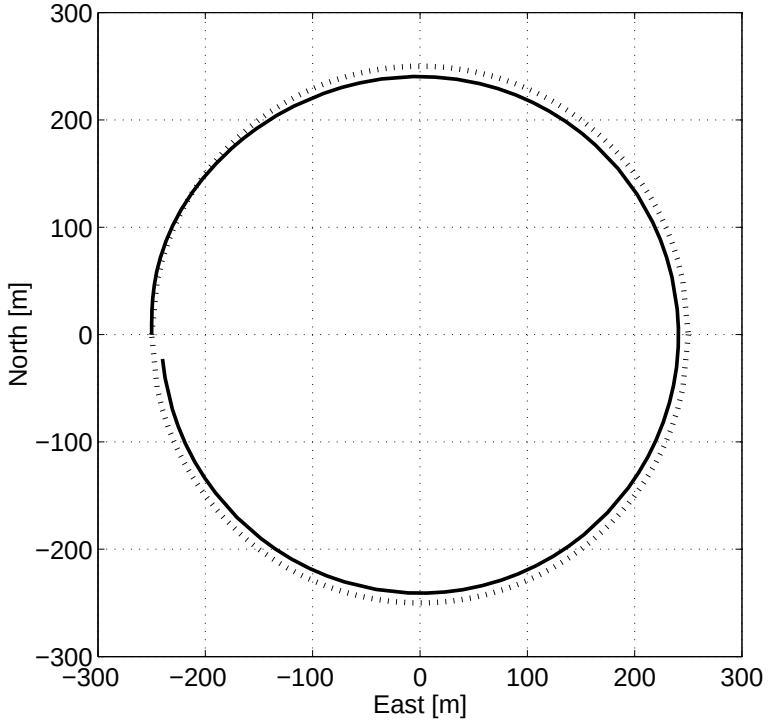

Figure 3-19: Simulation with 3 Degree Bank Angle Bias

order to solve this problem, a non-biased bank angle estimate is needed. The next chapter addresses a simple solution on this matter.

Chapter 4

Estimation

This chapter reports an estimation method that combines aircraft kinematics, GPS, and low quality inertial sensors to estimate vehicle bank angle and rate gyro biases. The associated Kalman filter is low-order, and thus simpler to implement, compared to other methods which are not based on the aircraft kinematics. Furthermore, this simple method is as effective as other methods when the aircraft bank angle is not very large.

4.1 Prior Work on Attitude Estimation

4.1.1 Traditional Attitude Heading Reference Systems with Inertial Navigation System

In the traditional attitude and heading reference systems (AHRS) with inertial navigation system (INS), the Euler angles are computed by the integrations of the rate gyro outputs. The drifts due to the integrations are corrected by accelerometers and a compass. The accelerometers are used to correct pitch and roll errors using the fact that the specific forces that they sense tend to average in the direction of the local vertical. A magnetic compass is used to correct the vehicle heading angle. The drawback of this method is that it requires rather high quality, low-drift inertial sensors.

4.1.2 INS/GPS Integration

There are many methods for the integration of inertial sensors with GPS. The integration architecture can be classified into uncoupled, loosely coupled, or tightly coupled config-

urations. In the uncoupled architecture the INS and GPS systems independently yield navigation solutions, and then they are combined by some form of selection logic or complementary filter. In the loosely coupled configuration the outputs of the GPS receivers, such as position and velocity, are combined with inertial sensors using kinematic equations. In the tightly coupled architecture, pseudo ranges and delta ranges in the GPS receivers are directly combined with inertial sensor outputs. The INS/GPS integrations are usually costly and complex in implementation.

4.1.3 Multi-Antenna GPS based Attitude Determination

The multi-antenna GPS based attitude determination method [9, Cohen] requires at least 3 GPS antennas, at different locations on a platform, and uses carrier phase differences to determine the Euler angles of the vehicle; to a resolution of approximately 1 to 2 degrees. Performance depends on the baseline length - the separation distances among the GPS antennas. The attitude solution can be combined with inertial sensors in a complementary filter to overcome the low sampling frequency of GPS receivers. The drawbacks of this method are the multi-path, the integer ambiguity problem in the differential carrier phase, and the need for vehicle baseline dimensions of about one meter to achieve 1 to 2 degree accuracies.

4.2 Prior Work on Attitude Estimation Using Aircraft Kinematics

4.2.1 Bank Angle Estimation Using a Complementary Filter with Roll and Yaw Rate Gyros

Aircraft attitude estimation algorithms can be greatly simplified if the aircraft kinematics are introduced. A mechanization which is widely used for the bank angle estimation is the complementary filter configuration, as shown in Figure 4-1 (a). In this configuration, roll and yaw rate gyros are used. High frequency bank angle information is obtained by the integration of the roll rate gyro output and a high pass filter. Low frequency motion is estimated with the help of aircraft kinematics. Steady state turn dynamics are assumed, where a vehicle bank angle is directly related to turning rate, which is further approximated

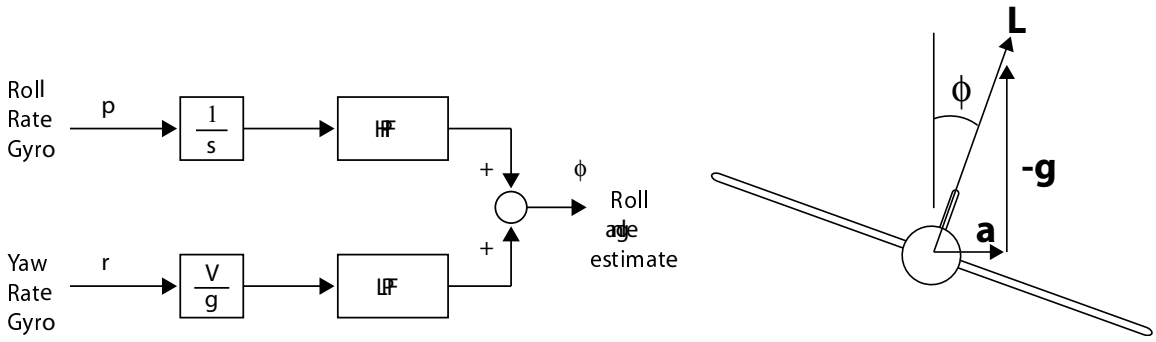

(a) Complementary Filter with Roll and Yaw Gyros

(b) Single-Antenna GPS Based Aircraft Attitude Determination

Figure 4-1: Attitude Estimations based on Aircraft Kinematics

by the vehicle yaw rate.

$$\phi \approx \frac{V_1}{g} r$$

where V_1 is the nominal velocity and g is gravity constant. This approximation to roll angle is low pass filtered with the cutoff frequency chosen based on gyro performance and vehicle dynamics.

One of significant problem in this estimation architecture is that the resulting bank angle estimate can be biased if either of the rate gyros has a bias.

4.2.2 Single-Antenna GPS Based Aircraft Attitude Determination

In 1999, Kornfeld[28] demonstrated a single-antenna GPS based system. First, the algorithm of the single-antenna GPS based aircraft attitude determination requires the estimation of acceleration from the GPS receiver. This is done by Kalman filter implementation under kinematic relations. Then, the acceleration vector in a local inertial frame is combined with the gravity vector to give an estimate of the lifting vector as shown in Figure 4-1 (b). If the aircraft flies in coordinated fashion its attitude is determined.

A limitation of this method is the rather large estimation time constants required to infer accurate acceleration. Typically the filter time constants must be of the order of 0.5 seconds, which prevents the use of this approach for high bandwidth control of small UAVs.

4.3 Simple, Low-order Attitude Estimation Combining Aircraft Kinematics, GPS and Low Quality Inertial Sensors

As a means of providing an effective source of attitude information, using low cost inertial sensors and GPS, a Kalman filter was developed to combine these two sources of information based on aircraft kinematic relationships. The details of this filter are reported in the following subsection.

4.3.1 Estimation of Bank Angle and Biases in Roll/Yaw Rate Gyros

A model of aircraft kinematics which is the basis for a Kalman filter that combines roll and yaw rate gyro outputs with GPS information is summarized in Figure 4-2. The external

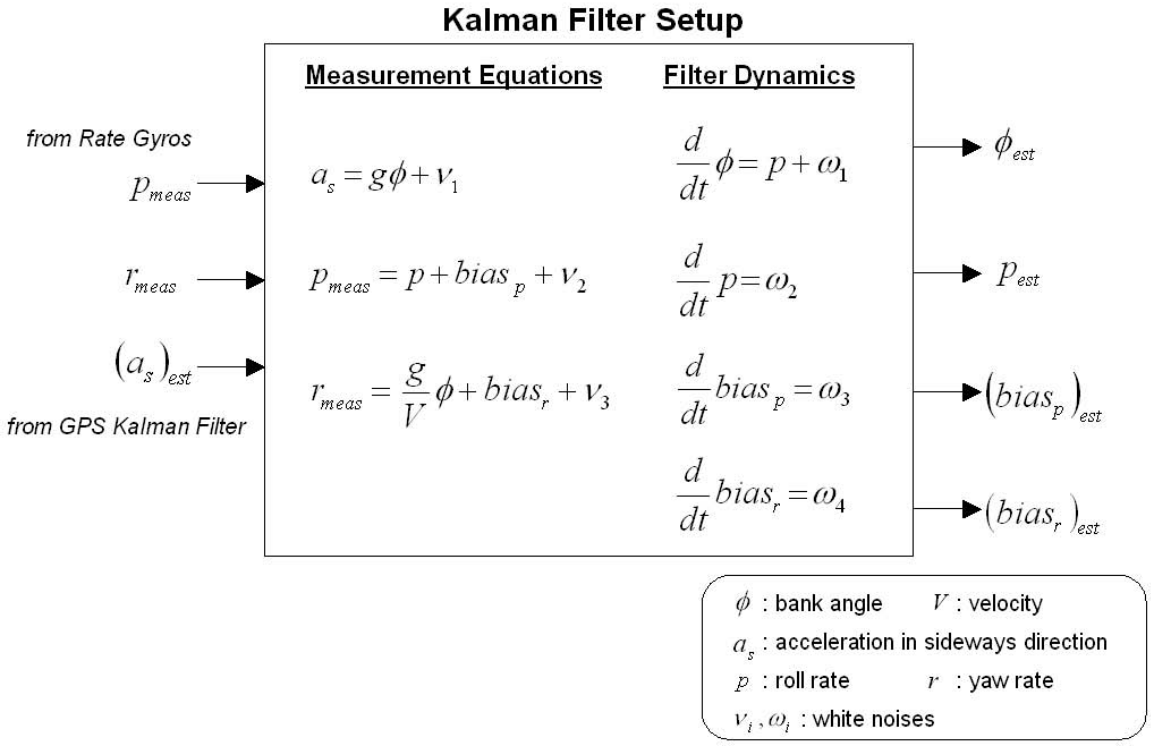

Figure 4-2: Kalman Filter Setup for Estimation of Bank Angle and Roll/Yaw Rate Gyro Biases (The lateral acceleration a_s is estimated from GPS Kalman filter described in Section D.1.)

three inputs to the filter are the roll and the yaw rate gyro measurements and the vehicle sideways acceleration in the horizontal plane of the local inertial frame as defined in Figure 4-

3. This acceleration is estimated from the GPS Kalman filter described in Section D.1 by

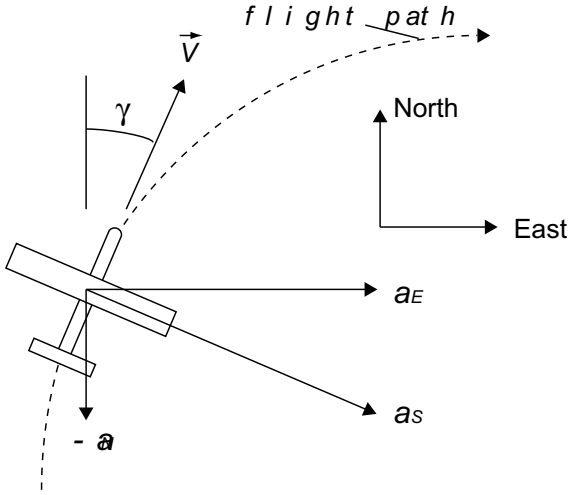

Figure 4-3: Definition of Sideways Acceleration a_s

the relation:

$$a_s = -a_N \sin\gamma + a_E \cos\gamma$$

where a_N and a_E are acceleration estimates in north and east directions from the GPS Kalman filter, and γ is the vehicle bearing angle, which is inferred from GPS velocity vector by

$$\gamma = \tan^{-1} \frac{V_E}{V_N}$$

The sideways acceleration a_s is used in the measurement equation in the Kalman filter setup. This value is related to bank angle by

$$a_s = g\phi + \nu_1$$

Here ν_1 is white noise, whose strength should include not only the estimation error but also the other ignored dynamics in this approximation. A standard deviation of $\sigma_{\nu_1} = 3.0\ m/s^2$ was used in the discrete Kalman filter design.

The second equation

$$p_{meas} = p + bias_p + \nu_2$$

which includes both bias and measurement noise, models the roll rate gyro measurement. A standard deviation of $\sigma_{\nu_2} = 0.028\ rad/s$ was used in the discrete filter design. This noise level was obtained from an experiment in the presence of engine vibration.

The last measurement equation, that relates bank angle to yaw rate, is for the yaw rate gyro measurement

$$r_{meas} = \frac{g}{V}\phi + bias_r + \nu_3$$

The associated measurement bias and noise are also included. The assumed standard deviation for the measurement noise was chosen such that it includes not only the measurement noise but also the ignored dynamics in this approximation. A standard deviation of $\sigma_{\nu_3} = (3.0\ m/s^2)/(25\ m/s)$ was used in the Kalman filter design.

There are four state variables in the filter dynamics. The first equation

$$\frac{d}{dt}\phi = p + w_1$$

relates the bank angle to the roll rate by an integration. The second equation

$$\frac{d}{dt}p = w_2$$

models roll rate as a brownian motion with a white noise derivative. The last two equations

$$\frac{d}{dt}bias_p = w_3 \qquad \frac{d}{dt}bias_r = w_4$$

model the biases in the two rate gyros as brownian motion. Small white noise powers are used in the Kalman filter in order to prevent the filter gains from approaching zero and also to take into account the fact that the gyro biases drift with time. For the process noises the following white noise strengths were used:

$$\Phi_{\omega_1} = 0.02^2\ [rad/s]^2,\ \Phi_{\omega_2} = 0.1^2\ [rad/s^2]^2,\ \Phi_{\omega_3} = \Phi_{\omega_4} = 0.001^2\ [rad/s^2]^2$$

The filter sampling rate was 40 samples per second.

It is interesting to investigate the resulting transfer functions from the measurement inputs to the estimation outputs under steady state. Their magnitudes are summarized in the Figure 4-4. All the transfer functions in the plots are normalized for easier interpretation.

Figure 4-4 (a) shows the transfer functions for the outputs of the bank angle estimation from the inputs of the three measurement sources. In the low frequency range GPS information dominates. This removes roll or yaw rate gyro biases. In the middle frequency range both the yaw rate gyro measurement and GPS information are primarily used. In the high frequency range the integration of the roll rate gyro output is used. It can be seen

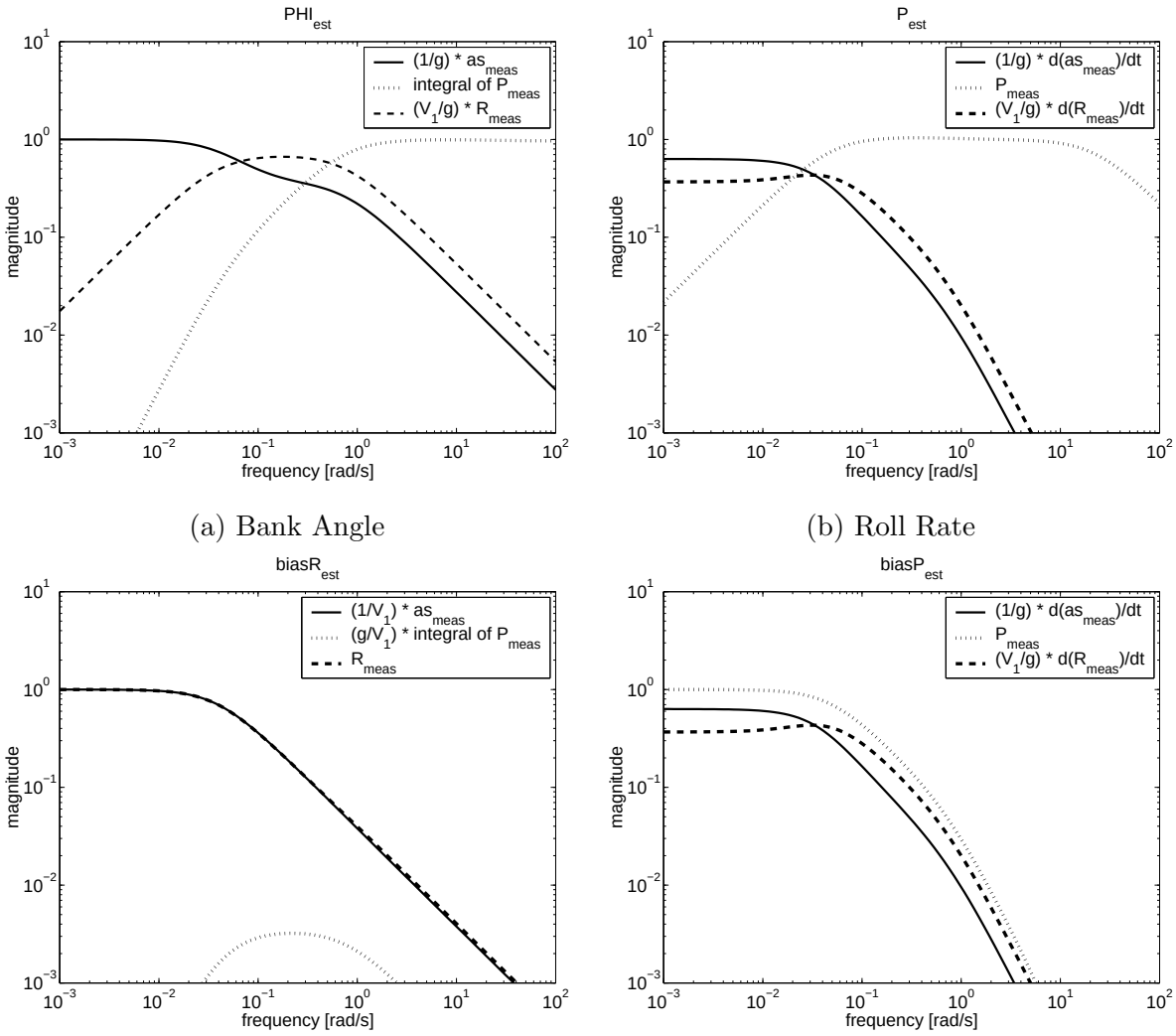

(a) Bank Angle

(b) Roll Rate

(c) Bias in Yaw Rate Gyro

(d) Bias in Roll Rate Gyro

Figure 4-4: Contributions of Measurements on Estimates in Lateral Filter

that the problem of the biased estimate in the complementary filter described in Section 4.2 is now removed by the inclusion of the GPS information.

Figure 4-4 (b) shows the transfer functions for the roll angle estimation from the inputs of the three measurement sources. The roll rate gyro is mostly used in the wide mid-frequency band. But in the low frequency range the GPS and yaw rate gyro are used to correct any bias in the roll rate gyro.

Figure 4-4 (c) shows the transfer functions for the estimation of the yaw gyro bias from the inputs of the three measurement sources. First, it is noted that the roll rate gyro doesn't have a significant effect for the correction of the yaw gyro bias. Second, the graph indicates

that the other transfer functions are identical low pass filters. But the investigation of the phase revealed that there is a phase difference of 180 degrees between the two. Thus, if there is a bias in the yaw rate gyro, the outputs of the two transfer functions will be different and won't be cancelled with each other in the subtraction. This will indicate the rate gyro bias.

Figure 4-4 (d) shows the transfer functions for the estimation of the roll gyro bias from the inputs of the three measurement sources. There is a 180 degrees of phase difference between transfer function from the roll rate gyro measurement and the sum of the other two transfer functions. This can be understood in a similar way as for the case of the yaw gyro bias estimation.

4.3.2 Bias Estimation in Pitch Rate Gyro

Another simple Kalman filter was constructed to estimate the bias in a pitch rate gyro. The associated Kalman filter is summarized in Figure 4-5. Two external inputs to this filter are

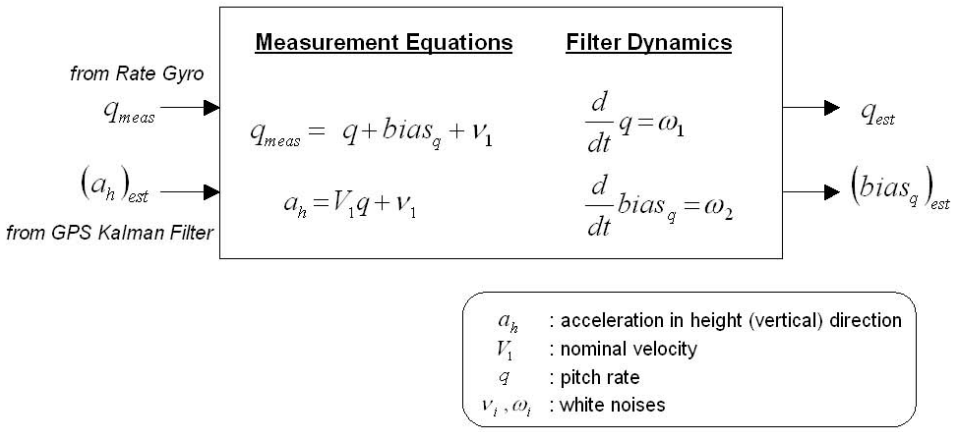

Figure 4-5: Kalman Filter Setup for Estimation of Pitch Rate Gyro Bias (Note: for turning with large bank angles, replace $(a_h)_{est}$ with $(a_h)_{est} + Vr|\tan\phi|$)

the pitch rate measurements and the acceleration estimate in the vertical(altitude) direction. The first measurement equation

$$q_{meas} = q + bias_q + \nu_1$$

is for the rate gyro measurement. Bias and noise are included. From the experiment under engine vibration a standard deviation of $\sigma_{\nu_1} = 0.02\ rad/s$ was obtained. The vertical

acceleration a_h is related with the pitch rate by

$$a_h = Vq + \nu_2$$

in the measurement equation. It is noted that the centripetal relation is used. ν_2 is the white noise, whose strength should be chosen such that it includes not only the estimation error of this variable but also the ignored dynamics in this approximation. A standard deviation of $\sigma_{\nu_2} = 4.0\ m/s^2$ is used in the discrete Kalman filter design.

The filter dynamics

$$\frac{d}{dt}q = w_1 \qquad \frac{d}{dt}bias_q = w_2$$

has two state variables to be estimated. They are the pitch rate and pitch rate gyro bias. Process noises are directly imposed on the time derivatives of these variables. White noise strengths of $\Phi_{\omega_1} = 0.1^2\ [rad/s]^2$ and $\Phi_{\omega_2} = 0.001^2\ [rad/s]^2$ were used in the Kalman filter design. The filter has a sampling rate of 40 samples per second.

The associated transfer functions from the measurement inputs to the estimation outputs under steady state are summarized in the Figure 4-6. All the transfer functions in the graphs

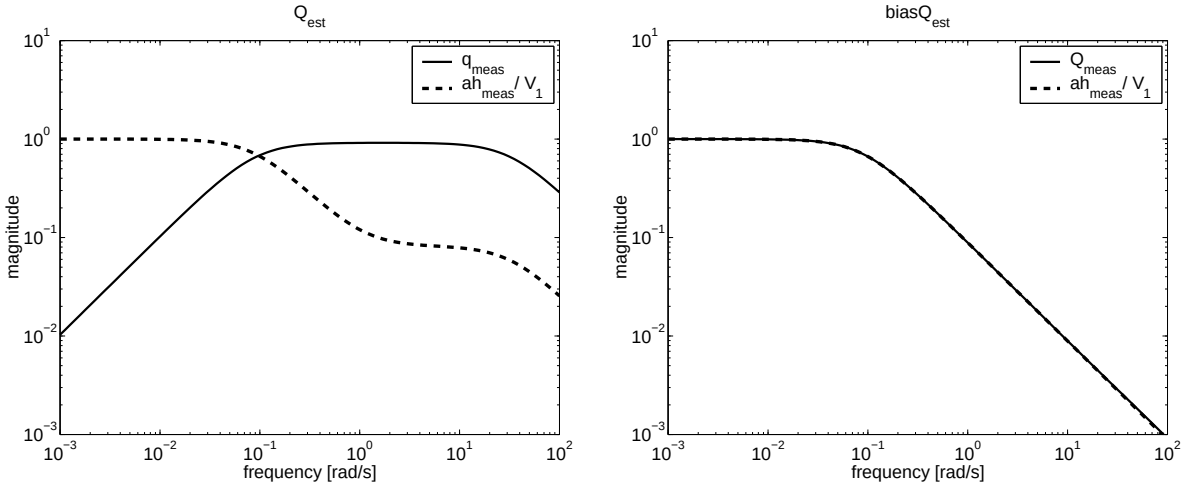

(a) Pitch Rate (b) Bias in Pitch Rate Gyro

Figure 4-6: Contributions of Measurements on Estimates in Longitudinal Filter

are normalized.

Figure 4-6 (a) shows the transfer functions for the output of the pitch rate estimation from the inputs of the two measurement sources. It indicates that the GPS is used primarily

in the low frequency range. In high frequency range, the pitch rate gyro is the primary source.

Figure 4-6 (b) shows the transfer functions for the output of the pitch gyro bias estimation from the inputs of the two measurement sources. The two transfer functions are low pass filters and they have 180 degrees of phase difference.

4.3.3 Flight Test Data : Rate Gyro Bias Estimation

Figure 4-7 shows flight test data regarding the gyro bias estimations. In this test, the Mini

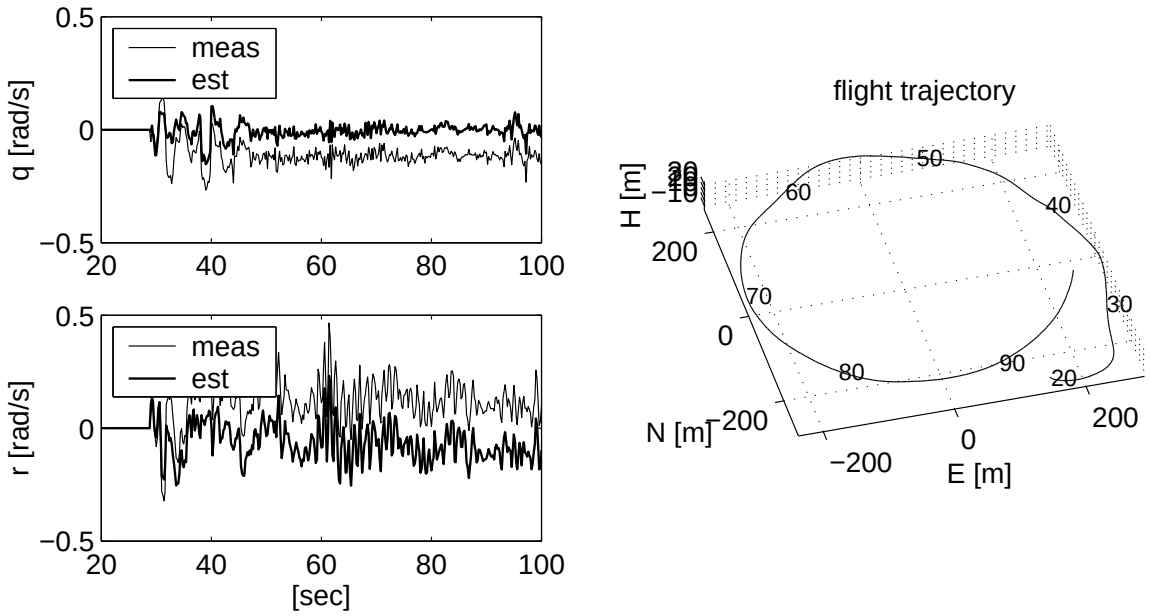

Figure 4-7: Flight Test Data : Rate Gyro Bias Estimation

vehicle was controlled manually to perform a left turn with the average bank angle of 10 degrees while maintaining the altitude within 20 meters as shown in the trajectory plot. The correct pitch rate under this turn should be 0.01∼0.02 rad/s considering the vehicle speed and the radius of the circular trajectory. But the measurement value of the pitch rate gyro was approximately -0.1 rad/s. This biased indication from the rate gyro output is corrected by the Kalman filter, as indicated by the first plot, which chose a mean pitch rate of approximately zero. Similarly, the positive values of the yaw rate gyro measurement, indicating a right turn of the vehicle, are also biased. This is corrected by the Kalman filter, as shown in the plot.

4.3.4 Comparison with a Multi State Extended Kalman Filter

This section compares the low-order attitude estimation method with other method which is not based on the aircraft kinematics. The following is the description of an Extended-Kalman filter [7, Chatfield], [41, Rogers] that was used as a counterpart for this comparison.

Filter Dynamics equations

$$\begin{aligned} \dot{\mathbf{p}}_L &= C\mathbf{v}_B \\ \dot{\mathbf{v}}_B &= \mathbf{a} + C^{-1}\mathbf{g} - \Omega_3\mathbf{v}_B \\ \dot{\mathbf{q}} &= -\tfrac{1}{2}\Omega_4\mathbf{q} \\ \dot{\gamma}_{P,Q,R} &= \mathbf{w}_I \\ \dot{\gamma}_{a_x,a_y,a_z} &= \mathbf{w}_{II} \end{aligned} \tag{4.1}$$

with

$$\begin{aligned} \mathbf{a} &= \mathbf{a}_m + \gamma_{\mathbf{a}} + \nu_{\mathbf{a}} \\ \Omega_3 &= \Omega_{3_m} + \gamma_{\Omega_3} + \nu_{\Omega_3} \\ \Omega_4 &= \Omega_{4_m} + \gamma_{\Omega_4} + \nu_{\Omega_4} \end{aligned} \tag{4.2}$$

Measurements

$$\mathbf{p}_{L_{meas}},\ \mathbf{v}_{L_{meas}} :\ \text{from GPS}$$
$$\psi :\ \text{from a compass}$$

Notation

subscript L	:	local earth-fixed inertial frame
subscript B	:	vehicle body frame
subscript m	:	measurement
$\mathbf{p}$	:	vehicle position vector
$\mathbf{v}$	:	vehicle velocity vector
$\mathbf{g}$	:	$=[0\ 0\ g]^T$, gravity vector
$\mathbf{a}$	:	specific force coordinatized into vehicle body axis, measurements of strapdown ideal 3-axis accelerometer
$\mathbf{q}$	:	$=[q_0\ q_1\ q_2\ q_3]^T$, quaternion
$P,\ Q,\ R$	:	roll, pitch, yaw angular rates
ψ	:	heading angle
γ	:	bias
ν	:	noise
C	:	Rotational Transformation matrix from body to earth-fixed coordinates

$$\Omega_3 \equiv \begin{bmatrix} 0 & -R & Q \\ R & 0 & -P \\ -Q & P & 0 \end{bmatrix}, \quad \Omega_4 \equiv \begin{bmatrix} 0 & P & Q & R \\ -P & 0 & -R & Q \\ -Q & R & 0 & -P \\ -R & -Q & P & 0 \end{bmatrix}$$

The first three vector relations in Equation 4.1 are the rigid body kinematics. Equation 4.2 models the measurements from the accelerometers and rate gyros. A total of 16 states are estimated in this extended Kalman filter. It is assumed that the GPS position/velocity information and a heading from a compass are available. They are included in the measurements equations in the Kalman filter setup.

Figure 4-8 shows simulation results comparing the performance of the low-order Kalman filter with that of the extended Kalman filter. In this simulation, the airplane's aileron angle was set to be a certain non-zero value. The vehicle followed a spiral path with gradual increase of the bank angle. The associated 3-D trajectory plot is shown in the figure.

For the bank angle estimations, the simulation result indicates that the simple method follows the bank angle upto about 40 degrees, and after that the estimation value departs from the true value. On the other hand, the extended Kalman filter follows the true value throughout the flight. The reason for the difference is due to the use of the simplified

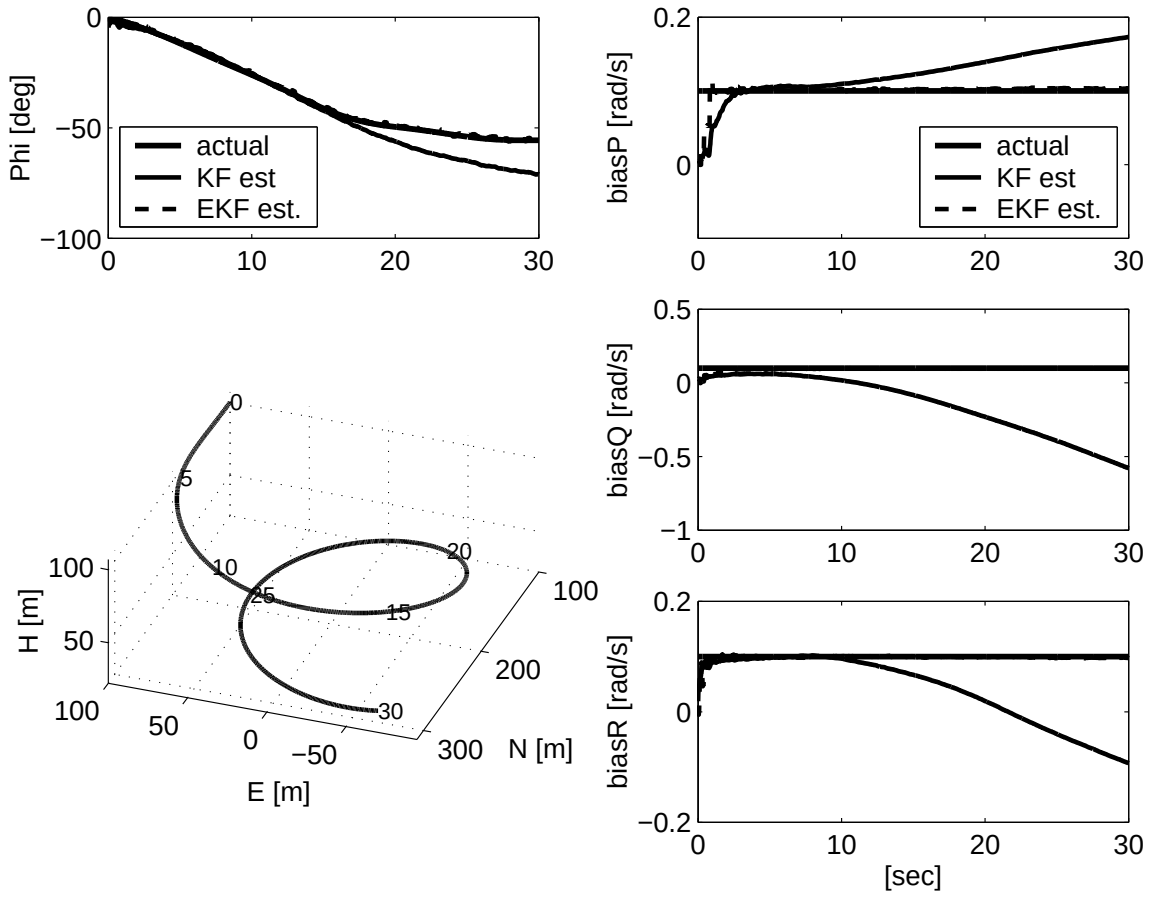

Figure 4-8: Comparison with Other Method under Spiral Motion in Simulation

relation of

$$a_s \approx g\phi$$

while a more realistic relation for the steady turn is

$$a_s \approx g \tan \phi$$

For example at t=30 seconds in the simulation, the actual bank angle is about 52 degrees while the estimation from the simple method is about 73 degrees, and this can be explained by

$$(180/\pi) \cdot \tan 52^o \approx 73^o$$

Next, regarding the gyro bias estimations, the simple method follows the true value until the vehicle bank angle is within about 30 degrees, and after that the estimates depart from

the true values while the extended Kalman filter follows the true values of the gyro biases throughout the flight.

4.4 Summary

This chapter proposed a simple and low-order aircraft attitude estimation method which combines the aircraft kinematics, GPS outputs, and low quality inertial sensors. In simulations it was also shown that the new estimation method works as well as other complex methods when the aircraft bank angle is not very large.

Chapter 5

Guidance for Phase II of Mid-Air Rendezvous

It is required to bring the two UAVs within a few meters of separation in the Phase II rendezvous procedure. The stand-alone GPS used as a primary position sensor for Phase I is not accurate enough for Phase II. Another type of sensor needs to be added for Phase II. The team considered two options. One is carrier-phase differential GPS and the other is an optical sensor. With the carrier-phase differential GPS it was envisioned that when the two vehicles are close to each other there is a high probability that a multi-path problem could occur, which will deteriorate the quality of the estimate of the relative position. For this reason the optical sensor option was chosen. Thomas Jones in the project team developed an optical sensor system. It is composed of two main elements. They are depicted in Figure 5-1. The first element is a target light on the OHS Parent vehicle which it faces backward. It generates high-power infra-red pulses at a certain frequency(4 kHz). The second element is the camera with a detection photodiode. This is mounted at the front of the Mini vehicle. This element measures the angles(η_h, η_s in Figure 5-1) to the target. Thus, the output of the optical sensor system is the relative bearing of the line-of-sight between the two vehicles.

Initially, the team considered an approach in which two camera sensors are mounted on each side of the Mini wing in order to get a relative position estimate from stereo-visioning. Then, a relative position hold could have been tried during the Phase II. But because of the hardware complexity and the limited time available in the project, the project team chose

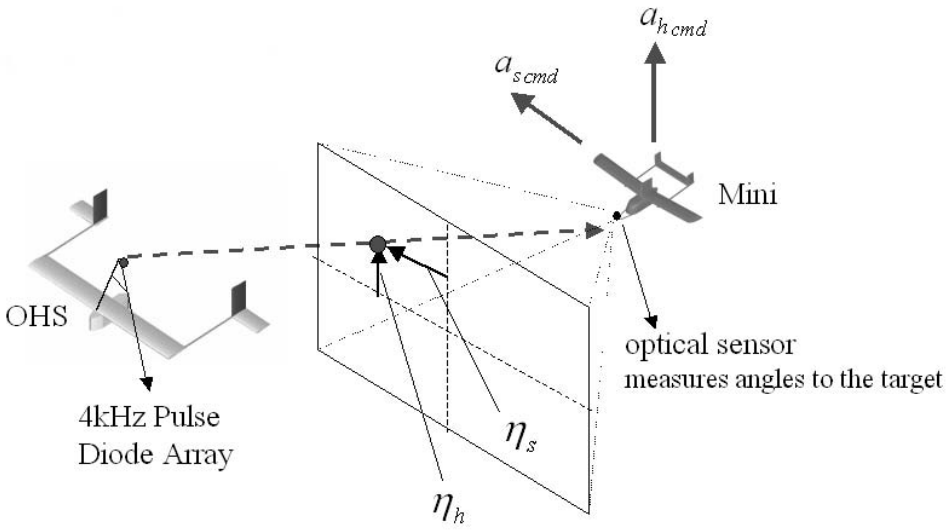

Figure 5-1: Phase II Optical Sensor and Control/Guidance Concept

a single-camera approach and decided to make the Mini vehicle approach the Parent with a relatively small closing velocity (∼1 m/s) while holding the line-of-sight angle.

Regarding the guidance laws, [15, Guelman], [37, Yuan & Hsu], and [20, Jensen] discuss the extension of the proportional navigation guidance for the rendezvous problem, where the relative velocity components not only normal to but also along the LOS are driven to zero when the two vehicles meet. But the algorithm is not adequate for the problem of the aircraft rendezvous because it requires the maneuver capability to generate acceleration in any direction and the measurement of the relative range. Thus, the conventional proportional navigation is used primarily for the guidance. In estimating the LOS rate with the optical sensor the change of the bearing angles are compensated by the onboard inertial sensors because the LOS rate required in the proportional navigation is the one relative to the inertial frame. The computation of the LOS rate is described in Appendix E.

The following sections report the guidance logic, the interface between the guidance logic and inner-loop controllers, and the associated performance analysis.

5.1 Phase II Guidance Logic

A pure proportional navigation $a_{cmd} = N'V_c\dot{\lambda}$ was not used. Some modification is needed because the Mini vehicle is required to approach the Parent from as directly behind as

possible. There are two reasons for this requirement. One is due to concern for collision. The wing tip of the Mini vehicle should not touch the tail of the OHS Parent while the Mini is approaching the Parent from behind. The other reason came from the limitation of the optical sensor that the team built. It turned out that the developed optical sensor system has a relatively narrow field of view of ± 20 degrees. Thus, the Mini vehicle is required to always be somewhere in the $\pm 20^o$ region directly behind the OHS Parent, in order to ensure that the light source is always within the field of view. Another modification to pure proportional navigation is the use of the Parent acceleration in generating the acceleration command for the Mini vehicle. The addition of the acceleration of the target maneuver is known to work better than the original basic form of proportional navigation [48, Zarchan]. This was done in the lateral direction to account for acceleration in the turn which maintains the Parent in a circular path. The resulting sideways acceleration command is expressed below by the sum of the pure proportional navigation expression and two additional terms :

$$a_{s_{cmd}} = N' V_c \dot{\lambda_s} + a_{s_{OHS_{nominal}}} + K_{\eta_s} \cdot \eta_s$$

where

N'	:	proportional navigation constant
V_c	:	closing velocity
$\dot{\lambda}_s$	:	line-of-sight rate
$a_{s_{OHS}}$	:	sideways acceleration command of the OHS Parent during the turn
K	:	constant gain
η	:	camera angle to the target

- The first term $N' V_c \dot{\lambda_s}$ is the original expression for the proportional navigation. The closing velocity was set to be a constant value, 1 m/s. Thus, the velocity command of the mini is set to V_{OHS}+1 m/s to have the required closing velocity.

- The last term $K_{\eta_s} \cdot \eta_s$ is for the feedback on the angle to the target. It is added to ensure that the Mini will follow the OHS Parent from behind, and also to ensure that the light source is always within the field-of-view of the camera.

Similarly, the vertical direction acceleration command is generated by:

$$a_{h_{cmd}} = N' V_C \dot{\lambda_h} + K_{\eta_h} \cdot \eta_h$$

The the last term is added to ensure that the target on the Parent vehicle is within the field-of-view of the camera.

5.2 Acceleration Commands to Inner-Loop Controller and Unconventional Control Surfaces

The output of the guidance logic is the acceleration command on each axis. This section describes how the acceleration command is executed. The same low level controllers - the bank angle controller in the lateral dynamics and the LQ controller in longitudinal dynamics - which were used in the Phase I, were used for the Phase II.

Lateral-Directional Configuration

As described earlier, the Mini vehicle has both conventional ailerons and rudders to control lateral motion and a direct side force vertical control surface. Figure 5-2 shows how the sideways acceleration commands generated from the guidance algorithm are handled in the low level controller. It also shows how the extra control surface - the sideways control surface on the vertical fin of the Mini UAV - is combined to enhance the control capability. In the low level controller there is the bank angle controller which was used in Phase I. The

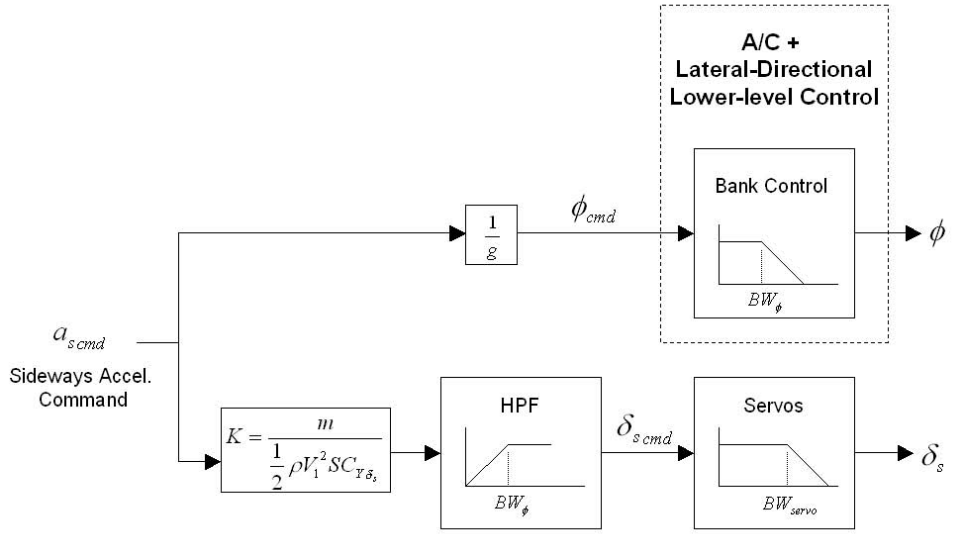

Figure 5-2: Phase II Lateral Guidance/Controller Structure

acceleration command is first converted to a bank angle command by relating it with the gravity constant as shown in the diagram.

The response of the sideways control surface deflection from its command is faster than that of the bank angle deflection from its command. Therefore, the sideways control surface can be added to create the acceleration more rapidly. This idea is accomplished by adding a high-pass filter on the channel for the sideways control surface as shown in the diagram. The cutoff frequency of the high-pass filter is chosen to be at the bandwidth of the bank angle controller.

Longitudinal Configuration

Figure 5-3 shows how the altitude direction acceleration commands generated from the guidance algorithm is handled in the low level controller. The same low level LQ controller

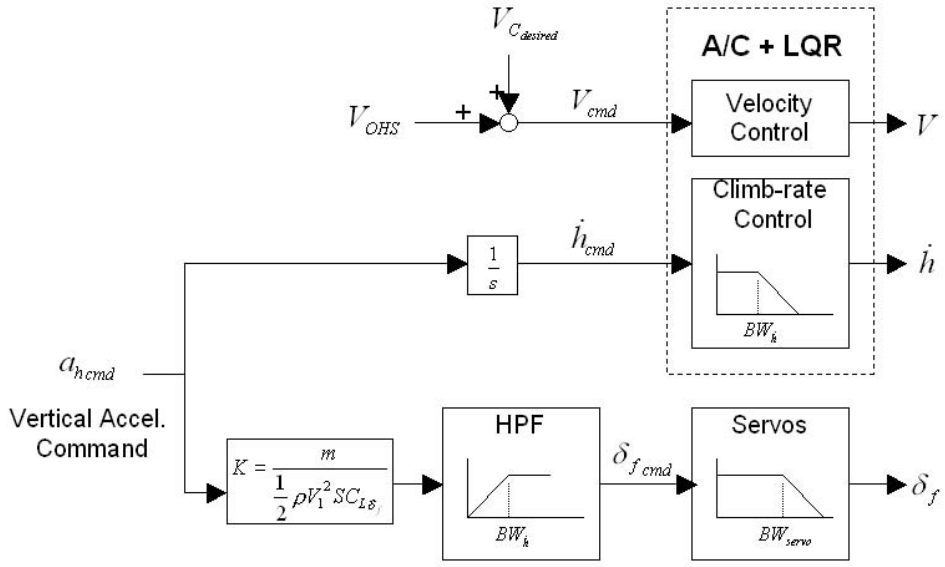

Figure 5-3: Phase II Longitudinal Guidance/Controller Structure

is also used here. The LQ controller takes the vertical velocity command as an input. Thus, the acceleration command from the guidance law is integrated so as to create an altitude rate command, for control at lower frequencies.

In order to create high bandwidth control, the flap mode of the flaperons is used. The cutoff of the high-pass filter on the flaperon channel is chosen at the frequency of the bandwidth of the clime-rate controller in LQR.

Additionally in the longitudinal direction, the speed command for the Mini is generated by adding $V_{C_{desired}}$ =+1 m/s to the speed of the Parent in order to have the desired closing velocity.

5.3 Linearization and Method of Adjoints for Miss Distance Analysis

The *miss distance* analysis deploying the adjoint technique, which is widely used in tactical missile guidance system design, is explained in [48, Zarchan]. This section describes the application of the miss distance analysis on the Phase II control system. Miss distance is nominally the distance by which one vehicle misses the other, and is formally defined as the distance between the two vehicles when their closing velocity changes sign. The outline of the analysis procedure is given first. A detailed description on each step is given in the following sections.

First, the Phase II engagement model is linearized for both the longitudinal and lateral dynamics. The linearization is a good approximation in the Phase II situation as long as the camera angle and line-of-sight rate remain small, which is essential for successful rendezvous. It is assumed in this analysis that the Mini vehicle approaches the Parent with a constant closing velocity. Then, it should be noted that the line-of-sight rate represents an increasing gain as the Mini vehicle approaches the Parent. Therefore, the resultant linearized model becomes a *time-varying* system.

The Method of Adjoints was used to predict the miss distance for the time-varying linear system. The following effects were considered as the disturbance sources on the miss distance.

- the effect of initial position of the Mini vehicle when Phase II is initiated
- the effect of initial heading of the Mini vehicle when Phase II is initiated
- the effect of wind in the vehicle x,y,z-axes

Analysis on Longitudinal Dynamics

Figure 5-4 shows the Phase II longitudinal model. In the diagram, the Mini vehicle, on the right side, is chasing the target on the left side. θ is the vehicle pitch angle, and η_h is

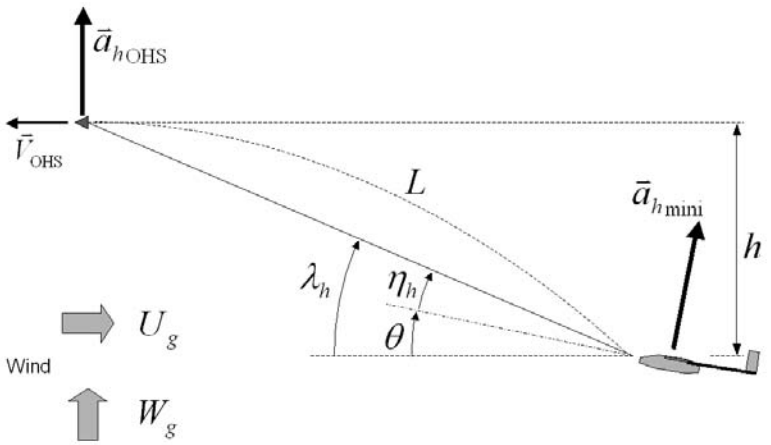

Figure 5-4: Phase II Longitudinal Engagement Model for Linearization

the vertical angle to the target relative to the vehicle body x-axis. h is the separation in vertical direction. $\vec{a}_{h_{OHS}}$ and $\vec{a}_{h_{mini}}$ are the accelerations in the vertical direction of OHS Parent and Mini respectively. By inspection of Figure 5-4, the relative acceleration can be written as

$$\ddot{h} = a_{h_{OHS}} - a_{h_{MINI}}$$

by using small angle approximations for θ and η_h. The expression for the line-of-sight angle can be linearized with the small-angle approximations, yielding

$$\lambda_h = h/L$$

In a linearized analysis the closing velocity(V_c) is treated as a positive constant [48, Zarchan]. Since the range(L) must go to zero at the end of the flight, the range equation is linearized as

$$L = V_c(t_F - t)$$

where V_c is a closing velocity and t_F is the total flight time, or the final flight time. Thus, the quantity $t_F - t$ is the time to go until the end of the flight. The linearized miss distance is defined to be the relative separation h between the MINI and OHS at the end of the flight, or

$$\text{Miss} = h(t_F)$$

Also, the angle to the target, in the longitudinal plane is

$$\eta_h = \lambda_h - \theta$$

It is assumed in the analysis that the OHS Parent vehicle is operating with tight control of its altitude so the acceleration $a_{h_{OHS}}$ is the effect of gusts (U_g and W_g) on that vehicle. However, for the Mini vehicle, the acceleration $a_{h_{MINI}}$ is the *sum* of gust effects and the effect of the guidance/control action on the Mini. All the above relations can be illustrated in the block diagram shown in Fig 5-5.

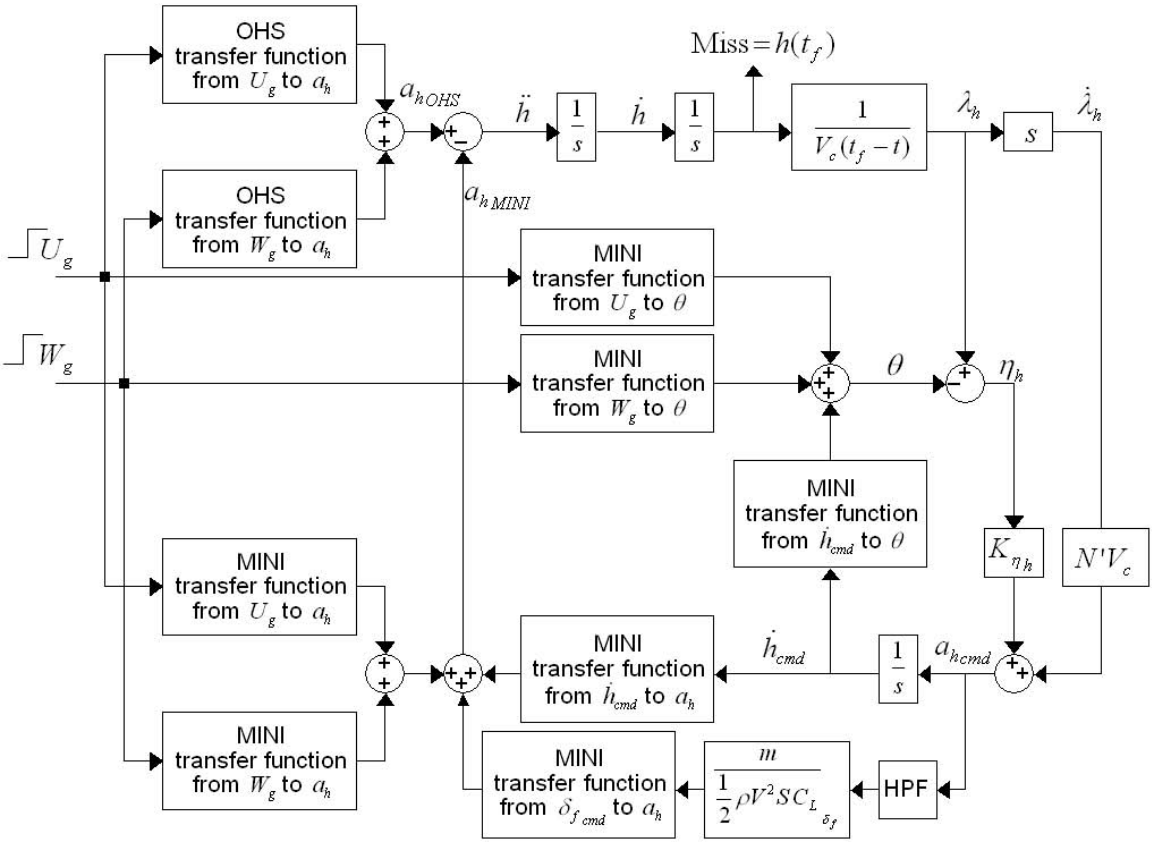

Figure 5-5: Phase II Longitudinal Linearized Engagement Model Homing Loop

It is emphasized again that the linear system in the block diagram is *time-varying*. This means that, for example, the response of the Mini vehicle to a certain type of gust will vary depending upon when the gust is applied. This is due to the fact that the LOS rate becomes more and more significant as the separation distance gets shorter and shorter, or as the time (t) approaches the final time (t_F). Another example would be the response to some initial altitude condition for different flight times (or different initial separation distances).

This characteristic of time-varying systems implies that in order to obtain the miss distance for various flight times or for various wind initiation times, many simulations would have to be performed in order to determine the associated miss distance for each case. The

method of adjoint saves this computation effort. The method is based on the system impulse response and can be used to analyze linear time-varying systems [48, Zarchan]. It is based on the fact that the impulse response of the original system h is related with the impulse response of the adjoint system h^* by

$$h^*(t_F - t_I, t_F - t_O) = h(t_O, t_I)$$

where t_I is the time of impulse application and t_O is observation time. This means that applying an impulse at time t_I and observing the output at time t_O, for the original system, is equivalent to applying an impulse at time $t_F - t_O$ and observing the adjoint output at time $t_F - t_I$ for the corresponding adjoint system. If the observation time is the final time($t_O = t_F$ to see miss distance, for example) the adjoint relationship becomes

$$h^*(t_F - t_I, 0) = h(t_O, t_I)$$

Therefore, an impulse applied at any time t_I and observed only at final time t_F in the original system is equivalent to applying an impulse at time zero in the adjoint system and monitoring the output at time $t_F - t_I$.

Figure 5-6 shows the corresponding adjoint model constructed by following the procedure described in [48, Zarchan]. In order to get a response to a step wind input an integrator is added as shown in the diagram. With this adjoint model miss distances due to step gust inputs and to initial altitude differences, for various flight times, are obtained in *one* computer run.

Figure 5-7 shows the adjoint simulation result. The comparison for the two cases - with and without using the flaperons - is also displayed. The first two graphs in Figure 5-7 are for miss distances with the input of unit(1 m/s) step gust U_g and W_g for various application times, which is the horizontal(x) axis of the graphs. The interpretation is, for example, if the Mini vehicle is 4 meters behind the Parent, then the remaining flight time is 4 seconds (because of the assumption of the 1 m/s of closing velocity), and if a unit step gust is applied at this moment, then the Mini will miss the OHS target by 0.02 meters.

The third plot in Figure 5-7 shows the miss distance due to the 1 meter of initial altitude difference for various flight times. The interpretation of this plot is that, for example, if the Mini is 6 meters behind and 1 meter above the Parent, then the Mini will miss the Parent target by about 0.05 meters, using the flaperon.

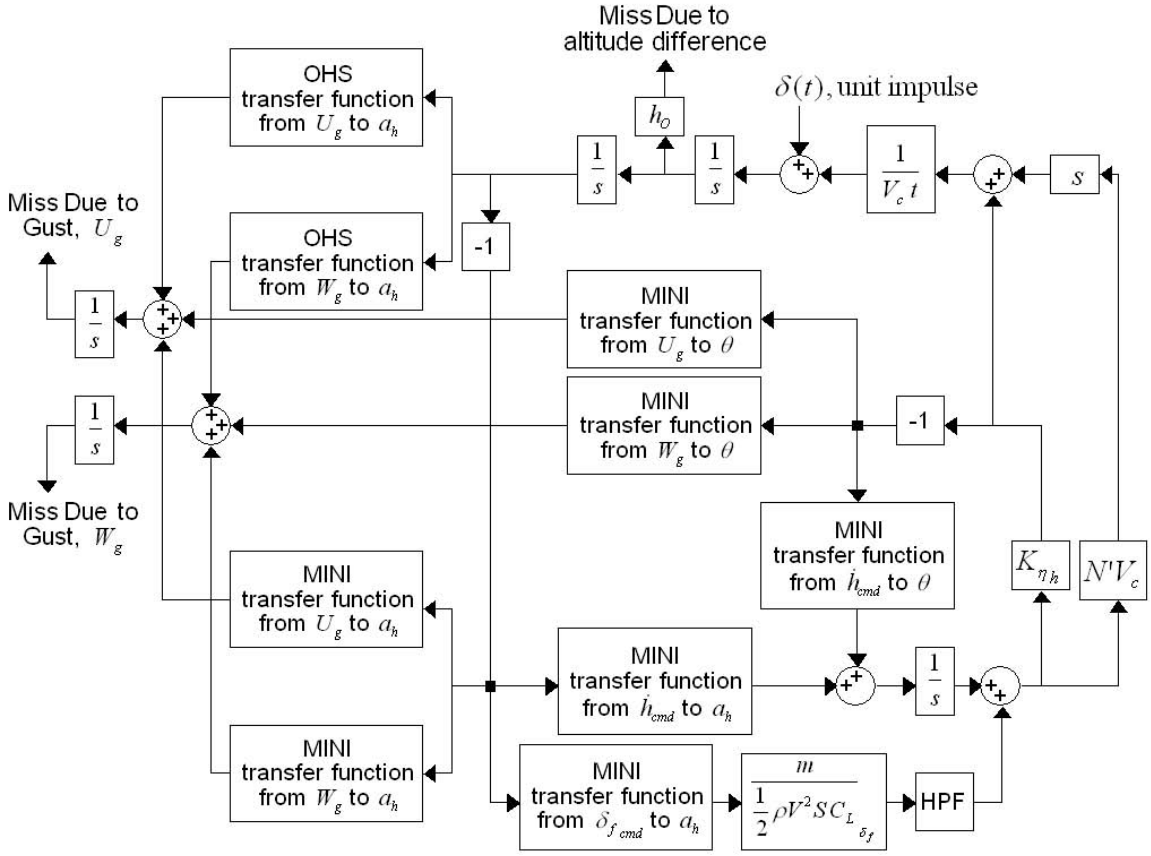

Figure 5-6: Adjoint of Phase II Longitudinal Engagement Model

The plots in Figure 5-7 indicate that the performance is significantly improved by using the flaperon. In general the miss distance depends on the speed of the response from the acceleration command to the actual acceleration. The bandwidth of the altitude rate control in LQR is about 1 rad/s, while the bandwidth of the control surface deflection is higher than 10 rad/s. Therefore, there is a significant benefit by adding the flaperon.

Analysis of Lateral Dynamics

A similar procedure was performed for lateral dynamics. Figure 5-8 shows a diagram for the lateral motion in Phase II, where ψ is the vehicle yaw angle, η_s is the angle to the target measured by the optical sensor, and y is the lateral displacement between the Mini and the target point of the OHS Parent.

Constructing the associated linear model and applying the method of adjoints leads to a similar analysis result, as shown in Figure 5-9. The figure shows the plots for miss distances

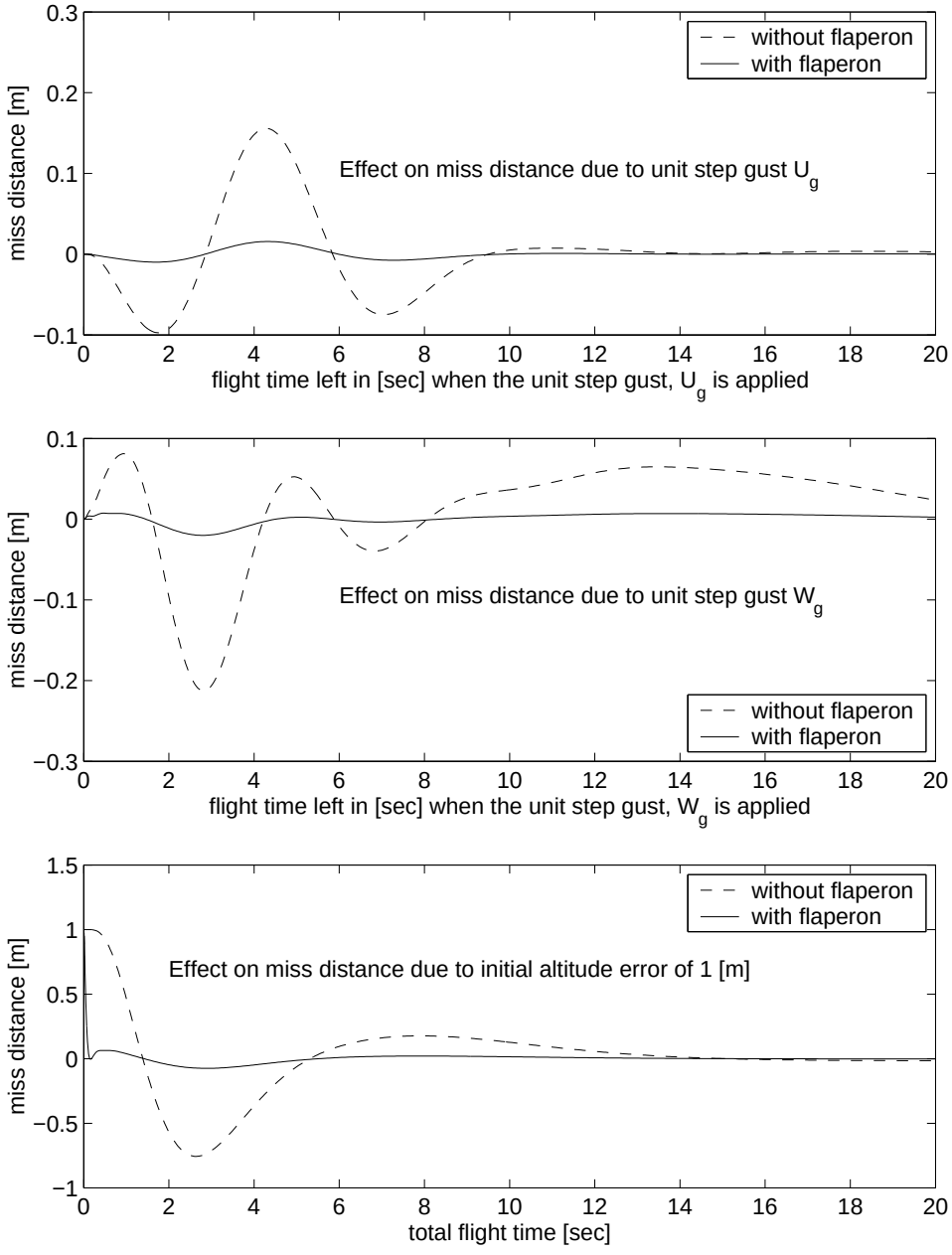

Figure 5-7: Miss Distances Due to Unit Step Gust U_g and W_g and Initial Altitude Difference of 1 Meter for Various Flight Times

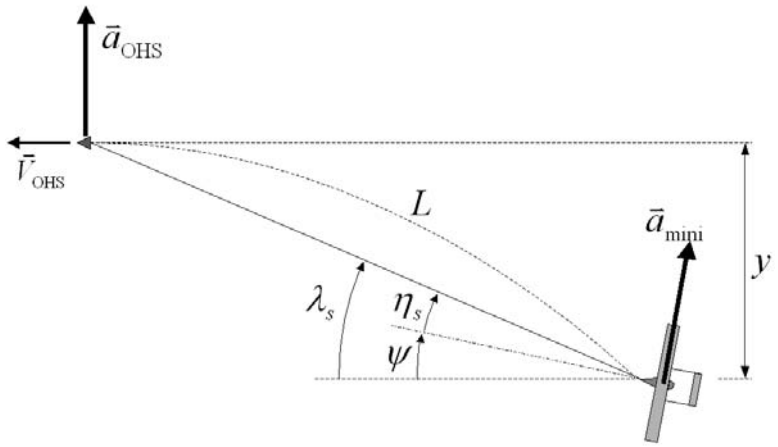

Figure 5-8: Phase II Lateral Engagement Model for Linearization

from the effect of the sideways gust W_g, initial heading angle error of 10 degrees, and initial sideways position difference of 1 meter, for various flight times.

Regarding the sideways control surface, saturation will easily occur for this control surface because its maximum acceleration value is only 0.1 g. Saturation cannot be included in the adjoint conversion. Therefore, the effect of the sideways control surface was not included in the analysis. However, the bank angle control alone seems sufficient as indicated in the miss distance plots. The reason for this is that the 3 rad/s of the bank control bandwidth is relatively high, compared to the 1 rad/s of the altitude rate control bandwidth.

5.4 Summary

This chapter presented the guidance algorithm for Phase II. A few modification were made on the proportional navigation to make the Mini vehicle to approach the OHS Parent from direct behind as much as possible. The same bank angle controller and LQ controller are deployed in Phase II as in Phase I. The interface between the acceleration command from the guidance logic and the low level controllers were discussed. The Phase II engagement model was linearized in longitudinal and lateral directions, then the method of adjoint was applied to predict the miss distances. Wind effect, initial position, and initial heading angle were considered as the disturbance sources in the prediction of the miss distance.

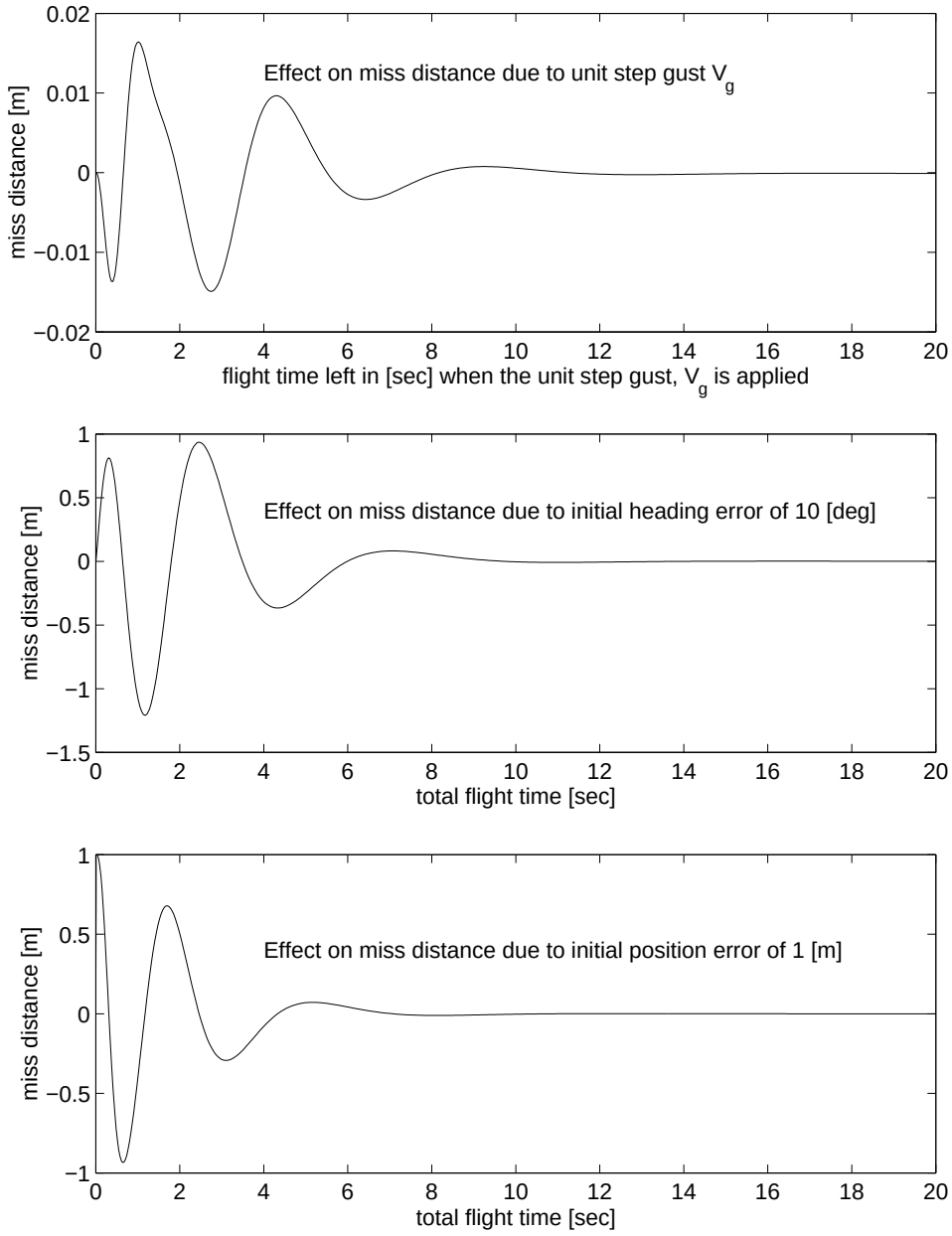

Figure 5-9: Miss Distances Due to Unit Step Gust V_g, Initial Heading Error of 10 Degrees, and Initial Sideways Position Difference of 1 Meter for Various Flight Times

Chapter 6

Flight Test Results

This chapter reports the flight test results. It first gives the individual flight test results on each aircraft and then provides the results of the Phase I flight test.

6.1 Flight Test of Individual Aircraft

Each aircraft should be controlled within a certain position error boundary during Phase I in order for the optical system to be engaged for the next phase because the optical system has limited operational range and field-of-view. Figure 6-1 shows an example of a worst-case situation where the Parent vehicle is offset to the left and the Mini to the right from the common desired flight path during the last stage of the Phase I. L is the operational range

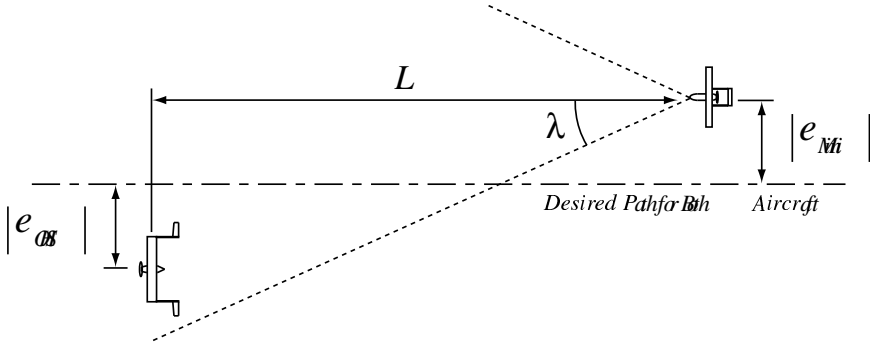

Figure 6-1: Requirements of Position Control Error Boundary of Each Vehicle Imposed by Optical Sensor

and λ is the half of the field-of-view angle of the optical sensor. In order to keep the OHS

target point within the field-of-view

$$|e_{Mini}| + |e_{OHS}| < L \sin \lambda$$

is required. With L=15 m and $\lambda = 20^o$ for the current developed optical sensor, $L \sin \lambda$ yields 5.1 meters.

The team performed a series of flight tests on each aircraft to validate the control systems before flying two aircraft at the same time for the rendezvous test. It was demonstrated that each individual aircraft could follow the commanded path within about 2 meters of position error in both longitudinal and lateral directions while also tracking the speed command within about 1 m/s of velocity error.

Figures 6-2 (a) and (b) show the flight test data for altitude hold and air speed tracking of both the Mini and the OHS Parent vehicles. The flight data in Figure 6-2 (a) indicates that the Mini aircraft followed its speed command within the error boundary of 1 m/s for the 88% of its flight time and held the altitude command within the boundary of 1 meter for the 90% of the flight time. Figure (b) is obtained from a flight test with the OHS Parent vehicle. It indicates that the aircraft followed its speed command within the error boundary of 1 m/s for the 86% of its flight time and held the altitude command within 2 meters for the 97% of the flight time. In both flight tests, the average wind condition was 5($\pm$1) m/s. The wind speed was obtained after the flight test by comparing the GPS velocity and air-speed sensor measurements.

Figure 6-3 shows the flight data for the Mini vehicle regarding the lateral guidance logic for trajectory following. The plot shows the 2-dimensional trajectory of the Mini vehicle (solid line) with a commanded desired trajectory (dotted line). This flight test was performed with a candidate Phase I trajectory path although there was no OHS Parent flying. The small numbers along the trajectory are the flight times recorded in the onboard avionics. This plot indicates that the vehicle follows the commanded trajectory quite well. When the Mini vehicle flies along the circle the lateral displacement between the vehicle and the desired path remained within $\pm$2 meters for the 75% of its flight time and within $\pm$3 meters for the 96% of the flight time.

A similar flight test was performed for the OHS Parent. Figure 6-4 shows the trajectory of the Parent vehicle and the commanded path. The autonomous control was activated at t=76 [sec] when the vehicle was at around (-140 m, 200 m). The initial gap during the flight

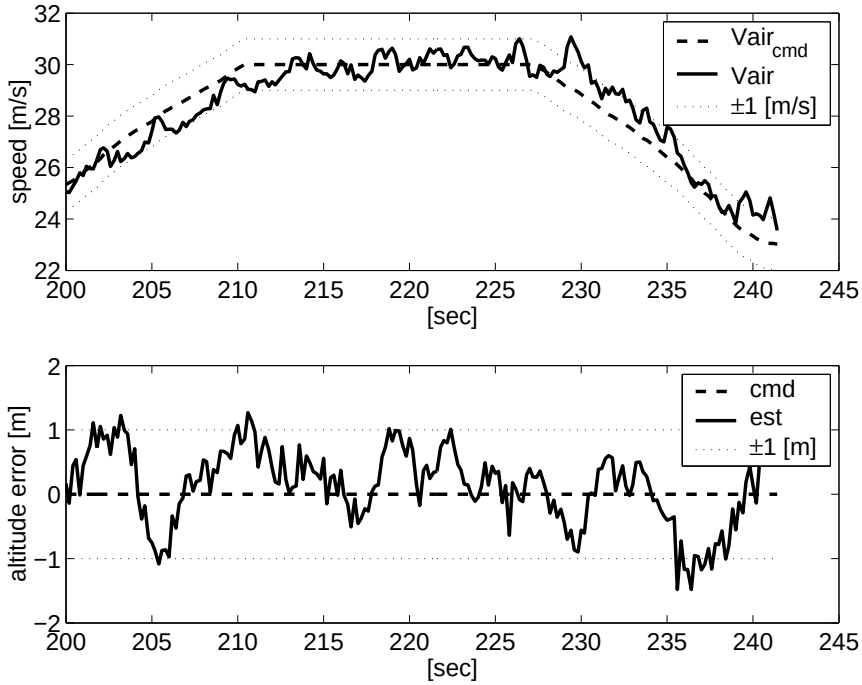

(a) Mini

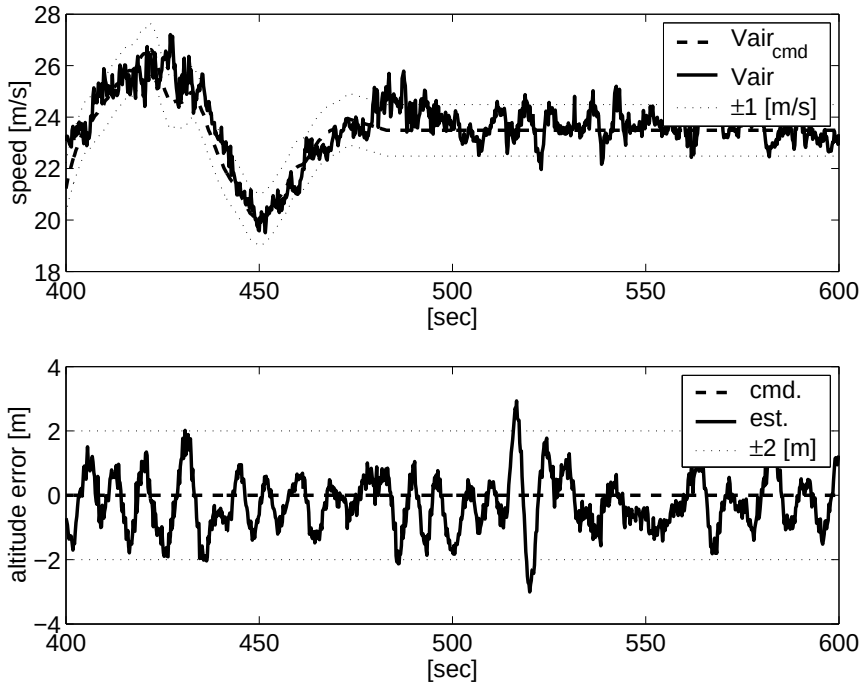

(b) OHS

Figure 6-2: Flight Data for Longitudinal Controller

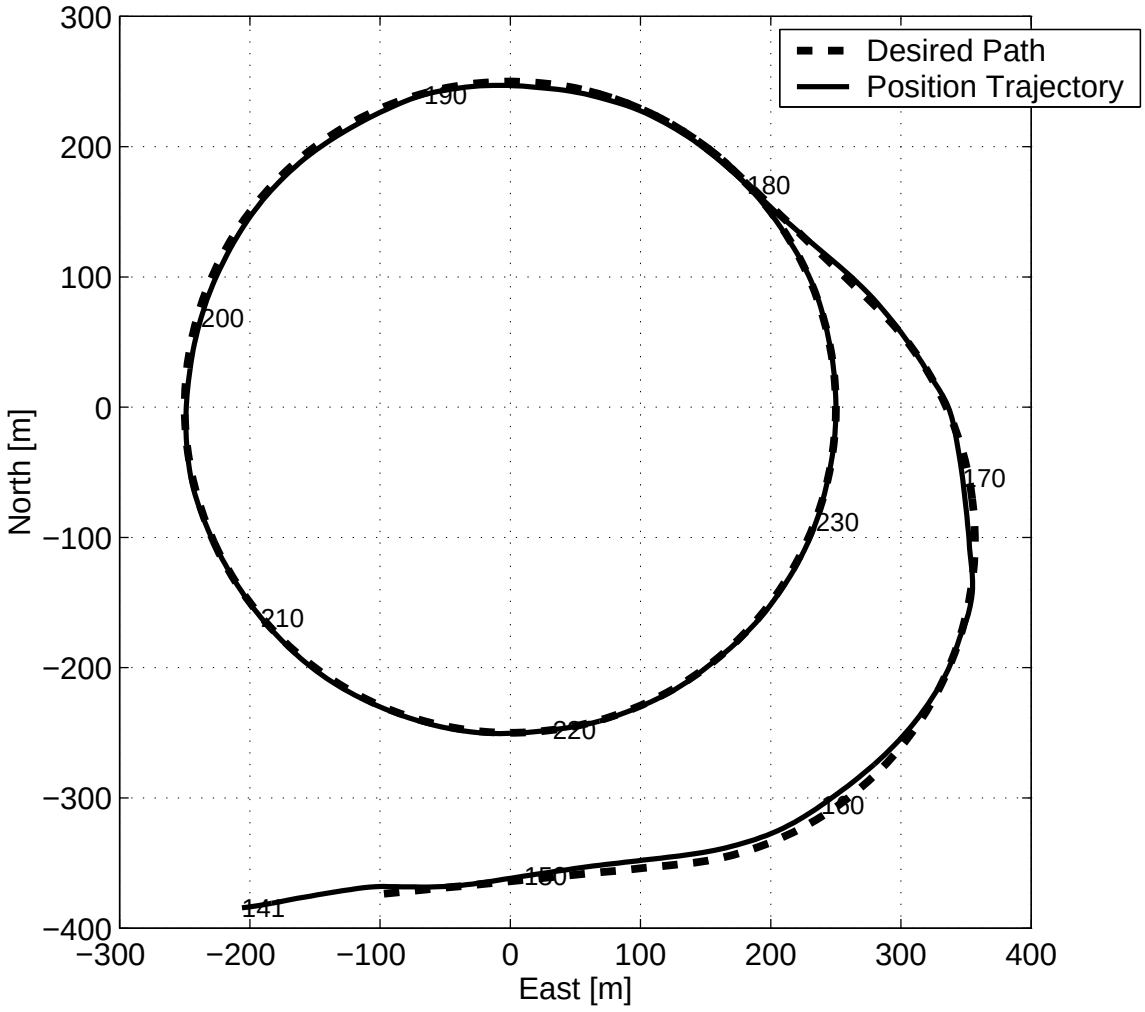

Figure 6-3: Flight Data of MINI - Trajectory Following

time between 76 and 90 seconds between the actual flight path and the commanded path, is due to the offset of the initial velocity vector. After the transition period, the trajectory of the vehicle converged to the commanded path within ±2 meters for the 78% of its flight time and within ±3 meters for the 97% of the flight time.

6.2 Flight Test of Rendezvous Phase I

After validating the control system for each aircraft, the Phase I rendezvous flight tests were performed. As mentioned earlier in Chapter 3, the OHS Parent vehicle follows the circular flight path without having any knowledge of the Mini vehicle during Phase I. The Mini vehicle schedules its flight path and performs formation flight by receiving position

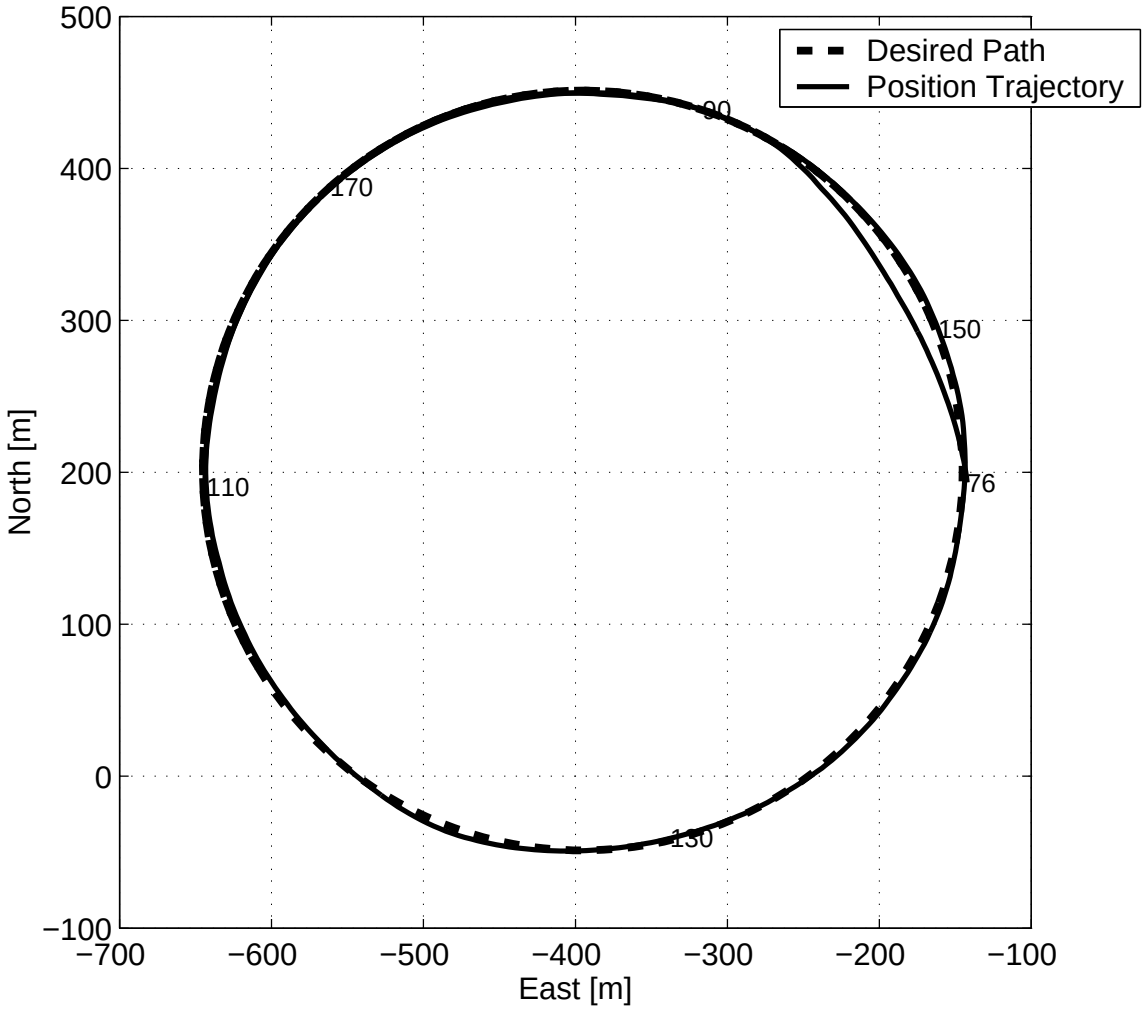

Figure 6-4: Flight Data of OHS Parent - Trajectory Following

information from the OHS Parent.

To the time of this thesis writing a total of 6 out of 7 trials of the Phase I flight tests were successful. There was one case where the procedure had to be aborted due to the malfunction of the communication link. One successful case is report here in greater detail. Another case is reported in Appendix F. The series of plots in Figures 6-5 and 6-6 show the positions of the Parent and the Mini in the north-east 2-D map at every 10 seconds. The letter 'O' on each plot stands for the location of the OHS Parent at each time, and 'M' is for the location of the Mini. The OHS Parent had been flying autonomously and maintaining a circular path when the Mini was switched to autonomous mode. The center of the circle is at (E=0 m, N=0 m). The autonomous control of the Mini vehicle initiates at about 40

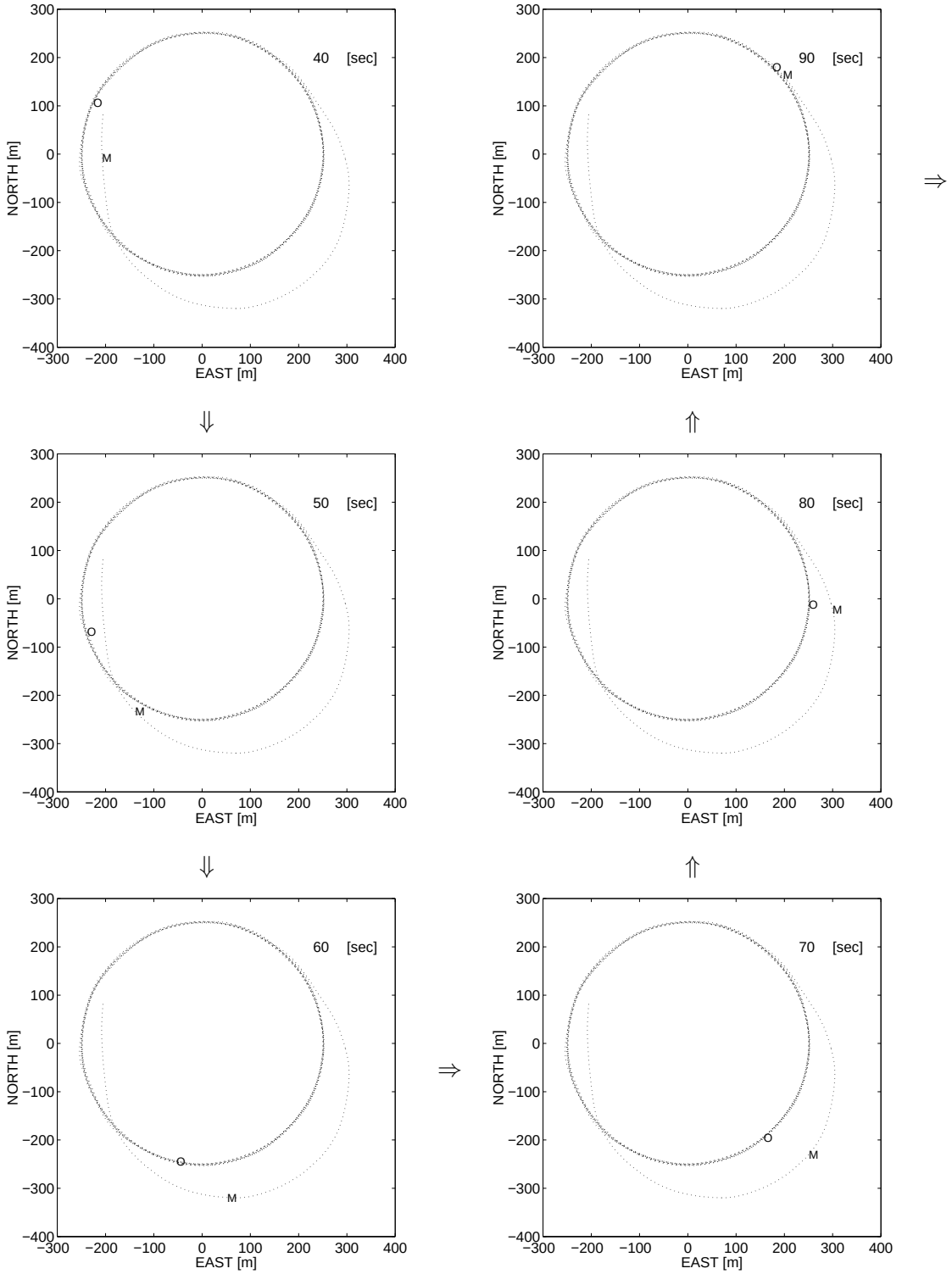

Figure 6-5: Flight Data - Phase I Trajectories of OHS and Mini (O:OHS, M:Mini)

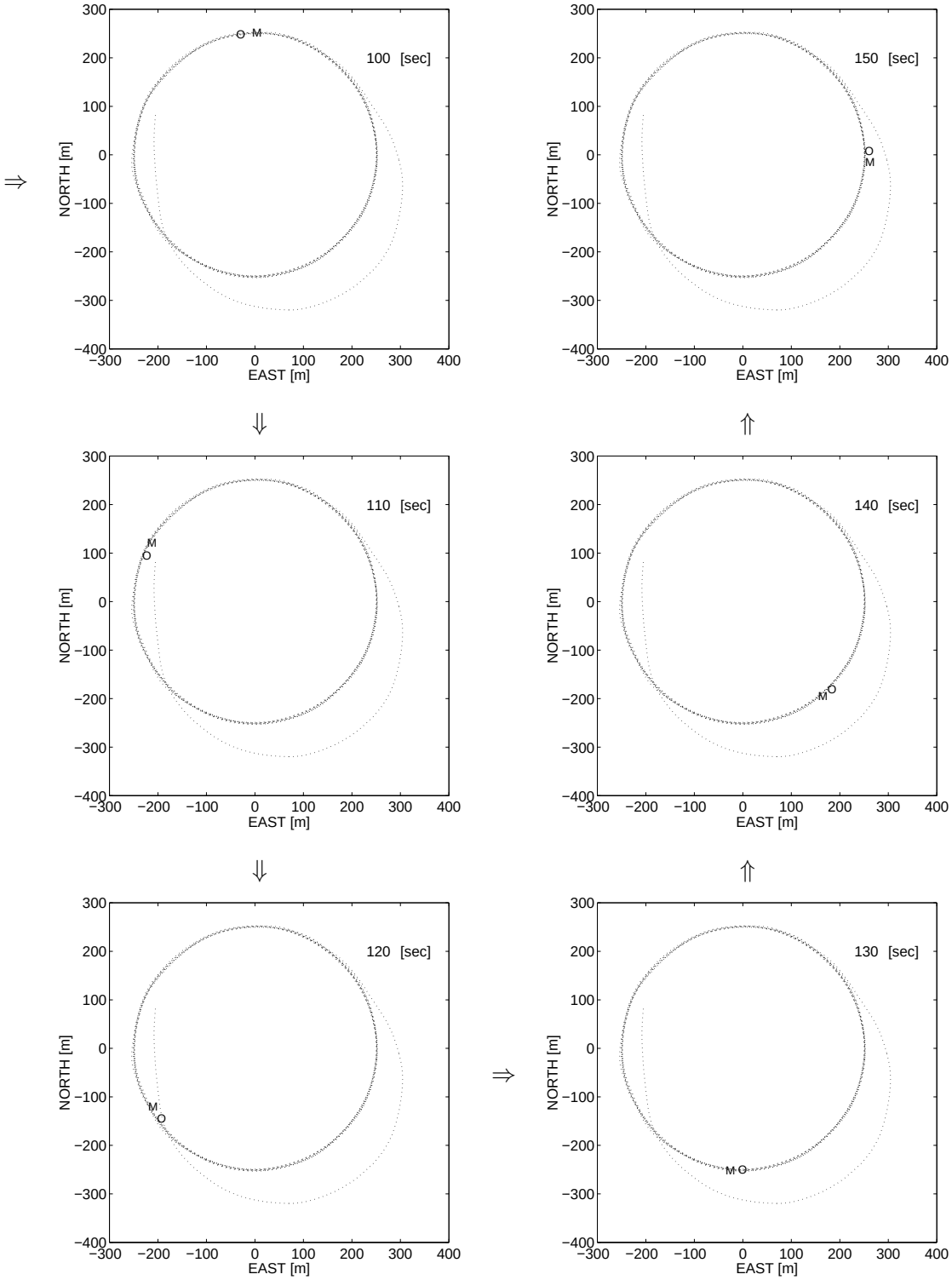

Figure 6-6: Flight Data(cont'd) - Phase I Trajectories of OHS and Mini (O:OHS, M:Mini)

seconds when the Mini was near (E=-207 m, N=-8 m), and the Parent was at (E=-225 m, N=105 m). Both UAVs were heading approximately south. From time=40 [sec] to 92 [sec], the Parent kept flying along the circle and the Mini generated and scheduled its path, and at about 92 [sec] the Mini entered the circle. From 92 [sec] onward the Mini was commanded to track the same circular path while maintaining the separation command relative to the Parent. Although the position plots here are presented until 150 [sec], the Mini and the Parent continued their flights making two and a half circuits of the circular path together before the Mini was switched back to the manual mode at 290 [sec]. Figure 6-7 shows the photo taken from the ground station during this period.

Figure 6-7: Formation Flight during Phase I Flight Test (The Mini is commanded 12 meters behind and 2 meters above the Parent at this moment)

During the period that the two vehicles were flying together the separation distance command was reduced gradually by a ground station command from the initial command of 30 meters down to 12 meters. The first graph in Figure 6-8 shows the relative distance and the separation command. During the period of the entire formation flight from 92 seconds till 290 seconds the separation distance command was slowly reduced, and the Mini

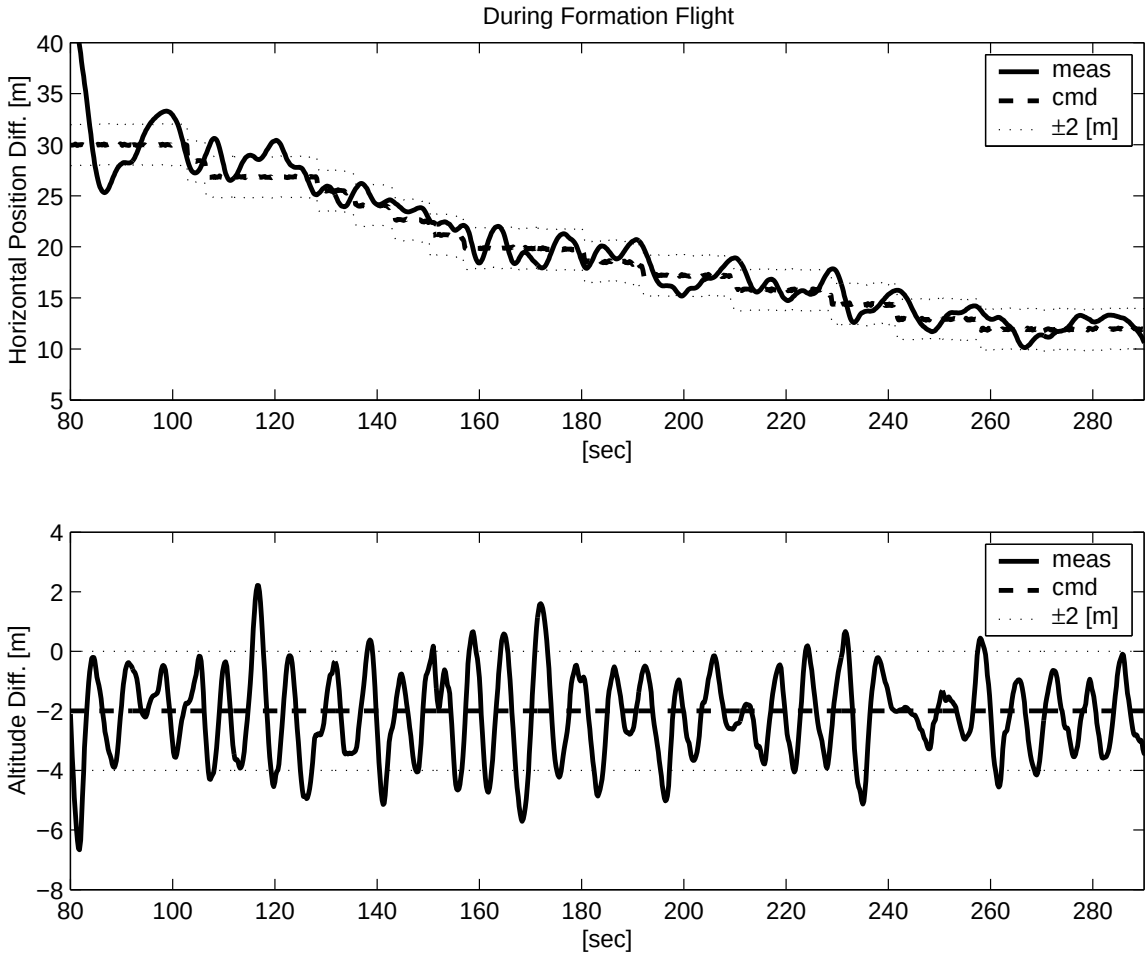

Figure 6-8: Flight Data of Relative Position Differences during Formation Flight in Phase I

vehicle followed its command within the error of ±2 meters for the 86% of this period.

The bottom graph in Figure 6-8 shows the altitude difference between the two vehicles during the formation flight. The command for the altitude difference was set to be 2 meters in this test, with Mini vehicle higher than OHS Parent. The altitude difference remained for the 84% of the time within ±2 meters.

Another video camera was installed at the back portion of the OHS fuselage facing backward in order to see the Mini vehicle approaching and following Parent from this view point. The image was transmitted to the ground station. Figure 6-9 shows a captured image from the rear facing camera.

Figure 6-9: OHS Rear Camera View on MINI during Formation Flight in Phase I

6.3 Summary

This chapter reported the results of the flight tests on the individual aircraft, and then showed the flight data on the Phase I demonstration. The flight data indicates that the requirement of the Phase I rendezvous is satisfied - the controls of the two vehicle's position are accurate enough for the optical sensor to be engaged for the Phase II. The two aircraft performed the Phase I procedure from an arbitrary initial position, and eventually configured the associated formation flight with the separation command of 12 meters while maintaining the relative position error within 2 meters in both horizontal and vertical directions for 85% of the flight time..

Chapter 7

Summary and Recommendations

7.1 Summary

This thesis reported a control system developed for mid-air rendezvous of two small UAVs, and presented the associated flight test results. The engineering approach to this challenge was to divide the rendezvous procedure into two phases. Phase I is to bring the two UAVs to within close proximity of each other, with one trailing the other within 20 meters; from any arbitrary initial positions. A stand-alone GPS was used for each vehicle as the primary position sensor. Phase II is to bring the two vehicles more closely together, to within a few meters of each other, for a potential reintegration or refueling.

The team built two demonstration UAVs and the avionics for each vehicle using inexpensive commercial off-the-shelf components. Six degree-of-freedom rigid body dynamics were used as a base to model the dynamics of each vehicle. In addition, the Parent vehicle required modeling of the effect of the flexible tail section to achieve successful control designs (Section B.7). The aerodynamic forces and moments were estimated mainly by the vortex lattice method.

One of the control challenges in small UAVs is the effect of the wind disturbances because the size of the typical wind speed is not very different from the vehicle nominal speed. The nominal flight speed for the two demonstration UAVs is around 22 m/s, and the controllers on both vehicles were designed to satisfy 1$\sim$2 meters of altitude error and 1 m/s of speed error under the nominal wind speed of 5($\pm$1) m/s.

In bringing the two vehicles close together from arbitrary initial positions, the project team's approach was such that a reasonable flight path commands are first generated for

each vehicle to follow and each vehicle should be guided on the desired trajectory as tightly as possible for rendezvous and formation flight.

A new guidance logic was developed for tightly tracking a given trajectory. This method is relatively simple, so easy to implement. It was explained in Section 3.3 that there is an element in this guidance logic that enables its tight tracking capability in following curved trajectories. Even though a simple circular path was used as an example for a curved line in Section 3.3, the new nonlinear guidance logic can tightly track any arbitrary, complex curved path, as long as the local desired path around the current vehicle position and the reference point is close to a circular arc. It was also shown that the guidance logic has an adaptive capability to the vehicle speed changes due to external disturbances such as wind.

An estimation method was developed, that combines aircraft kinematics, GPS, and low quality rate gyros. It is relatively simple and low-order, so easy to implement. Because this estimation method uses GPS information at lower frequencies for the indication of turning of a flight path, it effectively provides a means to generate non-biased lateral acceleration for the trajectory tracking guidance logic.

Phase II guidance strategy was also developed. An optical sensor was augmented in this phase. The proportional navigation is used as the base of the guidance logic during Phase II. The required acceleration commands generated by the guidance algorithm are executed by the low level controller and by the additional control surfaces such as the vertical fin control surface and the flaperon's flap mode. A linearized model for the Phase II engagement was developed and miss distance analysis was performed.

The guidance and estimation methods were implemented and demonstrated to work in the series of flight tests. Based on these the team demonstrated high accuracy control of small UAVs. In many of the flight tests, the two vehicles were controlled within a position accuracy of 2 meters under the wind condition around 5 m/s which is larger than 20 percent of the nominal vehicle flight speed.

The team successfully demonstrated Phase I flight test several times, where it was shown that the two UAVs can be brought from any arbitrary initial positions to a configuration of formation flight while the two aircraft maintains their relative position within the error boundary of 2 meters for 85% of the autonomous flight times. To the best of author's knowledge this is the tightest control of two small UAVs demonstrated to date.

7.2 Recommendations

- With a single optical sensor in the current setup for Phase II, the relative position information between the two vehicles is not obtained. The single camera option was taken because of the hardware complexity and the limited time available in the project. Thus, the guidance had to be based on line-of-sight control with a relatively small closing speed set between the two vehicles. A more proper way would be to obtain the relative position and then control the vehicle(s) based on this information, especially for the aerial refueling where the two vehicles are required to hold the relative position during the refueling period.

- In the aerial refueling between manned aircraft, the probe-and-drogue refueling system is widely used. Another approach for the last phase of the autonomous docking would be to use a *controllable* drogue, where the drogue is equipped with actuators such as lifting surfaces or compressed air and it adjusts its position based on the position of the trailing aircraft. The advantage of this approach is the use of the relatively smaller inertia drogue which can be very agile.

- Regarding the trajectory following guidance logic in Section 3.3, the ratio of the speed and the distance L_1 affects the performance and stability, as explained in Section 3.3.3. In the implementation, a fixed value was used for the distance L_1. Therefore, in a very windy day, when the wind speed was more 8 m/s, it was found that the increase of the inertial speed in the downwind region caused the system less stable. For this reason, an investigation should be made for the possibility of scheduling the distance L_1 based on the vehicle inertial speed.

Appendix A

Detailed Description of Avionics

A.1 Hardware Architecture

Figure A-1 shows the avionics architecture for the Mini vehicle. In the diagram the main

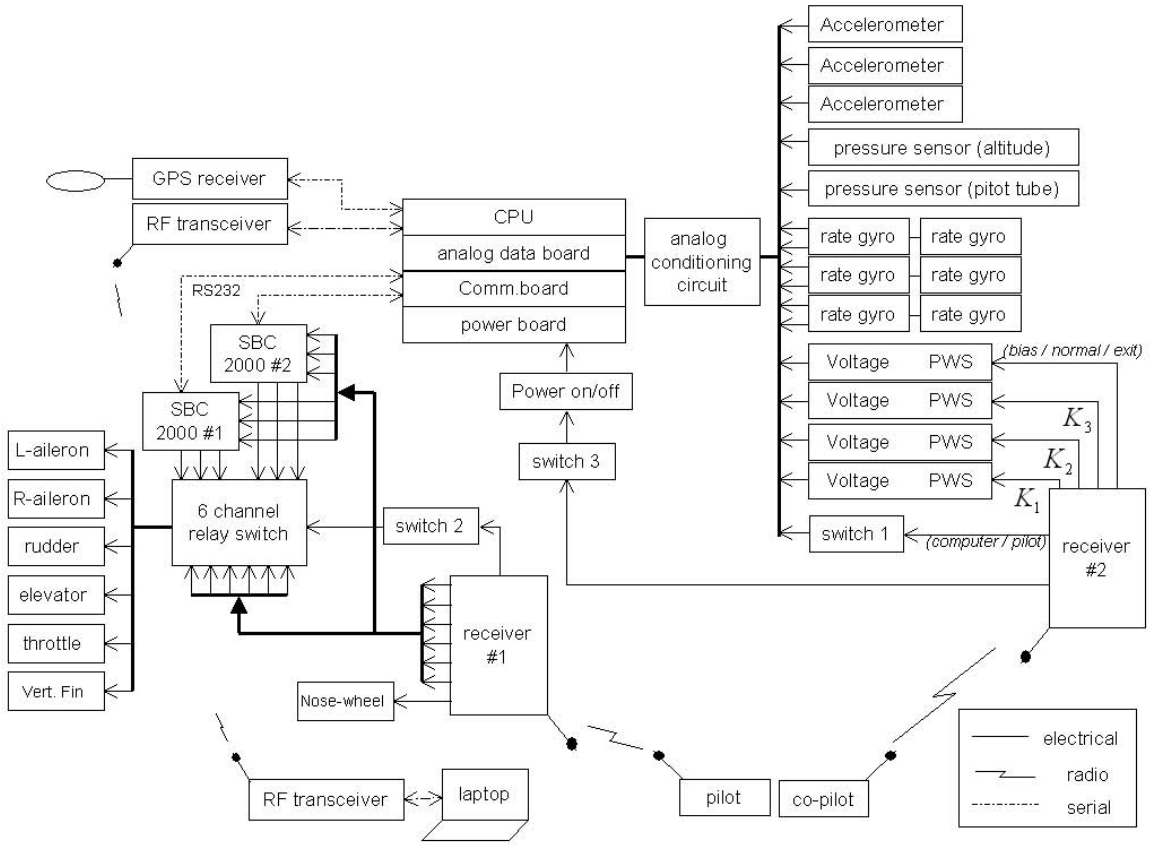

Figure A-1: Mini Avionics Architecture

computer or a central processing unit (CPU), and the associated support electronics, are placed at the center of the figure. On the right a series of the analog devices, including the inertial and the pressure sensors, are connected to the computer through an analog conditioning board. Six gyros are shown in the Mini avionics for redundancy. A GPS receiver and a communication board are connected to the computer through RS232 serial communication link. Shown on the left are the control surface servos and the associated servo control unit including the two microcomputers (SBC 2000) and the 6 channel relay switch. Ground components such as pilot, copilot, and ground station computer are shown at the bottom of the diagram.

The architecture shown here is specifically designed to facilitate flight tests for control system validation. For this type of complex system, a small failure of a critical component can lead to a crash of the aircraft, implying months of delay in the project. Therefore, in order to enhance safety a number of features were added to the avionics architecture.

For example, the need for additional ground personal("copilot") was realized. The copilot can give commands to the onboard avionics while continuously monitoring the behavior of a plane in the sky. Although, as shown in the diagram, there is a communication link between a ground station laptop and the main computer in the test aircraft, this link was not used for that purpose because of the following reasons. First, the person with the laptop is required to constantly look at a display of flight data rather than monitoring airplane in the sky from. Second, this communication link which is basically an off-the-shelf wireless local area network system, turned out not to be as reliable as desired and was sometimes lost during test flights, depending on the orientation and the location of the plane. Thus, this link has been dedicated only to receiving flight data from an airplane, and another RC receiver was added to the aircraft to receive the commands from the copilot. As shown in the diagram, receiver #1 is used for manual control of the aircraft by the pilot, and receiver #2 receives commands from the copilot.

A specific set of procedures is imposed on the pilot and the copilot. First, the copilot can switch the modes between the computer control and the manual control. Second, the copilot can switch the main onboard computer stack on and off. In the actual flight tests, the computer was usually turned off during take-off and climb, and was turned on only after the plane gained sufficient altitude, thus saving onboard battery power. An important lesson learned during early flight testing, including one aircraft crash, was to

physically separate the radio control receivers from the computer stack so as to alleviate control system anomalies caused by electromagnetic pulses during on and off switching of the computer system. At that time remote switching capability was not implemented and the computer had to be turned on before the take-off. Third, using this link the copilot is also able to change control variables during the flight test for the controller validation. Fourth, if an unsafe flight condition arises the copilot is able to terminate the onboard flight system function and return control to the pilot.

Another safety feature implemented in the architecture is the ability to switch to the *safety mode*. This mode is activated by the pilot when it is judged that something is going severely wrong with the onboard automation. There are three modes - normal computer mode, normal pilot mode, and safety mode. When in the normal computer mode or the normal pilot mode, the servo motor control signal - pulse width modulation(PWM) - is generated from the servo motor control microcomputer - SBC2000 in the diagram. But in the safety mode the PWM signal generated by the receiver #1 bypasses the motor control computer and is directly fed to the servo motor. In other words, in the safety mode the pilot can fly the airplane with the ordinary RC configuration. This is done by a multi-channel relay switch, controlled by switch 2, as shown in the diagram.

The usual sequence of mode changes in a flight test is as follows. Takeoff and climb are performed in the normal *pilot mode*, and the vehicle is manually controlled by the pilot. The PWM signal from receiver #1 is read in the servo control microcomputer, SBC2000, which regenerates the PWM signal and sends it to the servo motors.

When the plane has gained enough altitude, the main computer is turned by the copilot through switch 3 and the onboard flight software begins to send information on the status of the avionics and flight data to the laptop ground station. If all indications are positive the normal *computer control mode* is activated by the copilot. This command is read to the main computer from receiver #2 through switch 1 and one of the servo-potentiometer couplings to the analog data board. The the flight software then sends a signal through an RS232 link to SBC2000 #1 and #2 indicating that the computer control mode is initiated. The flight software begins to perform controller functions and generates servo commands. These are sent to the SBC2000 #1 and #2 through RS232 serial links. The SBC2000 microcomputers generate the desired PWM signals and send them to the servo motors (instead of copying the PWM command from the receiver #1, as is done during the normal pilot mode).

Once the flight test using the computer control mode is completed, the pilot takes over the control again on command from the copilot. Then the copilot terminates the onboard flight software, and the flight data is recorded in CPU memory. If there is no need to do another flight test, the computer is switched off by the copilot, and the pilot brings the airplane down on the ground. If another computer control mode test is desired the previous sequence is repeated.

A similar avionics configuration is used for the OHS Parent. Figure A-2 shows the diagram for the avionics architecture of the Parent UAV. It has the same avionics structure

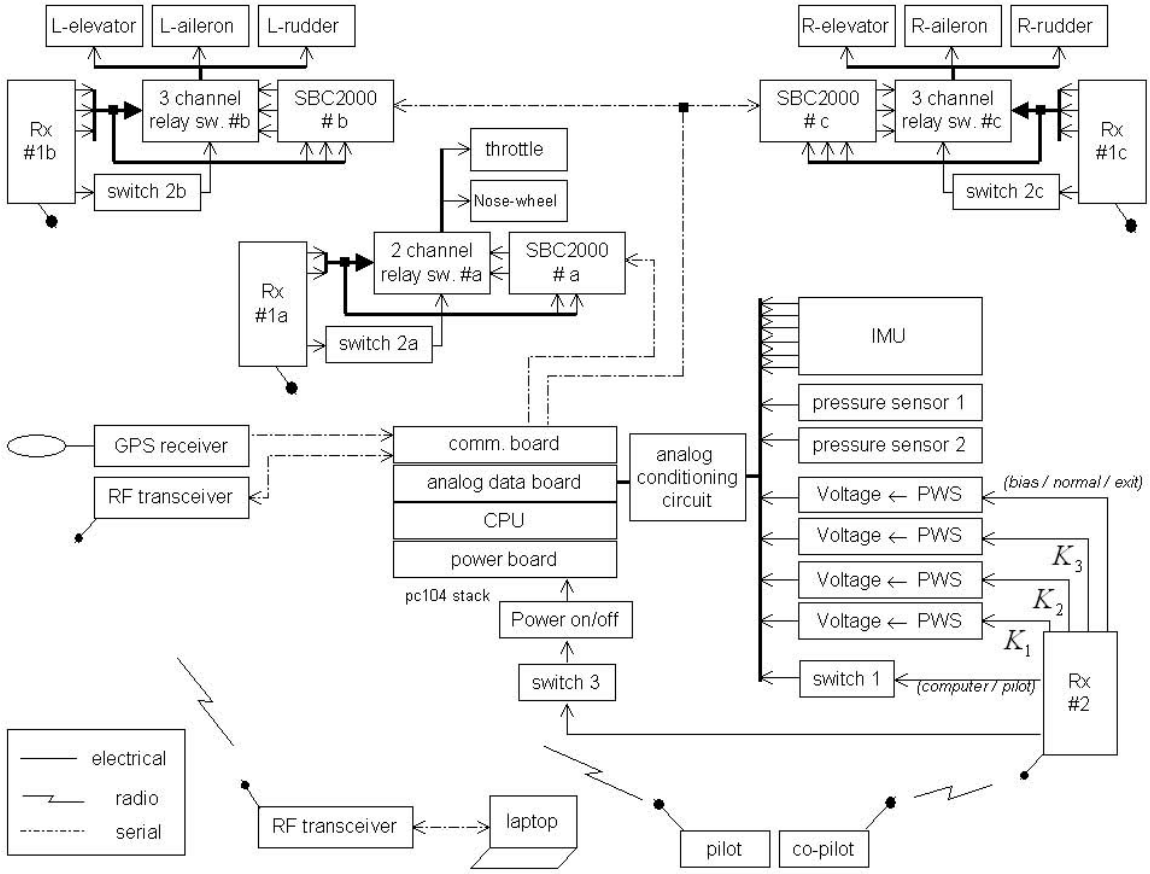

Figure A-2: OHS Avionics Architecture

and the same safety features. The differences come mainly from the larger size of this vehicle. First, three identical servo control units – SBC2000, relay switch, and RC receiver – were made. They are shown in the three bundles at the top portion of the diagram in Figure A-2. One of them is mounted inside the fuselage to control the engine throttle and the nose landing gear. The other two units are placed at the tips of the main wing to

control the aileron, elevator, and rudder on each side. Each of these units uses a separate power source and they are connected only through RS232 serial communication link. This feature improves the noise characteristics of the servo motors by removing the use of a long wiring between the source of the PMW signal and the servo motor. The receivers #1a, #1b, and #1c in the diagram are tuned to the same frequency and they all listen to the pilot transmitter.

The other difference is the use of the inertial measurement unit (IMU) package for the Parent vehicle. Since the Parent UAV can carry heavier payload, the more expensive and accurate inertial sensors are used, compared to the ones in the smaller Mini UAV.

A.2 Overview of Avionics Components and Ground Station

Onboard Computer

The main computer which runs the onboard flight software is the heart of the avionics. It receives the sensor information and generates control commands. It also stores flight data and sends information to the ground. The main computer unit is composed of a few PC104 boards, which include a CPU module, a power board, an analog data board, and a utility module. The PC104 is a standard format for hardware cards. The physical dimensions are around 10x10x2 cm. The cards can be attached on top of each other through the PC104 bus connectors.

CPU Module

The onboard computing is provided by a CPU module from Real Time Devices USA, Inc., CMC6686GX 233 MHz with 64 Mbytes surface mount SDRAM, two serial ports, parallel port, SVGA monitor output support, and PC/AT standard keyboard port. Thus, the CPU module provides a user friendly development environment. It has a DiskOnChip 77Mb (solid state memory). This disk space is a lot less sensitive to vibration than a standard hard-disk and has been used to store flight data. For an operating system and software development, ROM DOS and Borland C++3.1 are used. The chosen CPU module requires the power supply of 5V and 10 Watts.

Power Supply Board

A Tri-M PC104 power board is used. It has a wide input range of 6-40V and provides +5V with 10A, +12V with 2A, -5V with 400mA, and -12V with 500mA.

Analog Data Board

The main function of the analog data board is to interface the analog flight sensors and devices with the CPU board. DM6430HR-8 from Real Time Devices UAS, Inc. is used. Some of the important features of this unit are:

· 16 single-ended or 8 differential analog input channels
· 16-bit,10 microsecond A/D converter with 100 kHz throughput
· ±10 volt input range
· Programmable gains of 1,2,4, & 8
· One 16 bit D/A output channel with ±10 volt range
· +5V operation

Utility Module

CM312 Utility Module from Real Time Devices USA, Inc. provides four additional serial ports and a 10-BaseT network connection. The additional serial ports are necessary because the total of four RS232 serial links is required: two for the two SBC2000s for servo control, one for the GPS receiver, and the other for the RF transceiver. The network connection provided by this module is used to download flight software, to retrieve flights data, and to access the computer in the field with a laptop.

Transceiver

The function of the transceivers is to communicate among the Parent, the Mini, and the ground station. The development of the related software code was performed by Richard Poutrel in the team. The detailed information on the communication subsystem is found in his thesis [38].

The 9XStream 192 modules from MaxStream Inc. are used. It can sustain a continuous data stream at 19.2 kbps. The frequency range is from 902 to 928 MHz. The reception sensitivity is -107 dBm. It has a RS232 serial interface. The required power supply is 5V

with 150mA. It should be noted that the advertised range of 7 miles is highly dependent on the type of antenna used. The unit comes with a 1/4 wave length wire monopole and provides an outdoor range of only 400 m. This antenna was upgraded to a 1/2 wave length antenna A09-HBMM-7-P61 mounted with an MMCX connection. An outdoor range of up to 1 km was verified by a test.

Inertial Sensors

Rate gyros and accelerometers are used at each axis of the two airplanes. A rate gyro directly measures the angular rate about an input axis, and an accelerometer measures the acceleration along an input direction. Many of these units are now manufactured based on MEMS technology. Therefore, the devices usually provides high bandwidth measuring capability for vehicle applications. In general, inertial sensors play an important role in estimating the high frequency information on vehicle states. The estimation method using the inertial sensors is described in Chapter 4.

Mini Inertial Sensors

The main constraint in the selection of the flight sensors for small UAVs comes from their weight and size. There exist a number of high quality off-the-shelf inertial measurement units, such as Crossbow IMU. But these IMUs are still too large and heavy to be installed in the Mini Child vehicle. For this reason a ceramic micro rate gyros are used. Typically, a ceramic rate gyro weighs around 10-50 grams. A tests was performed with a few gyros, and Tokin CD-16D piezo-electric gyro was selected because of its ability to operate in the presence of engine vibration [45, Urbain]. Other important features of the chosen rate gyro are:

· Dimension : 8x20x8 mm
· Range : $\pm$300 degrees per second
· Resolution : 1 degree per second
· Sensitivity : 1.1 mV per degree per second
· Bandwidth : 100 Hz when phase = -90 degree
· Drift : $\sim 5^o$ after 30 seconds of integration
· Power Supply : 5 Volt, 7mA max

In this kind of small rate gyros the drift property is not usually very good. It should be noted that the small value of the sensitivity implies that this device requires a proper signal processing including amplification.

For accelerometers, a Crossbow CXL04M3 3-Axis Accelerometer is used. It is small in size and weight and provides enough range of operation. The properties are summarized as:

· Dimension : 25x25x20 mm
· Range : ±4G
· Sensitivity : 500mV/G
· Bandwidth : DC 100 Hz
· Power Supply : 5 Volt, 24mA typical

OHS Parent Inertial Sensors

Since the larger OHS Parent UAV can be equipped with heavier electronics than Mini vehicle, a Crossbow IMU400CA-100 was chosen for the inertial sensors. Its size is 80x100x80 mm and the weight is 600g. It provides RS-232 digital output as well as analog outputs. It has an update rate of 100Hz and runs with 9∼30 input volt with 250mA max. Some other important features are:

		Angular Rate	Acceleration
· Range	:	±100 deg/sec	±2 G
· Bias	:	$< \pm 1$ deg/sec	$< \pm 8.5$ mG
· Scale Factor Accuracy	:	$< 1\%$	$< 1\%$
· Resolution	:	< 0.025 deg/sec	< 0.25 mG
· Bandwidth	:	> 10 Hz, -3dB	> 75 Hz, -3dB
· Random Walk	:	$< 0.85\ deg/hr^{1/2}$	$< 0.1\ m/s/hr^{1/2}$

Global Positioning System (GPS)

GPS sensor is the main source to obtain the low frequency information on the position and the velocity of an aircraft. Therefore, this sensor plays an important role in the Phase I of the mid-air rendezvous.

The All-Star GPS receiver from Canadian Marconi Company and the AT575-70 GPS

antenna from AeroAntenna Technology Inc. were chosen. The same receiver is now sold by BAE System, Canada. The selected device provides 5 Hz update rate. Table A.1 summarizes the position and the velocity output properties of this GPS receiver. In the

Navigation Accuracies	GPS	DGPS
Horizontal Position	30 m	2 m
Altitude	40 m	5 m
Ground Speed	0.13 m/s	0.05 m/s
Vertical Speed	0.16 m/s	0.1 m/s

Table A.1: Position and Velocity Characteristics of All-Star GPS Receiver. (Note: GPS is for SA inactive, and the performance is for 2 Sigma (95%). This accuracies are for HDOP=1.5, VDOP=2.0, and TDOP=0.8)

table, the absolute position error for the stand-alone GPS seems to be large considering the requirement of the Phase I rendezvous where the two airplanes are supposed to maintain the relative position within 20 meters. But, even if the GPS receivers are used in the stand-alone mode independently by the two airplanes, it turned out that the relative position error is within 3$\sim$4 meters. The reason for this small relative position error comes from the fact that many common error sources are cancelled each other in the two GPS receivers when they are placed relatively close to each other. Thus, the GPS sensors were used in the stand-alone mode independently in the two UAVs for the Phase I air-rendezvous.

The chosen GPS receiver has 0.4 seconds of a time delay. The delay was found by a test setup devised by the team. The associated diagram for the test is shown in Figure A-3. In this setup, while the inverted pendulum swings the GPS output is recorded, and at the same time the rotational potentiometer measurement at the pivot point is also stored. The time delay was discovered by comparing the time history of the two measurements. A more detailed description of the test and the associated results can be found in [38, Poutrel]. The pendulum test setup was also used to check the performance of the estimator that filters the GPS position and velocity measurements. The description of the estimator and the associated test results are presented in Section D.1 .

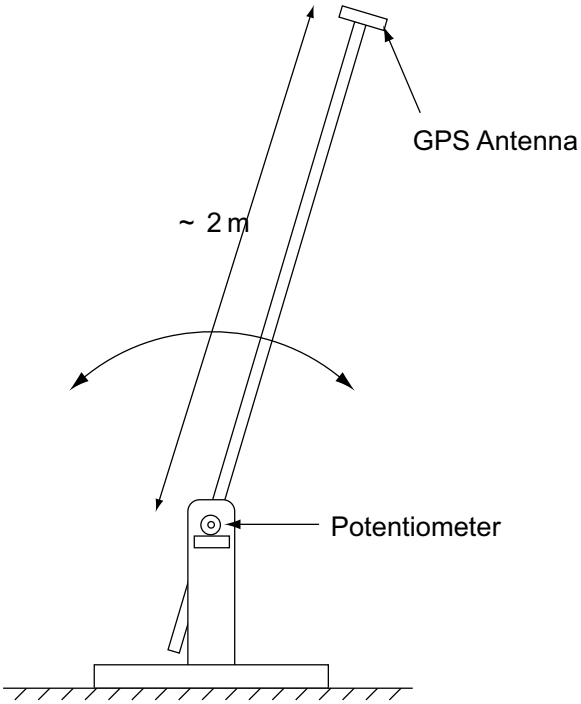

Figure A-3: GPS Pendulum Test Setup

Air Speed Sensor

An air speed sensor is recommended to be installed for a small airplane. The GPS sensor gives the ground speed of the vehicle. But under a windy condition the ground speed can be very different from the air speed. The air speed is the one that matters in determining the aerodynamic forces and moments, and with an air speed sensor a stall situation can be avoided. Especially for the Parent and the Mini UAVs the nominal flight speed of these vehicles is around 22 m/s, and the wind speed on ordinary days can easily be around 5 m/s, which is more than 20% of the flight speed. Therefore, the feedback control on the air speed is desirable for the Parent and the Mini UAVs.

In order to measure the air speed two pitot tubes were built for the Mini and the OHS Parent. Figure A-4 shows the diagram of the pitot tube made in the team. Two metal tubes which have different diameters are used. The total pressure is measured at the pressure of the hole of the inner tube facing toward the airflow. The static pressure is measured by the serval small holes placed on the outer tube at about 30mm from the front. These small holes are punctured all around the outer tube in order to make the measurement less sensitive to

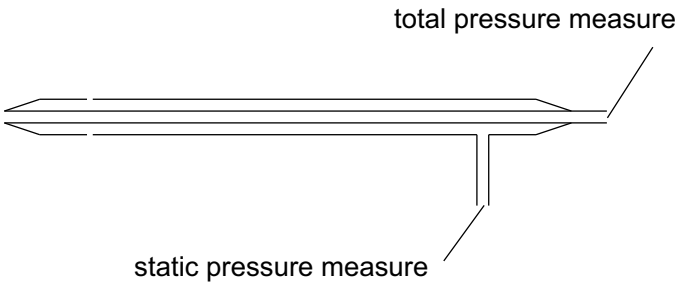

Figure A-4: Pitot Tube Diagram

the attitude change of the vehicle. The associated pressure difference gives the air speed. A differential pressure sensor, PX138-0.3D5V from Omega Company was used. The operation range of the chosen pressure sensor is from 0 to ±0.3 PSI. It requires a supply voltage of 7 to 16 Volt.

A pitot tube should be mounted such that it is well exposed in a free stream without the air flow being disturbed by any other objects around. For this reason the pitot tubes was made long(∼25cm) enough and are mounted under the wing at the front part for the Mini vehicle and on the truss for the OHS Parent.

The constructed air speed sensor units were calibrated in a wind tunnel. The two units resulted in the same calibration curve shown in Figure A-5. With the pitch angle variations of up to ± 5 degrees the differential pressure measurement almost didn't change at all. In Figure A-5, it is noticed that a parabolic relation is obtained between the air speed and the output voltage of the pressure sensor. This agrees to the fact that the dynamic pressure is proportional to the squared term of air speed. The chosen pressure sensor is sensitive enough to have the voltage range of almost 1.0 volt in the flight region between 16 and 30 m/s

Altitude Pressure Sensor

An altitude pressure sensor was used to compensate the time delay of 0.4 seconds in the GPS receiver. Therefore, only the high frequency information was used from the altitude pressure sensor. The same differential pressure sensor PX138-0.3D5V from Omega Company was used, but one of the port was sealed this time. The sensitivity of the pressure sensor is good enough to give the output voltage change of 21.6 mV per the altitude change of 1 meter.

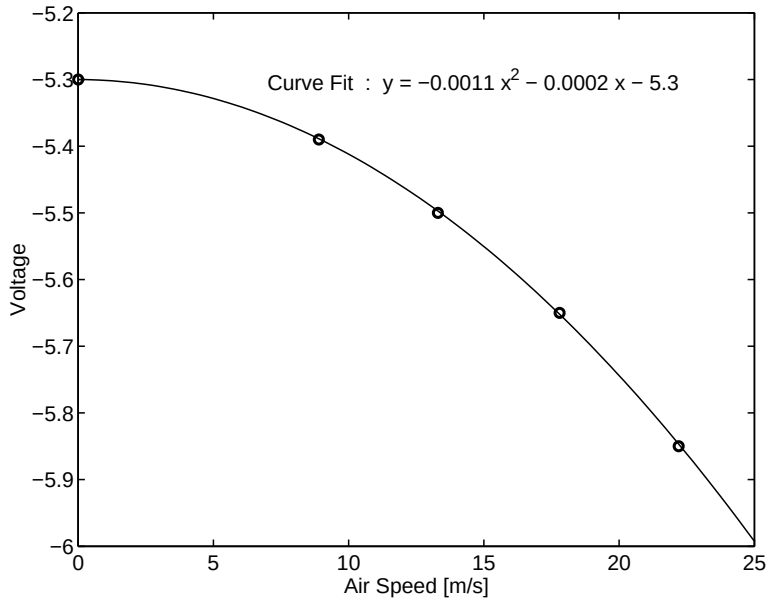

Figure A-5: Calibration of airspeed sensor. (Note : voltage supply 12[V])

Optical Sensor

The use of the optical sensor in the Phase II of air rendezvous is depicted conceptually in Figure A-6. A rear-facing diode array which generates 4 kHz infra-red pulses is mounted on the Parent vehicle. An electronic unit which measures the two angles(η_h and η_s in the figure) to the diode array on the Parent is placed on the front of the Mini vehicle. The central part of this electronic unit is a Two-Axis Position Sensing Photodiode PSS-DL-16-7 Cer Pacific Silicon Sensor Inc. This photodiode is most sensitive in the infrared frequency region. A few electronic components were added around the photodiode such that the entire unit is only responsive to the 4 kHz infra-red pulses. This unit was built by Thomas Jones in the team. Chapter 5 discusses how the optical sensor unit is used for the Phase II of the air rendezvous.

Analog Conditioning Board

The analog conditioning board mainly performs the high frequency noise rejection on the analog signals from flight sensors. Active low-pass filters were implemented using low-noise LM837 OP-AMP's.

A continuous model is usually used in the control design phase. In order for the controller

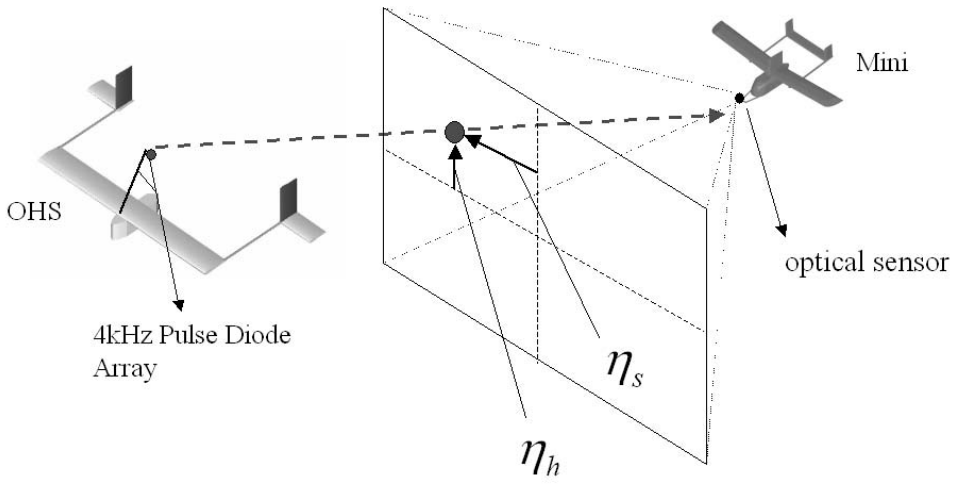

Figure A-6: Optical Sensor Concept : The angles to the target η_h and η_s are measured

to work properly under the associated digital implementation, the rule of thumb is that the sampling frequency should be larger than the frequency range of the vehicle dynamics by about 20 times. So, the sampling frequency for the flight sensors was chosen at 40 Hz. For the anti-aliasing the low-pass filters are implemented in the analog conditioning board. The associated cut-off frequency was chosen at 8 Hz, which is still 4 times faster than the airplane dynamics. Figure A-7 shows the related circuit diagram implemented for the anti-aliasing.

For the Tokin gyro in the Mini vehicle the signal needs to be amplified by a factor of 10 because the output voltage sensitivity (1.1 mV/deg/sec) is small. Figure A-8 shows the associated circuit diagram around the Tokin gyro.

Servo Control Microcomputer

The function of the servo control computer is to generate a pulse width modulation (PWM) signal to be sent to a servo motor. A PWM signal for an RC servo motor typically has a period of 20 ms and a pulse width between 0.7 and 1.5 ms. The servo deflection angle is determined depending on the pulse width. In the computer control mode, the servo control computer receives the command for the control surface deflection from the main computer through RS232 serial link. In the pilot control mode, the servo control computer receives the PWM signal from a RC receiver and regenerated regenerate the PWM signal to send to a servo motor.

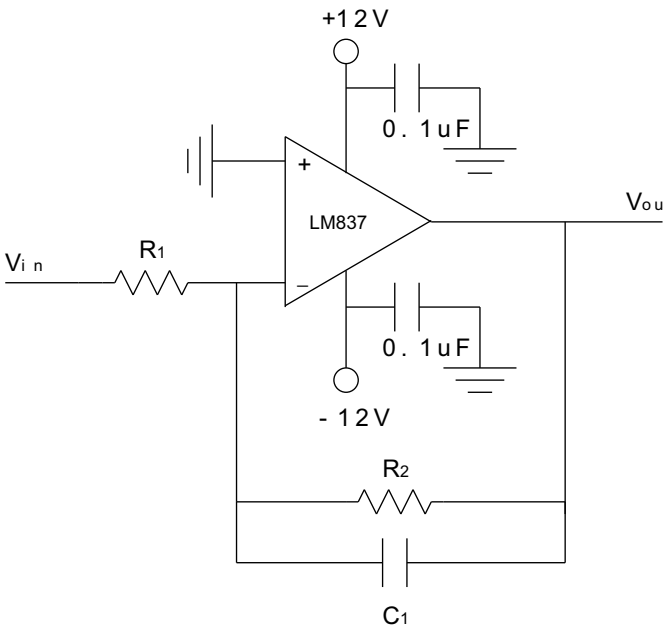

Figure A-7: Circuit for Anti-Ailasing Low Pass Filter. Note: $\frac{V_{out}}{V_{in}} = -\frac{R_2/R_1}{R_2C_1s+1}$. R_1=R_2=20k, C_1=1μF are used.

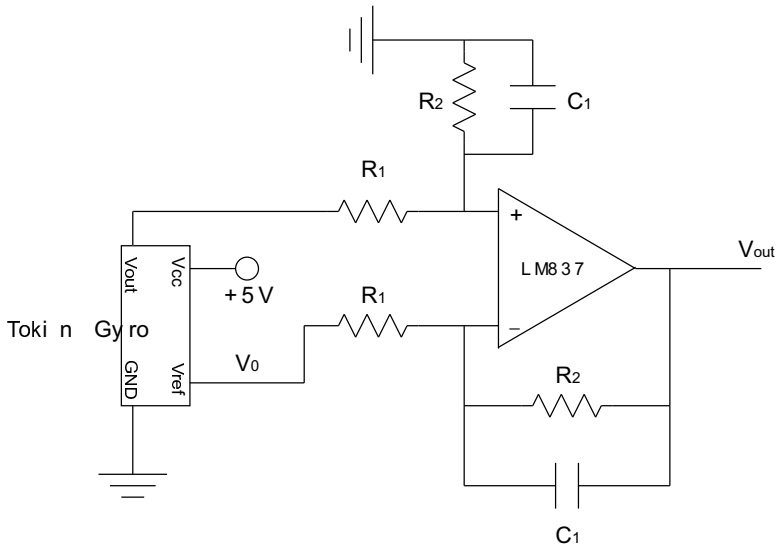

Figure A-8: Circuit around Ceramic Tokin Gyro. Note: $\frac{V_{out}}{V_1-V_0} = \frac{R_2/R_1}{R_2C_1s+1}$. R_1=20k, R_2=200k, C_1=0.1μF are used.

A small micro computer, SBC2000 from Micro Pilot Company is used as the servo control computer. It turned out that the use of up to three channels per each unit is

reasonable to comply with the 40 Hz sampling rate. Each unit is programmed by the Vesta Basic language with an Integrated Development Environment. The associated code was developed by Francois Urbain in the team. Later, a capability of the smooth transition at the switch over from the computer control to the pilot control mode was added by Damien Jourdan. This function achieves a safe mode changes when the vehicle control is taken back to the pilot. This functionality is desirable since the control surface deflection associated with the pilot stick position can be very different from that of the last control command from the computer in the computer control mode.

Servo Motors

Three kinds of RC servo motors were mainly used. They are summarized in Table A.2. These servo motors were used at different locations depending on the size of the load.

RC servo	Speed[sec/60deg]	Torque[kg-cm]
Hitec HS-85MG+	0.13 w/6.0V	3.5 w/6.0V
	0.16 w/4.8V	3.0 w/4.8V
Futaba S9402	0.10 w/6.0V	8.0 w/6.0V
	0.13 w/4.8V	6.4 w/4.8V
Futaba S9303	0.19 w/6.0V	7.2 w/6.0V
	0.24 w/4.8V	5.7 w/4.8V

Table A.2: RC Servo Motors

Usually a strong servo motor is recommended for the elevator deflection. Hitec HS-85MG+ Metal Gear is used for all the servos in the Mini vehicle. They are also used for the throttle, the rudders, and the noise-wheel servos in OHS Parent. A pair of Futaba S9402 servos is allocated for the elevators, and a pair of Futaba S9303 is used for the ailerons in the OHS Parent vehicle.

The exerted torque on a servo motor can be roughly estimated by the following. From Figure A-9, the moment balance at the joint of the control surface is

$$Fl_1 = L\frac{c}{4}$$

where

$$F = \frac{\tau}{l_2}, \quad L = \frac{1}{2}\rho V^2 S C_{L_\delta}\delta$$

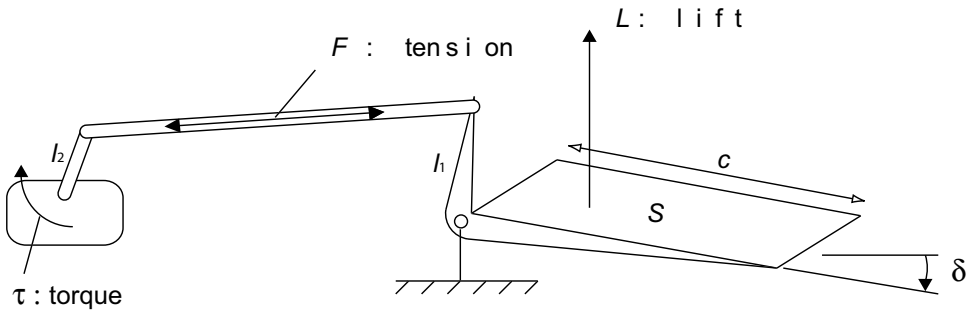

Figure A-9: Servo and Control Surface Linkage

Assuming $C_{L_\delta} \approx 2\pi$ leads to

$$\frac{l_1}{l_2}\tau = \frac{1}{2}\rho V^2 S 2\pi\delta\frac{c}{4}$$

RC receiver and transmitter

Futaba FP-R14148DP receivers were used. This 8 channel receiver was selected because of its robustness to noise. A range test with several receivers from different manufacturers revealed that the chosen Futaba receiver is most robust in the presence of electric and magnetic noise generated from the main computer. Futaba 8UAFS 8 channel radio control system is used for pilot and copilot RC transmitters.

Other Components

Relay switches were used in many places in the avionics. Some of them are the kind that is activated by PWM signals. The relay switches played an important role for the safety-related functions. They were used in switching between the safety mode and normal modes. They were also used to remotely turn on the onboard computer while the plane is in the air. The advantage of the relay switches is the reliability that comes from the use of simple analog/mechanical relays instead of relying on logic of any integrated circuits.

In order to indicate the status of the flight software an LED was used. Using different frequencies such as 2 or 1 or 0.5 Hz ..., it was programmed such that the LED can indicate one of the following modes: insufficient number of GPS satellites(<5), pilot control mode, computer control mode, and phase II mode. The use of an LED in this regard turned out to be very useful. It indicates the status of the flight software without having to plug a display monitor.

Assembly of the Avionics Components

The effect of the engine vibration should be considered in the installation of the inertial sensors. Two methods were used to reduce the vibration level. First, for the Mini vehicle, each gyro and the 3-axis accelerometer were wrapped with a piece of foam sheet and were inserted in a square box together to form an inertial package. Second, this inertial package of the Mini vehicle and the IMU of the OHS Parent were mounted in each avionics box in such a way that the inertial package is suspended by an elastic material. This suspension can be seen in Figure 2-4 (a) and (c) for the Mini avionics box, where a square object in the pictures is the inertial sensor package and is suspended inside the outer square frame. This mechanical method acts as a low pass filter with a cutoff frequency at $\sim$20 Hz, which is about midway in a log-scale between the two frequency ranges of the engine vibration($>$ 100 Hz) and the airplane dynamics($<$ 2Hz).

The mounting location of a GPS antenna on an airplane needs to be carefully selected. If it is mounted too rear, a non-minimum phase zero dynamics is introduced, which makes a tight altitude control difficult. It was also found that the GPS antenna is not very robust to the electro-magnetic(EM) noise from the main computer. When it was placed close to the main computer, it was observed that the number of satellites that can be tracked by the GPS receiver reduced. For these reasons, the GPS antenna was mounted at the top of the truss for the OHS Parent vehicle, and for the Mini vehicle it was placed at the top of the vertical fin.

The RC receiver antenna is almost a meter long when it is stretched. For each vehicle at least two RC antennas should be installed for the pilot and the copilot receivers. These antennas should be installed properly. First, the antennas should not be folded. They have to be straightened in order to a good range. Second, if the two antennas are aligned together one next to the other, the range is reduced for both receivers. Thirdly, they are also susceptible to the EM noise from the main computer. For these reasons, the two antennas were placed along the two tail booms for the Mini vehicle, and for the OHS Parent, one was placed such that it runs in the rear portion of the fuselage and the other was located such that it runs vertically along the truss.

The communication transceiver antenna was mounted vertically inside the vehicle fuselage. With this vertical orientation of the antenna with respect to the vehicle, the zero gain

situation happens only when the airplane is closest and is right above the ground station assuming the pitch and roll angles of the plane are not severe.

Power Subsystem

Table A.3 shows the power budget for the major power consuming electric elements. Considering

Component	Voltage [V]	Power [W]
CPU module	5	10
Data board	5	2.5
Utility board	5	1.0
Transceiver	5	0.75
IMU	12	3
GPS receiver	5	1.5
Total		18.75

Table A.3: Power Budget for Avionics (The power consumptions are under typical conditions)

the efficiencies and the margins in the use of batteries, two NiCd 6V-2800mAH batteries (flat JRPB4550) were used to supply the power to the main electric elements. About 30 minutes of running time was safely guaranteed. For the Mini vehicle, these batteries were placed in the nose cone section in order to place the center of gravity at a reasonable location.

Two other 4.8V-600mAH batteries were used in the Mini vehicle. One supplies the power for the servo motors, and the other for the receivers and the servo control computers. For the Parent vehicle a total of three additional batteries were used for the servo motors. Two 6.0V-1100mAH batteries were dedicated for the control of the elevator, the rudder, and the aileron on each side. A 4.8V-600mAH battery was used for the engine throttle and the nose wheel. Also three other 4.8V-600mAH batteries were used for the receivers and the servo control computers.

Ground Station

The ground station computer displays in real time the flight sensor data and the status of the flight software during flight tests. Figure A-10 shows the snapshot photo of the ground station laptop display. Some of the important flight data displayed in the ground station

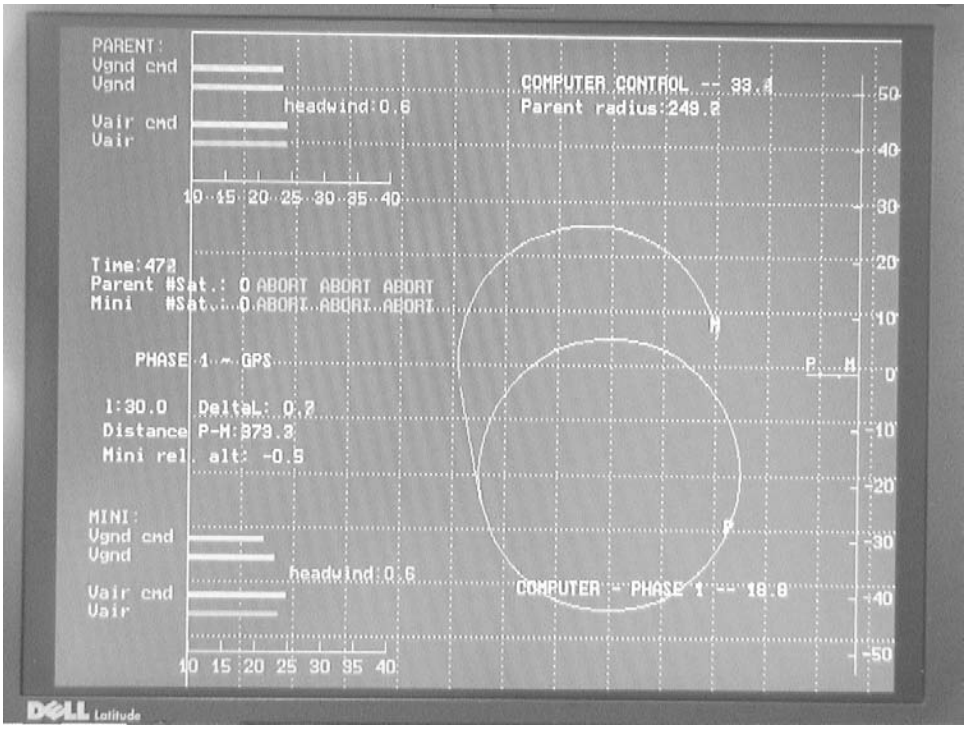

Figure A-10: Ground Station Display

include:

- flight software mode
- commanded flight path line and vehicle north-east position estimate
- altitude command and estimate
- speed command and estimate
- number of GPS satellites seen by the GPS receiver.

The display of the flight software mode reassures the changes of the control mode which is engaged by the copilot. The display of both the command and the estimate for the flight trajectory, the altitude, and the speed makes it possible for a ground personnel to

see whether or not the controller is working properly. When the airspeed becomes lower than a certain criterion set slightly higher than the stall speed, a warning sign flashes. The number of GPS satellites tracked by the GPS receiver is displayed, and if it is lower than 6, a warning sign appears.

It is important to display the various kinds of information in such a way that they can be understood clearly and quickly by an operator. The trajectory of the plane is displayed in a 2-dimensional north-east map. The altitude and the speed are shown with a vertical and a horizontal bar graphes respectively.

A.3 Software

Software Structure

This section briefly outlines the sequence of the flight software implemented on the onboard computers for the two UAVs. When the computer is turned on, a RAM-disk is allotted for the storage space of the flight data. The flight software starts next and performs a series of initializations. One of the important task in the initialization steps is the declaration of a software timer interrupt. Then the flight software follows the sequence outlined in Figure A-11. The program enters the main loop in which the flight software waits for the GPS data update that occurs at 5 Hz. If the GPS data is updated, a few functions are executed such as flight path generation, transceiver and copilot inputs handling, data storage, etc. On the other hand, after the definition of the timer interrupt, at every 0.025 seconds (40Hz) the timer interrupt defined in the initialization step begins to occur and a few time-critical tasks are performed. These include the reading the analog flight sensors, the performing the estimation and the controller algorithms, and the sending the control inputs to the servo motors. The program is terminated by the copilot input which is picked in the main loop of the software, and the flight data is copied from the RAM-disk to the DiskOnChip of the CPU module.

Discretization of Continuous Controller

All the continuous filters designed for the controllers and the estimators should be discretized for the implementation of digital computers. These filters were converted using a zero order

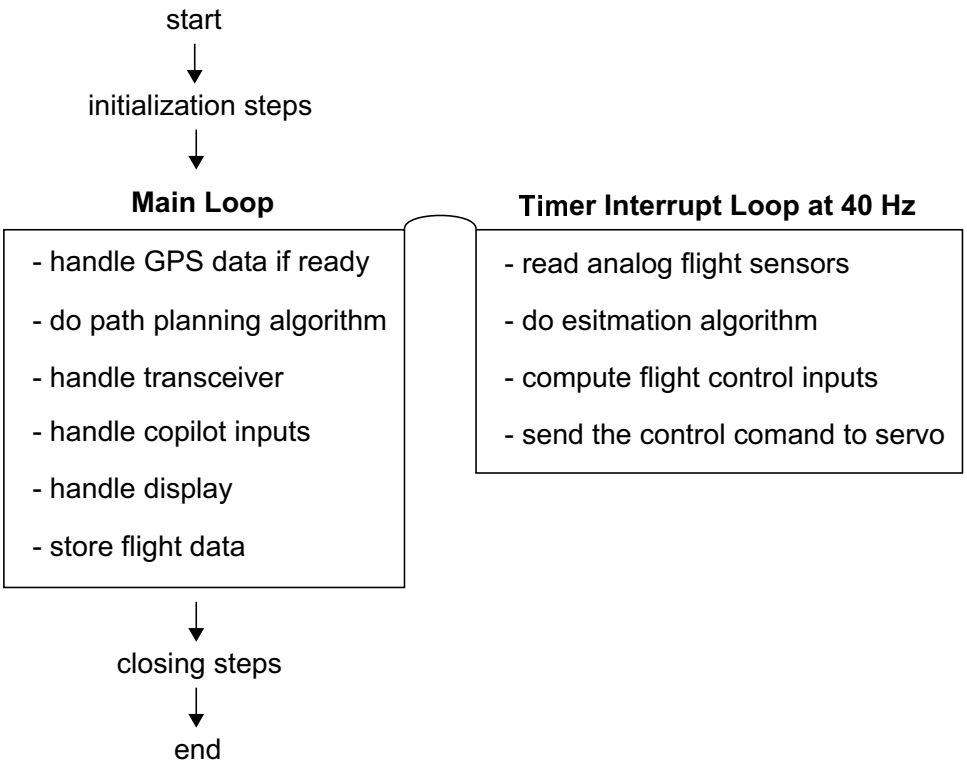

Figure A-11: Fight Software Sequence

hold (step invariance) method [3, Astrom & Wittenmark],

$$G_D(z) = \mathcal{Z}\left[\frac{1-e^{Ts}}{s}G(s)\right]$$

where $\mathcal{Z}$ is z-transformation, $G(s)$ is the continuous transfer function for a controller or an estimator that needs to be discretized, and $G_D(s)$ is the discrete transfer function. T=0.025[sec] is used as a sampling interval. In Matlab the conversion is obtained by the function 'c2dm'.

A couple of Matlab M-files was created that automatically generates a C-code portion from a continuous filter at least for the first and the second order linear transfer functions. Since most of the linear filters designed for the controllers and the estimators were either the first or the second order transfer functions, and there were many cases where the parameters of the filters needed to be changed through the iteration of the design process, the developed M-files that transforms a continuous filter to the corresponding C-code turned out to be very convenient.

A.4 Avionics Diagrams for OHS Parent Vehicle

The overall avionics architecture was presented in Section A.1, and Figure A-2 showed the hardware overview for the OHS Parent UAV. The subsets of the Parent's avionics are presented here as an example.

Figure A-12 and Figure A-13 show the avionics diagram for the control of left side and right side control surfaces (elevator, rudder, and aileron). They are mounted at each side of the main wing tips. Figure A-14 shows the avionics components that are mounted in the fuselage for the control of throttle and nose wheel. Figure A-15 shows the diagram related with the remote power switching capability when the main onboard computer is turned on/off remotely in the air. Finally, Figure A-16 shows the circuit diagram of the analog conditioning board, the interface between the main computer data board and analog sensors.

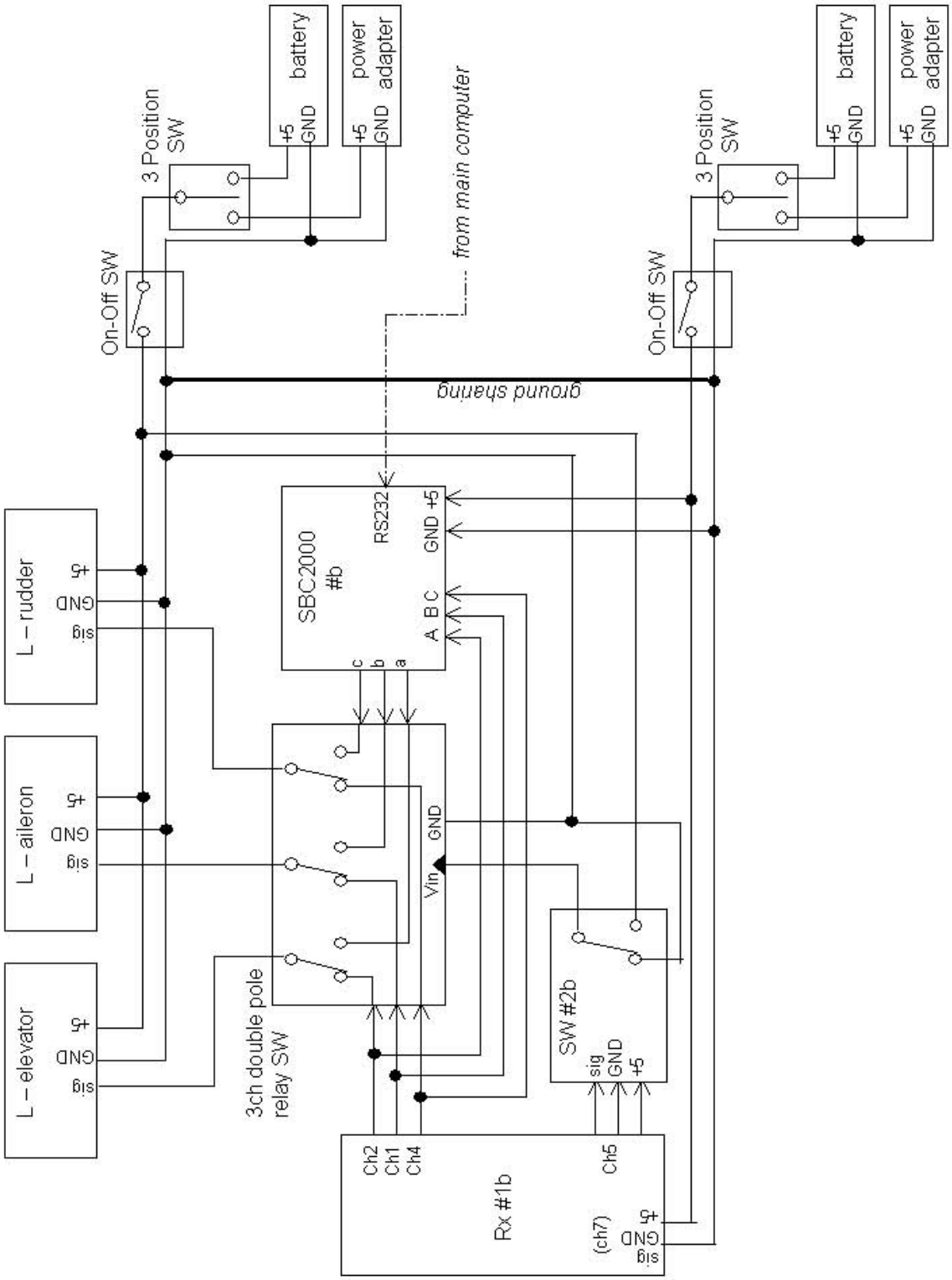

Figure A-12: Avionics for Left Side Controls

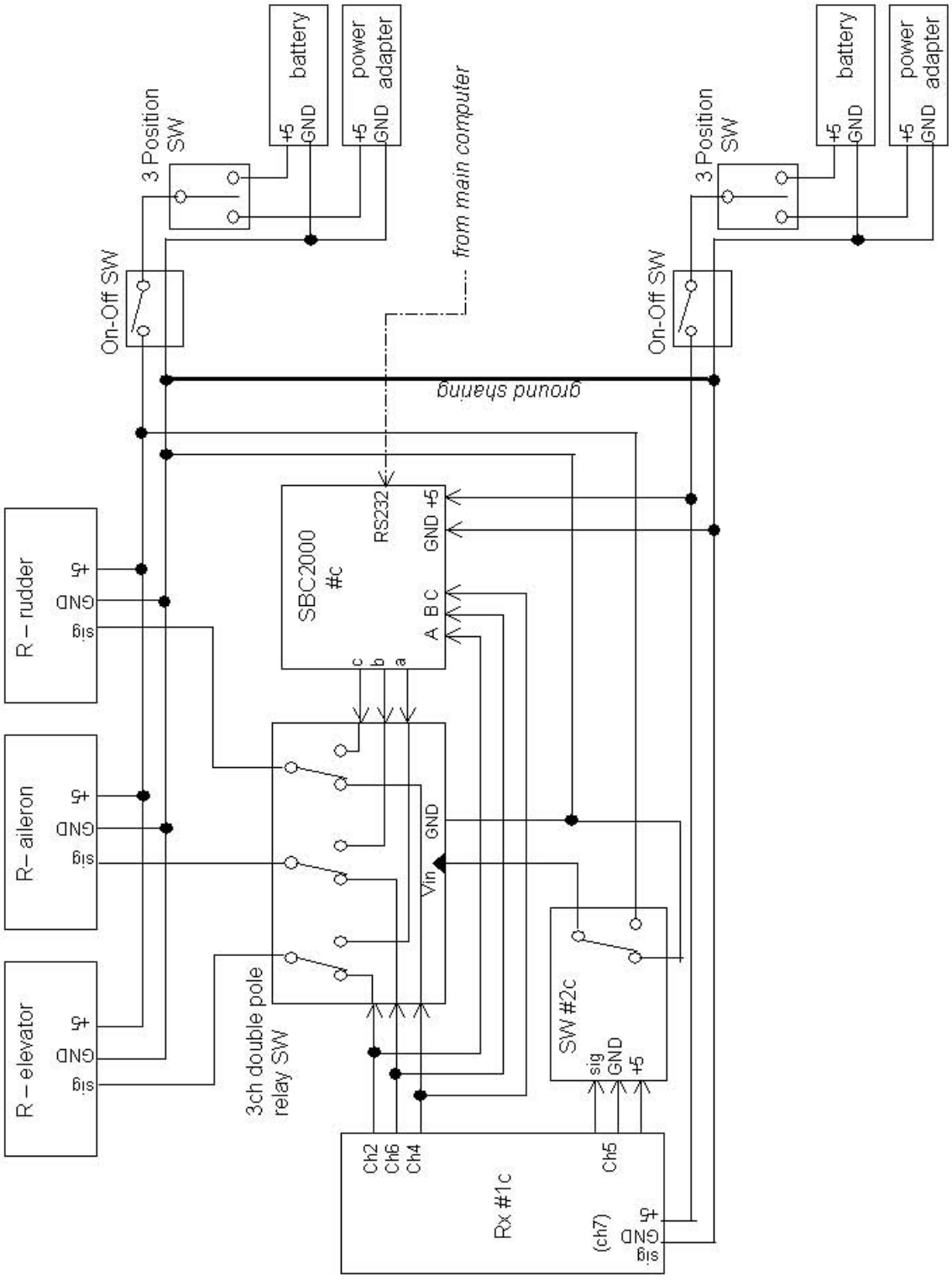

Figure A-13: Avionics for Right Side Controls

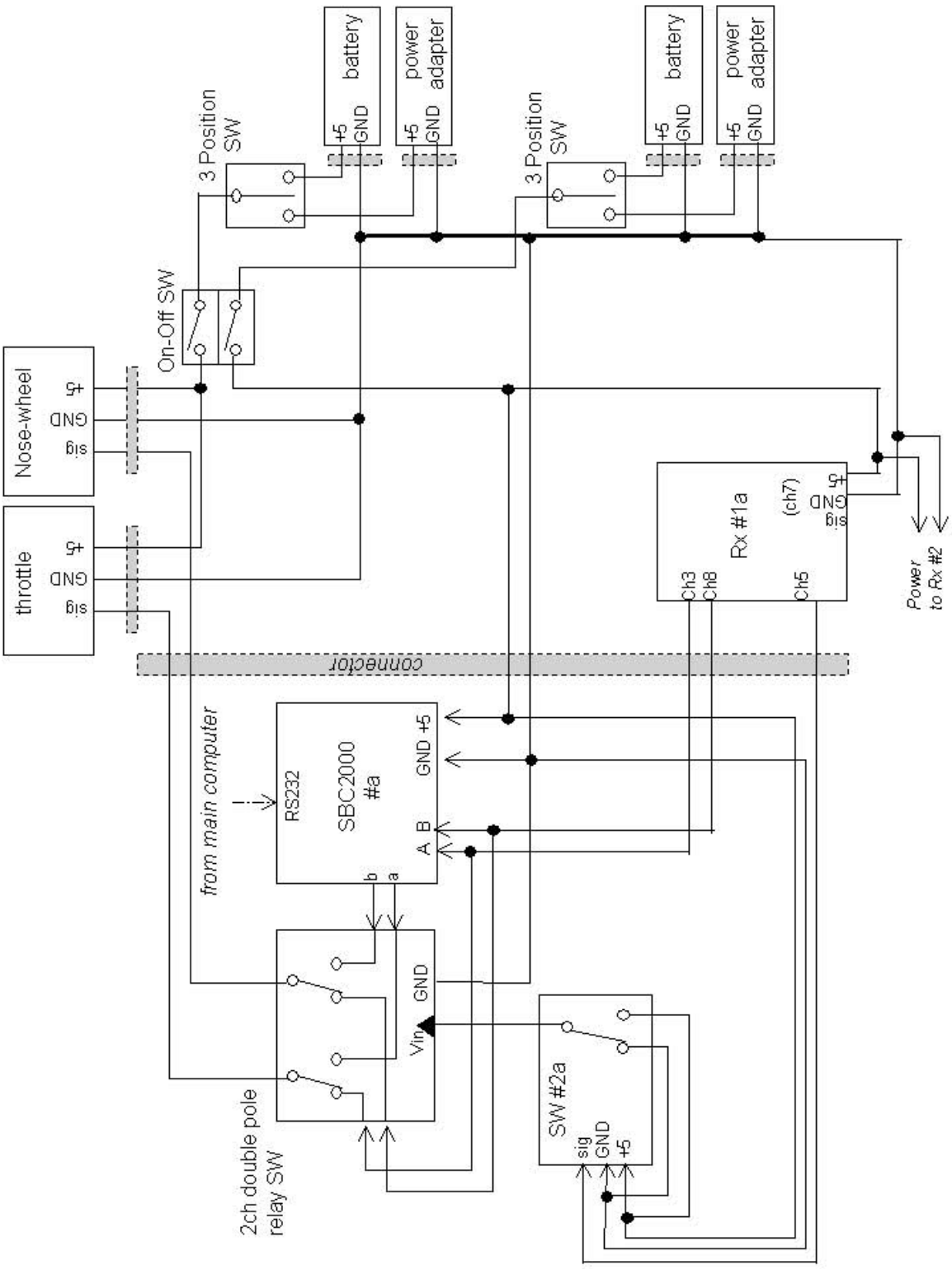

Figure A-14: Avionics for Throttle and Nose Wheel Control

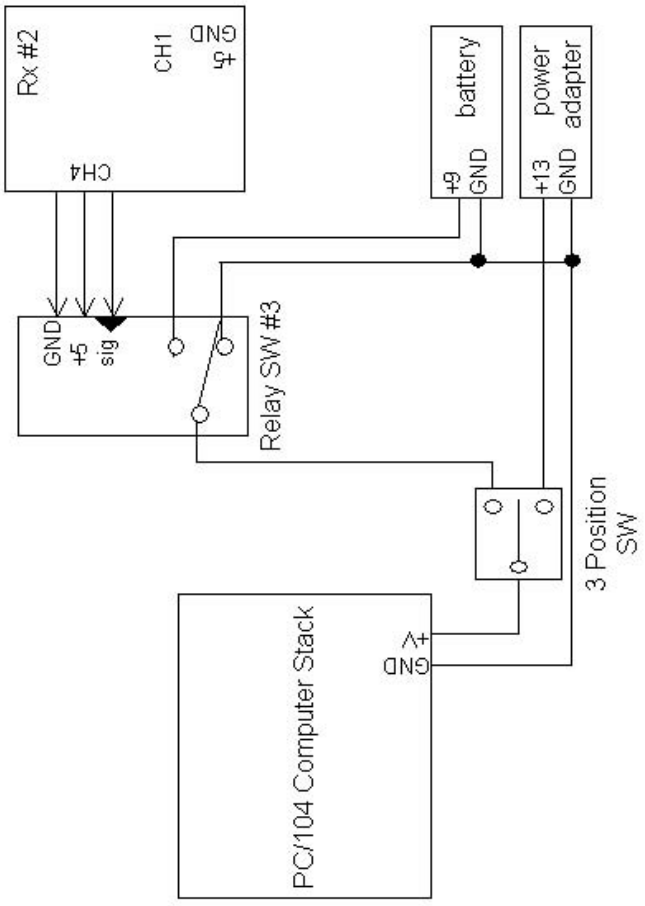

Figure A-15: Power Supply Subsystem for PC104 Computer Stack

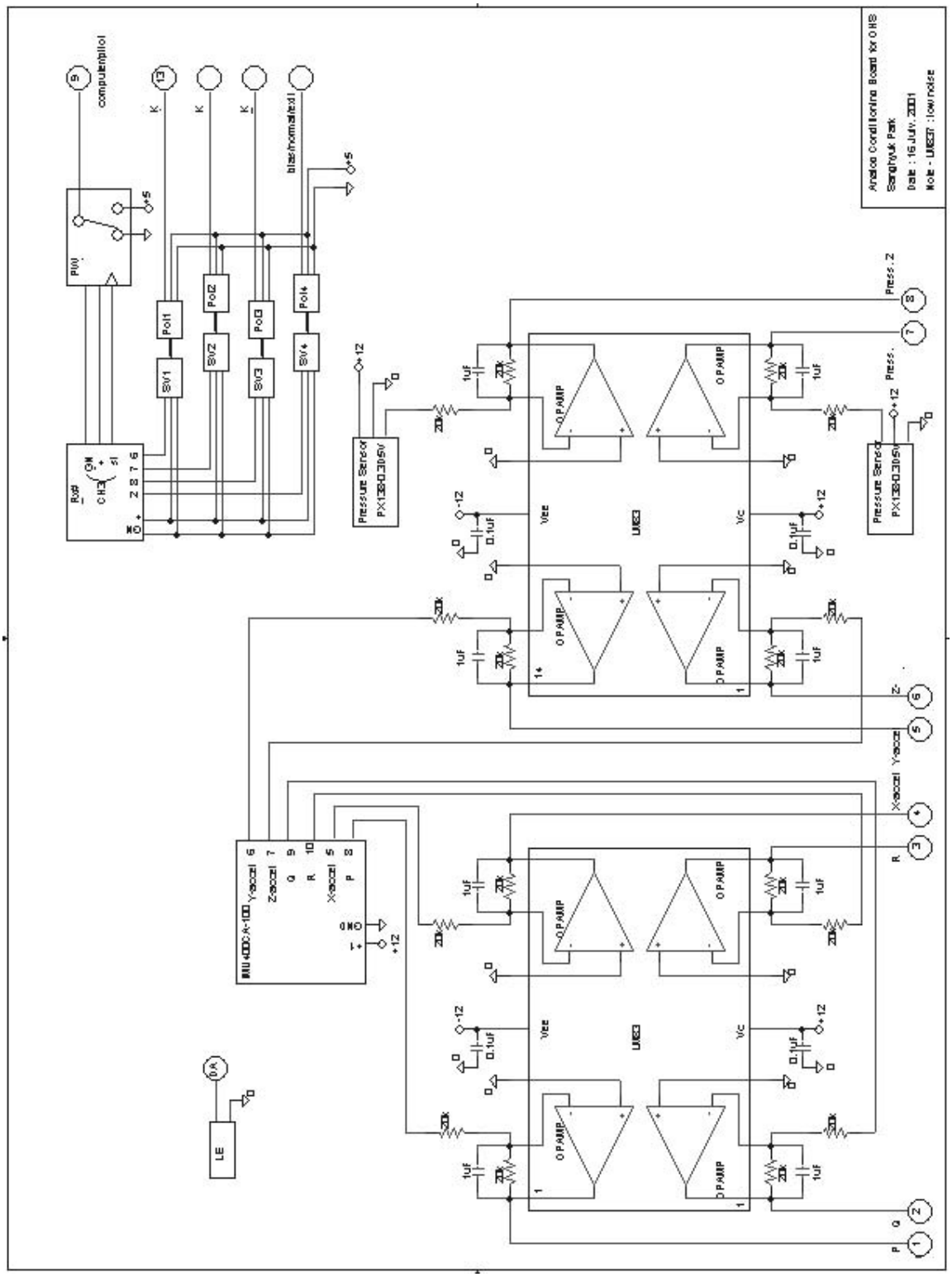

Figure A-16: Analog Conditioning Board

Nomenclature

α	angle of attack
$\bar{c}$	mean aerodynamic chord
$\bar{L}$	aerodynamic moment component about the vehicle x-axis
β	side slip angle
δ_a	aileron deflection
δ_e	elevator deflection
δ_f	flap deflection or flap mode deflection in flaperon
δ_r	rudder deflection
δ_s	sideways control surface deflection at the vertical fin in the Mini vehicle
λ	line-of-sight angle
ν	measurement noise
ω	frequency in [rad/s]
ω_{co}	crossover frequency
ϕ	roll angle or bank angle
ψ	heading angle
ρ	air density
σ	standard variation

θ	pitch angle
ζ	damping ratio
b	wing span
C_D	drag coefficient
C_{L_0}	lift coefficient at zero angle-of-attack
C_L	lift coefficient
C_l	moment coefficient about the vehicle x-axis
C_{m_o}	pitching moment coefficient with zero angle-of-attack
C_m	moment coefficient about the vehicle y-axis
C_n	moment coefficient about the vehicle z-axis
C_x	force coefficient in the direction of vehicle x-axis
C_y	force coefficient in the direction of vehicle y-axis
C_z	force coefficient in the direction of vehicle z-axis
F_x	aerodynamic force component in the direction of vehicle x-axis
F_y	aerodynamic force component in the direction of vehicle y-axis
F_z	aerodynamic force component in the direction of vehicle z-axis
h	altitude
M	aerodynamic moment component about the vehicle y-axis
m	mass
N	aerodynamic moment component about the vehicle z-axis
P	angular velocity component about the vehicle x-axis
p_E	position in the east direction
p_N	position in the north direction

pow engine power setting [0-1]

Q angular velocity component about the vehicle y-axis

R angular velocity component about the vehicle z-axis

S wing area

T_x thrust in the direction of vehicle x-axis

T_z thrust in the direction of vehicle z-axis

U velocity component in the direction of vehicle x-axis

V velocity component in the direction of vehicle y-axis

V_T speed

W velocity component in the direction of vehicle z-axis

GM gain margin

PM phase margin

subscript 1 : related with steady state value

subscript cmd : command variable

subscript est : estimate variable

subscript g : related with wind

subscript $meas$: measurement variable

subscript $MINI$: related with Mini UAV

subscript OHS : related with OHS Parent UAV

subscript s : related with stability axis, or sideways direction

superscript T : transpose

Appendix B

Modeling and Simulation

Detailed description on the dynamic modeling for the OHS Parent and the Mini vehicle are presented in the below.

B.1 Geometric and Inertial Properties

The geometric and inertial properties for the Mini vehicle are:

mass : $m = 9.1\ kg$

wing area : $S = 0.71\ m^2$

wing span : $b = 2.54\ m$

mean aerodynamic chord : $\bar{c} = 0.28\ m$

moment of inertia:

$$J_x = 0.876\ kgm^2 \quad J_y = 0.977\ kgm^2 \quad J_z = 1.802\ kgm^2$$
$$J_{xz} = 0.0268\ kgm^2 \quad J_{xy} = 0\ kgm^2 \quad J_{yz} = 0\ kgm^2$$

The OHS Parent aircraft has the following geometric and inertial properties:

mass : $m = 20\ kg$

wing area : $S = 4.5\ m^2$

wing span : $b = 2.43\ m$

mean aerodynamic chord : $\bar{c} = 0.54\ m$

moment of inertia:

$$J_x = 25.46\ kgm^2 \quad J_y = 5.05\ kgm^2 \quad J_z = 29.58\ kgm^2$$
$$J_{xz} = 0.37\ kgm^2 \quad J_{xy} = 0\ kgm^2 \quad J_{yz} = 0\ kgm^2$$

The moment of inertia of the Mini vehicle was estimated based on the pendulum setup shown in Figure B-1 for each axis. In this test setup the Mini vehicle was hang by the

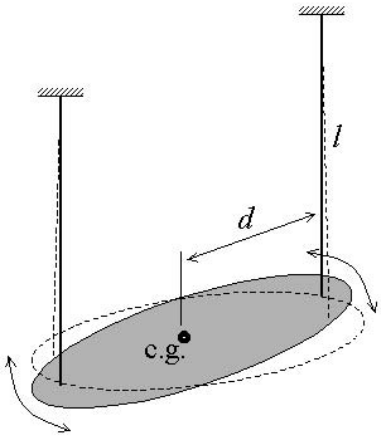

Figure B-1: Pendulum Setup for Estimation of Moment of Inertia

two strings, and was tilted about the c.g. in the horizontal plane, then was released. By measuring the period of the oscillation the moment of inertia was estimated in each axis. The associated relation

$$J_i = \frac{mgd^2T^2}{4l\pi^2}$$

is used, where T is the measured period.

For the OHS Parent, the size of this vehicle does not allow such a test. The moment of inertia for this vehicle is estimated by summing up the components of the vehicle.

B.2 Equations of Motions

The standard 6 DOF rigid body equations are used[5, Stevens].

Force and Moment Equations :

$$\begin{aligned}
\dot{V}_T &= \frac{U\dot{U} + V\dot{V} + W\dot{W}}{V_T} \\
\dot{\beta} &= \frac{\dot{V}V_T - V\dot{V}_T}{V_T^2 \cos\beta} \\
\dot{\alpha} &= \frac{U\dot{W} - W\dot{U}}{U^2 + W^2} \\
\dot{P} &= (c_1R + c_2P)Q + c_3\bar{L} + c_4N \\
\dot{Q} &= c_5PR - c_6(P^2 - R^2) + c_7M
\end{aligned}$$

$$\dot{R} = (c_8 P - c_2 R)Q + c_4 \bar{L} + c_9 N$$

where

$$\begin{aligned}
\dot{U} &= RV - QW - g\sin\theta + \frac{1}{m}(F_x + T_x) \\
\dot{V} &= PW - RU + g\cos\theta\sin\phi + \frac{1}{m}F_y \\
\dot{W} &= QU - PV + g\cos\theta\cos\phi + \frac{1}{m}(F_z + T_z)
\end{aligned}$$

In simulation, the output of the strapdown three axis accelerometer can be generated with

$$A_x = (F_x + T_x)/m, \quad A_y = F_y/m, \quad A_z = (F_z + T_z)/m$$

by considering the aerodynamic and thrust forces. It should be noted that the acceleration due to gravity is not included in the accelerometer measurement.

Kinematic Equations :

$$\begin{aligned}
\dot{\phi} &= P + \tan\theta(Q\sin\phi + R\cos\phi) \\
\dot{\theta} &= Q\cos\phi - R\sin\phi \\
\dot{\psi} &= \frac{Q\sin\phi + R\cos\phi}{\cos\theta}
\end{aligned}$$

Navigation Equations :

$$\begin{aligned}
\dot{p_N} &= U\cos\theta\cos\psi + V(-\cos\phi\sin\psi + \sin\phi\sin\theta\cos\psi) \\
&\quad + W(\sin\phi\sin\psi + \cos\phi\sin\theta\cos\psi) \\
\dot{p_E} &= U\cos\theta\sin\psi + V(\cos\phi\cos\psi + \sin\phi\sin\theta\sin\psi) \\
&\quad + W(-\sin\phi\cos\psi + \cos\phi\sin\theta\sin\psi) \\
\dot{h} &= U\sin\theta - V\sin\phi\cos\theta - W\cos\phi\cos\theta
\end{aligned}$$

where the forces and moments with respect to the body axis are computed from those with respect to the stability axis by the relations:

$$\begin{Bmatrix} F_x \\ F_y \\ F_z \end{Bmatrix} = \begin{bmatrix} \cos\alpha & 0 & -\sin\alpha \\ 0 & 1 & 0 \\ \sin\alpha & 0 & \cos\alpha \end{bmatrix} \begin{Bmatrix} F_{x_s} \\ F_{y_s} \\ F_{z_s} \end{Bmatrix}, \quad \begin{Bmatrix} \bar{L} \\ M \\ N \end{Bmatrix} = \begin{bmatrix} \cos\alpha & 0 & -\sin\alpha \\ 0 & 1 & 0 \\ \sin\alpha & 0 & \cos\alpha \end{bmatrix} \begin{Bmatrix} \bar{L}_s \\ M_s \\ N_s \end{Bmatrix}$$

where

$$\begin{aligned}
F_{x_s} &= C_{x_s}\bar{q}S \qquad & \bar{L}_s &= C_{l_s}\bar{q}Sb \\
F_{y_s} &= C_{y_s}\bar{q}S \qquad & M_s &= C_{m_s}\bar{q}S\bar{c} \\
F_{z_s} &= C_{z_s}\bar{q}S \qquad & N_s &= C_{n_s}\bar{q}Sb
\end{aligned}$$

The aerodynamic coefficients about the stability axes are obtained either from the Vortex Lattice method or from wind tunnel tests. These coefficients are described in the following sections.

The constants c_1 through c_9 are determined by the inertial properties of the vehicle by the relations:

$$\begin{aligned}
\Gamma &= J_x J_z - J_{xz}^2, & c_1 &= \tfrac{(J_y - J_z)J_z - J_{xz}^2}{\Gamma} \\
c_2 &= \tfrac{(J_x - J_y + J_z)}{\Gamma}, & c_3 &= \tfrac{J_z}{\Gamma} \\
c_4 &= \tfrac{J_{xz}}{\Gamma}, & c_5 &= \tfrac{J_z - J_x}{J_y} \\
c_6 &= \tfrac{J_{xz}}{J_y}, & c_7 &= \tfrac{1}{J_y} \\
c_8 &= \tfrac{J_x(J_x - J_y) + J_{xz}^2}{\Gamma}, & c_9 &= \tfrac{J_x}{\Gamma}
\end{aligned}$$

B.3 Aerodynamic Forces and Moments

Vortex Lattice method was extensively used in estimating the aerodynamic properties of the two vehicles. Specifically, Athena Vortex Lattice (AVL) code was used. This program employs the vortex lattice method [21, Anderson], and is available on Athena (MIT computer network). Basically, the code takes the vehicle's geometric information and flight condition, such as angle of attack and flight speed, then it computes lift, induced drag, lift loading distribution, stability derivatives, etc. It can also find the trim flight conditions for given control surface deflections. Figure B-2 shows the AVL model of the OHS Parent where the fuselage effect was assumed to be negligible and was not included in the modeling.

The coefficients of aerodynamic forces and moments with respect to the stability axis are computed by linearly summing up all the contributions.

$$\begin{aligned}
C_{x_s} &= -C_D \\
C_{y_s} &= C_{y_\beta}\beta + C_{y_p}\tfrac{P_s b}{2V_T} + C_{y_r}\tfrac{R_s b}{2V_T} + C_{y_{\delta_r}}\delta_r + C_{y_{\delta_s}}\delta_s \\
C_{z_s} &= -C_L \\
C_{l_s} &= C_{l_\beta}\beta + C_{l_p}\tfrac{P_s b}{2V_T} + C_{l_r}\tfrac{R_s b}{2V_T} + C_{l_{\delta_a}}\delta_a + C_{l_{\delta_s}}\delta_s \\
C_{m_s} &= C_{m_0} + C_{m_\alpha}\alpha + C_{m_q}\tfrac{Q_s \bar{c}}{2V_T} + C_{m_{\delta_e}}\delta_e + C_L(X_{cg} - X_{ref}) + C_{m_{\delta_f}}\delta f \\
C_{n_s} &= C_{n_\beta}\beta + C_{n_p}\tfrac{P_s b}{2V_T} + C_{n_r} r + C_{n_{\delta_r}}\delta_r + C_{y_s}(X_{cg} - X_{ref}) + C_{n_{\delta_a}}\delta_a + C_{n_{\delta_s}}\delta_s
\end{aligned}$$

where

$$\begin{aligned}
P_s &= P\cos\alpha + R\sin\alpha \\
Q_s &= Q \\
R_s &= -P\sin\alpha + R\cos\alpha
\end{aligned}$$

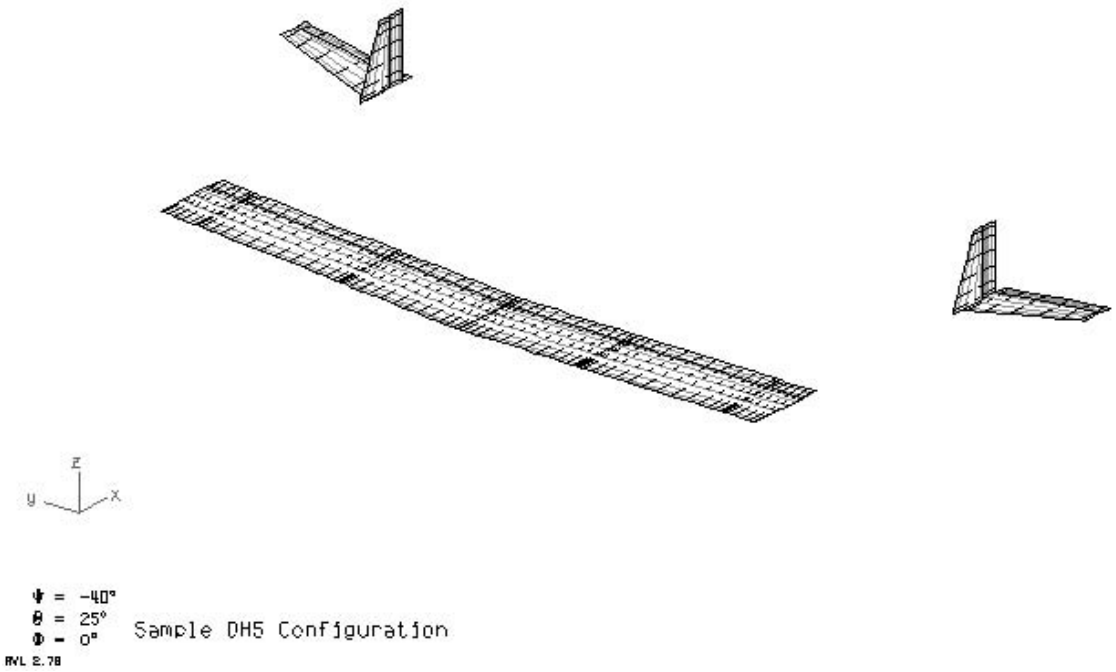

Figure B-2: AVL Model for OHS Parent

and

$$C_L = C_{L_0} + C_{L_\alpha}\alpha + C_{L_q}\frac{Q_s\bar{c}}{2V_T} + C_{L_{\delta_e}}\delta_e + C_{L_{\delta_f}}\delta_f$$
$$C_D = C_D(\alpha, \delta_f)$$

where the effect of α and δ_f on C_D are separately computed with second order polynomial approximations obtained in AVL and added together. It should be noted that the effect of the flaperon(δ_f) and sideways control surface(δ_s) deflections are also added into the equations. This is true only for the Mini vehicle.

The coefficients required to compute the aerodynamic forces and moments around the proposed flight condition are obtained by AVL. The control derivatives can also be estimated in AVL by deflecting each concerned control surface in the AVL model.

The static derivatives and the control derivatives were also obtained from the wind tunnel data. These aerodynamic coefficients are summarized in Table B.1 for the Mini vehicle and in Table B.2 for the OHS Parent aircraft.

It should be noted that C_{l_β} from the wind tunnel data is greater than that by the AVL model. This is because of the high wing effect. The fuselage section was modeled smaller in the AVL model for the Mini vehicle. Another point is that the control surface

C_{Lo}	C_{Mo}	C_{L_α}	C_{M_α}	C_{y_β}	C_{l_β}	C_{n_β}	C_{y_p}	C_{l_p}
0.0278	0.008	5.45	-1.10	-0.645	-0.0279	0.0576	0.0232	-0.541
		5.96	-1.17	-0.885	-0.0755	0.0870		
C_{n_p}	C_{L_q}	C_{M_q}	C_{y_r}	C_{l_r}	C_{n_r}	$C_{M_{\delta_e}}$	$C_{L_{\delta_e}}$	$C_{y_{\delta_r}}$
-0.0396	9.98	-12.9	0.236	0.146	-0.064	-1.65	0.745	0.183
						-1.2	0.20	0.206
$C_{n_{\delta_r}}$	$C_{L_{\delta_f}}$	$C_{M_{\delta_f}}$	$C_{y_{\delta_s}}$	$C_{n_{\delta_s}}$	$C_{l_{\delta_a}}$	$C_{n_{\delta_a}}$	$C_{l_{\delta_s}}$	
-0.063	2.06	-0.183	0.183	0.000	-0.458	0.0057	-0.0057	
-0.061	1.73	-0.120	0.110	0.000	-0.231	0.000	-0.003	

Table B.1: Aerodynamic Characteristics of Mini (reference : 1/4 $\bar{c}$ from L.E.)
(Note: *The numbers in the upper row represent the AVL results, and the bottom is for the wind tunnel data.*)

effectiveness is in general oversized in the AVL model. That is mainly because the airfoil thickness is not considered in AVL. Also, because of the effect of the wake behind the fuselage, the coefficients for the elevator deflection are smaller in the wind tunnel data than in AVL methods. The effectiveness of the sideways control surface is also smaller in the wind tunnel than in the AVL model, which is again likely to be due to the fuselage effect. In the controller design of the Mini vehicle the wind tunnel data was used.

B.4 Actuator and Sensor Modeling

Control Surface with Servo Motor

A simple first order low pass linear filter was used in modeling the dynamics from the control surface deflection command to the actual deflection. The cutoff frequency was chosen based on the slew-rate limitation from the specification of a servo motor. This is reported in the next. In the frequency range less than the cutoff frequency, sinusoidal deflection of a servo arm can be expressed as:

$$\delta = A\sin\omega t \quad \Rightarrow \quad \dot{\delta} = A\omega\cos\omega t$$

C_{Lo}	C_{Mo}	C_{L_α}	C_{M_α}	C_{y_β}	C_{l_β}	C_{n_β}	C_{y_p}	C_{l_p}
-0.0093	0.0276	5.55	-1.60	-0.294	-0.028	0.10	-0.12	-1.05
C_{n_p}	C_{L_q}	C_{M_q}	C_{y_r}	C_{l_r}	C_{n_r}	$C_{M_{\delta_e}}$	$C_{L_{\delta_e}}$	$C_{y_{\delta_r}}$
-0.0188	7.11	-16.0	0.247	0.106	-0.085	-1.43	0.401	0.247
$C_{n_{\delta_r}}$	$C_{l_{\delta_a}}$	$C_{n_{\delta_a}}$	$C_{D_{truss}}$	$C_{M_{truss}}$				
-0.085	-0.329	-0.024	0.021	0.024				

Table B.2: Aerodynamic Characteristics of OHS Parent (reference: 55% $\bar{c}$ from L.E.)
(Note: *The numbers represent AVL results. Truss effect is included in drag and moment.*)

Since the maximum of $\dot{\delta}$ is limited, the corresponding critical frequency where the servo begins to reach its maximum speed is

$$\omega_{cr} = \frac{\dot{\delta}_{limit}}{A}$$

where A is the amplitude of the servo arm deflection. This is the frequency where the sinusoidal motion begins to be distorted and this frequency is chosen as the cutoff of the low pass filter. For example, if the typical movement of the surface deflection is $\pm 15^o$, and if the linkage ratio between the servo arm and the control surface deflection is 2, then $A = 30^o$. If the slew rate limit is $375^o/sec$ (for Hitec HS-85MG+), then

$$\omega_{cr} = \frac{375^o/sec}{30^o} = 12.5\ rad/s$$

Thrust and Engine

For the Mini vehicle, 0.91 cu.in. internal combustion (IC) engine and 12-6 propeller are used. For the OHS Parent, 2.1 cu.in. IC engine and 22-8 propeller are used. The amount of thrust can be expressed as:

$$T = T_{static} + K \cdot V$$

where T_{static} is the thrust value under zero velocity condition. From the static thrust test on the ground the following approximations are obtained.

$$T_{static} = -8.72pow^3 + 11.1pow^2 + 1.75pow + 0.10 \text{ [kg]} \quad \text{for Mini (4.5 [kg] max.)}$$

$$T_{static} = -6.0pow^2 + 15.0pow \text{ [kg]} \quad \text{for OHS Parent (9.0 [kg] max.)}$$

where pow is the power setting between 0∼1.0. The term $K \cdot V$ is the correction for the forward velocity(V), where the correction factor K is given [45, Urbain] by

$$K = K_o \frac{T_{static}}{(T_{static})_{max}}, \qquad K_o = -0.0671[kg \cdot sec/m]$$

The dynamics of the IC engine is modeled with a first order low pass filter. Time constants of 0.5 and 1.0 second were used for the Mini and the Parent engines respectively.

Sensor

For the GPS output variables, time delay of 0.4 second is modeled in simulations. For other analog sensors the low pass filter due to the anti-aliasing filter are included.

B.5 Wind Effect

Since the demonstration vehicles fly at low altitude (usually below 150 m), only the wind components parallel to the ground surface are considered here. A first order low pass filter with time constant at 2 seconds was used for the shaping of the wind disturbance, and up to 5 m/s (≈ 11 mi/h) of wind speed is considered, which is more than 20 percent of the vehicle speed. The flight tests were usually scheduled when the weather forecasts predict less than 11 mi/h wind speed. But there were a few cases when the test was performed with ∼ 7 m/s wind.

Depending on the wind direction and the attitude of the vehicle, wind velocity components (U_g, V_g, W_g) along the vehicle body x,y,z-axes cause aerodynamic forces and moments. Here, the changes of total velocity, angle of attack, and sideslip angle are considered in the model with the following relations [42, Roskam]:

$$\begin{aligned} V_T &= \sqrt{(U - U_g)^2 + (V - V_g)^2 + (W - W_g)^2} \\ \alpha_A &= \alpha + \alpha_g \\ \beta_A &= \beta + \beta_g \end{aligned}$$

where

$$\alpha_g = -\frac{W_g}{U_1}, \qquad \beta_g = \frac{V_g}{U_1}$$

and U_1 is the steady state vehicle velocity component in the x-direction. These expressions for V_T, α_A, and β_A are used in the computation of the aerodynamic forces and moments,

which is described in Section B.3. Because these quantities are induced by relative wind rather than the motion of the vehicle, they shouldn't be applied directly to the inertial terms in the differential equations described in Section B.2.

B.6 Trim Analysis and Linearization

The non-linear 6-DOF model is built based on the equations described in the previous sections using the Matlab simulink environment for the two vehicles. In order to apply linear controller, first a trim condition needs to be imposed, and then the linear model around the trim condition should be extracted. Assuming the vehicle doesn't have to do any aggressive maneuver involving large pitch or bank angles during the air rendezvous, a linearized model around a steady level flight condition is required.

Thus, a steady state trimmed flight condition is found from the non-linear model using the Matlab optimization toolbox function 'fminsearch'. The flight condition is imposed in the model by the relations:

$V_T = 22\ m/s$	:	as proposed from the power-speed curves
$\theta = \alpha$	:	specified for level-flight with γ=0.
$\phi = 0, P = 0, Q = 0, R = 0$	:	steady-state level
$\delta_f = 0, \delta_s = 0$	:	flaperon and sideways control surface are not used to trim the aircraft for the steady-state level flight.

The function

$$cost = \dot{V_T}^2 + 100(\dot{\alpha}^2 + \dot{\beta}^2) + 10(\dot{P}^2 + \dot{Q}^2 + \dot{R}^2)$$

is chosen as the cost to be minimized in the 'fminsearch', while 100 and 10 are multiplied as weighting factors for faster numerical results. The following trim conditions are found from the algorithm

$$V_T = 22\ m/s,\ \alpha = 1.4^o,\ \delta_e = -1.53^o,\ pow = 0.43,\ \beta, \delta_r, \delta_a \approx 0$$

for the Mini and

$$V_T = 22\ m/s,\ \alpha = 2.9^o,\ \delta_e = -1.54^o,\ pow = 0.49,\ \beta, \delta_r, \delta_a \approx 0$$

for the OHS Parent.

A linear model is then numerically extracted around the trim conditions. The Matlab function 'linmod' is used, where the nonlinear simulink model and the steady state conditions are imposed in the use of this function. The output of the 'linmod' in state space form, showed that the longitudinal and lateral modes are decoupled. Table B.3 and B.4 summarize the longitudinal and lateral mode properties for the Mini and the OHS Parent airplanes. The two tables indicate that the frequency of the short period mode is faster for

	eigenvalues	descriptions
longitudinal	-5.65±8.10i	short period : ω_{n_s}=9.9 rad/s(=1.6 Hz), ζ_s=0.57
	-0.08±0.58i	phugoid : ω_{n_p}=0.58 rad/s(=0.09 Hz), ζ_p=0.14
lateral	-19.04	roll mode
	-1.06±5.33i	dutch roll : ω_{n_d}=5.44 rad/s(=0.87 Hz), ζ_d=0.19
	0.0651	spiral

Table B.3: Mode Characteristics : Mini

	eigenvalues	descriptions
longitudinal	-12.2±9.9i	short period : ω_{n_s}=15.7 rad/s(=2.5 Hz), ζ_s=0.78
	-0.15±0.41i	phugoid : ω_{n_p}=0.44 rad/s(=0.07 Hz), ζ_p=0.34
lateral	-13.7	roll mode
	-0.70±3.31i	dutch roll : ω_{n_d}=3.38 rad/s(=0.54 Hz), ζ_d=0.21
	0.017	spiral

Table B.4: Mode Characteristics : OHS Parent

OHS than for Mini vehicle. Considering the sizes and inertias of the vehicles it is contradictory to the intuition. This can also be explained by the unique aerodynamic feature of the outboard horizontal stabilizer configuration mentioned in Section 2.1, where the horizontal tail surface is placed in such as way to give more restoring force than conventional airplane due to the wing vortex changes when the vehicle is disturbed about pitch axis. This larger restoring moments results in the faster short period mode for the OHS Parent.

B.7 OHS Tail Boom Flexibility

Because of the vehicle configuration of OHS, the flexibility effect of the tail section needs to be considered. It was found by a simple test in the lab that the oscillation of the tail section is mainly due to the twist of the main wing. The following assumptions are used in the modeling of the flexible tail section.

1. The dynamics is simplified by two rigid bodies(wing-fuselage and tail-section) motions with spring and damper at the joint as shown in figure B-3.

2. Inertia of wing-fuselage section is much larger than that of the tail section. Also, for the wing-fuselage section there is no significant aerodynamic force that can change its pitching moment compared to the tail section. So it is assumed that the fuselage section doesn't move. If this assumption is not true (i.e. the amount of deflections of the two body sections are about same), the natural frequency of this spring mass system would be higher (which is better) than the values computed with this assumption.

3. The elevator deflection and angle of attack changes are considered as major disturbing sources for the tail boom deflection.

4. Only perturbed dynamics regarding the pitching moment change is considered here.

The lift on the tail surface is modeled as the linear combination of the elevator deflection, the tail boom deflection angle and its rate, and the angle of attack change:

$$\begin{aligned} F_h &= F_h(\delta_e, \eta, \alpha, \dot{\eta}, ...) \\ &= c_1\delta_e - c_2\eta + c_2\alpha - c_2\frac{l_h\dot{\eta}}{V_{trim}} \end{aligned}$$

where

$$\begin{aligned} c_1 &= \frac{1}{2}\rho V^2 S_h C_{L_{\alpha_h}}\tau \\ c_2 &= \frac{1}{2}\rho V^2 S_h C_{L_{\alpha_h}} \end{aligned}$$

where τ is a function of the ratio between the area of elevator and that of tail surface.
The moment equation about the joint point for the tail section is found from the free diagram in Figure B-3.

$$\begin{aligned} I_{h_o}\ddot{\eta} + b\dot{\eta} + k\eta &= l_h F_h \\ &= l_h\left(c_1\delta_e - c_2\eta + c_2\alpha - c_2\frac{l_h\dot{\eta}}{V_{trim}}\right) \end{aligned}$$

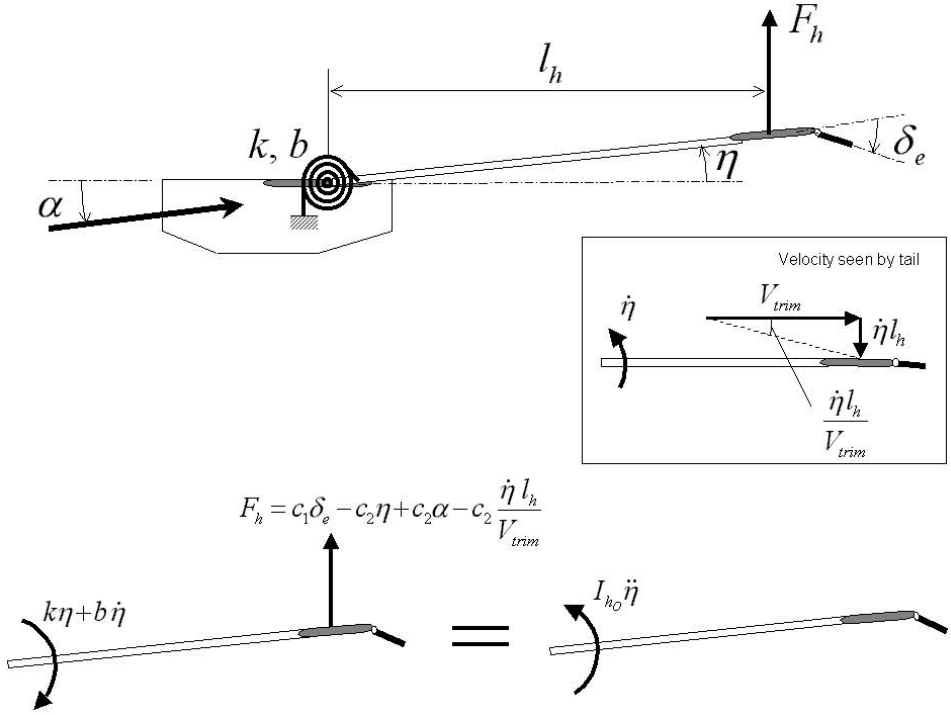

Figure B-3: Modeling of Flexible Tail Section for OHS Parent Vehicle

where I_{h_o} is moment of inertia of the tail section. After the Laplace transformation, boom deflection angle is expressed as

$$\eta(s) = \frac{l_h c_1}{I_{h_o}s^2 + (b + c_2\frac{l_h\dot{\eta}}{V_{trim}})s + (k + l_h c_2)}\delta_e + \frac{l_h c_2}{I_{h_o}s^2 + (b + c_2\frac{l_h\dot{\eta}}{V_{trim}})s + (k + l_h c_2)}\alpha$$

The moment change felt by the main body section is

$$\begin{aligned} M_{by\ tail} &= -(k\eta + b\dot{\eta}) \\ &= -l_h F_h + I_{h_o}\ddot{\eta} \\ &= -l_h\left(c_1\delta_e - c_2\eta + c_2\alpha - c_2\frac{l_h\dot{\eta}}{V_{trim}}\right) + I_{h_o}\ddot{\eta} \end{aligned}$$

Laplace transforming this and substituting the expression for $\eta(s)$ yields

$$M_{by\ tail} = -l_h c_1\left[1 - \underbrace{\frac{I_{h_o}s^2 + c_2\frac{l_h^2}{V_{trim}}s + l_h c_2}{I_{h_o}s^2 + (b + c_2\frac{l_h^2}{V_{trim}})s + (k + l_h c_2)}}_{(A)}\right]\delta_e(s)$$

$$-l_h c_2 \left[1 - \frac{I_{h_o} s^2 + c_2 \frac{l_h^2}{V_{trim}} s + l_h c_2}{\underbrace{I_{h_o} s^2 + (b + c_2 \frac{l_h^2}{V_{trim}}) s + (k + l_h c_2)}_{(B)}} \right] \alpha_e(s)$$

Note that the subtracted terms are from the flexibility effect. They can be considered as

- (A) represents moment loss due to servo-tab effect induced from elevator deflection
- (B) represents moment loss due to weathercock motion of the tail boom itself induced from angle of attack change.

Assuming the major moment contribution is from the horizontal tail, the terms $-l_h c_1$ and $-l_h c_2$ can be replaced by $\bar{q} S \bar{c} C_{M_{\delta_e}}$ and $\bar{q} S \bar{c} C_{M_\alpha}$ respectively. The following physical properties can also be noted.

- if no flexibility, i.e. $k \rightarrow \infty$, then (A), (B) $\rightarrow 0$
- if no spring and damping resistance, i.e. $k,\ b \rightarrow 0$, then (A), (B) $\rightarrow 1$
- if V $\rightarrow \infty$, then DC gain $\left(= \frac{-\frac{1}{2}\rho V^2 S \bar{c} C_{m_{\delta_e}}}{k - \frac{1}{2}\rho V^2 S \bar{c} C_{m_{\delta_e}}} \right)$ of (A), (B) $\rightarrow 1$

From a vibration test on the OHS vehicle in the lab, the following values for the moment of inertia, spring constant, and the damping constant are obtained :

$$\begin{aligned} I_{h_o} &= 4.0\ kg \cdot m^2 \\ k &= 762\ N \cdot m \\ b &= 11.0\ N \cdot m/s^{-1} \end{aligned}$$

From the above analysis the following results are obtained.

		V=0.0		V=22.0 m/s
natural frequency	:	2.2 Hz	$\rightarrow$	3.0 Hz
damping ratio	:	0.10	$\rightarrow$	0.44

Because of the aerodynamics effect when the vehicle has forward speed, the natural frequency and the damping ratio are increased compared to the situation where the vehicle has no speed. This simple analysis results agree with the analysis done by Jason Kepler in the team [26, Kepler], where he used the Aswing, a program created by Professor Mark

Drela at MIT that combines computational fulid dynamics with structural finite element methods to analyze both the steady and unsteady aerodynamics of flexible bodies. Furthermore in his analysis, the damping ratio increases up to a certain speed around 50 m/s and begins to decrease and becomes zero at around 80 m/s, where the structural divergence occurs.

B.8 Downwash behind OHS

During the Phase II of air rendezvous the Mini is supposed to be exposed to the downwash airfield induced by the OHS Parent since the Mini vehicle approaches the Parent from behind. The downwash velocity field was estimated by Sarah Saleh in the team using the AVL. A thin and long lifting surface which doensn't affect the overall air flow is placed at several location behind the OHS main wing. The lift coefficient of the thin stripe was recorded, and from this the downwash velocity are computed. The 3-D graph in Figure B-4 summarizes the results, where the downwash velocities at several locations are shown with different levels of darkness. The graph was obtained under the flight condition of 5 degree angle of attack. The graph indicates that the downwash is the strongest at the same level of hight with the main wing, where the downwash exceeds 1 m/s right behind the wing and it decreases as the point moves further backward from the wing. The fact that the angle of attack of the OHS Parent here is assumed to be 5 degrees which is higher than the trimmed value, and the downwash velocity is 1 m/s right behind, doesn't indicate a severe problem. But this analysis suggests that the trailing vehicle should approach the larger one from either lower or higher altitude.

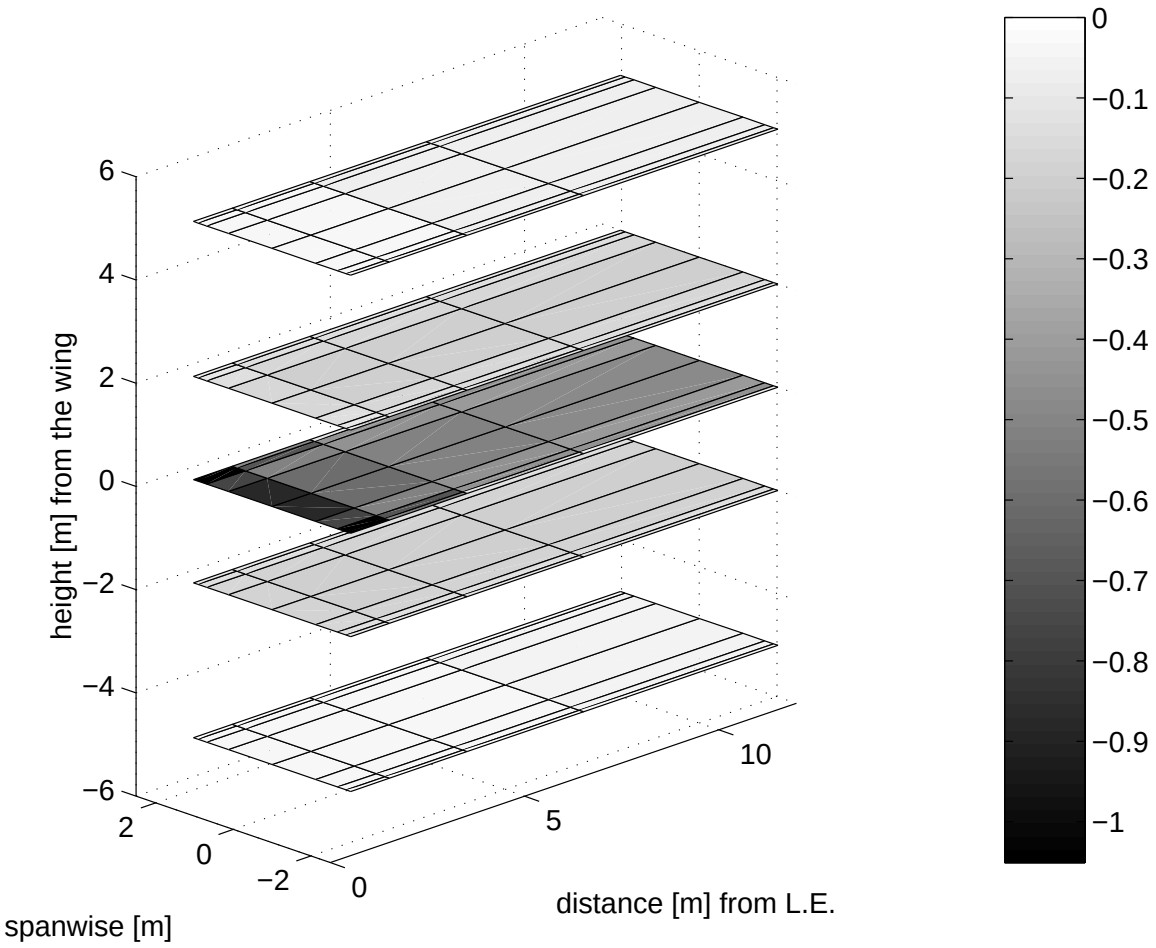

Figure B-4: Downwash [m/s] behind OHS - under V=22 m/s, angle of attack=5 deg.

Appendix C

Controller Design and Analysis

C.1 Lateral and Directional Controller

Discussed below is the detailed description of the controller design and analysis for the Mini UAV as an example. So the specific numbers and figures shown in this section are associated with the Mini vehicle unless otherwise noted. But the same controller structure is used for both Mini and OHS Parent.

Yaw Damper with Washout

The first step in creating the lateral and directional controller is the design of the yaw damper. The purpose of this rate damping is to improve the damping ratio of the dutch roll mode. The use of rudder control surface is often the efficient way of improving this mode [11, Drela]. The vehicle yaw rate is easily estimated with a rate gyro and a simple proportional control is used to generate the rudder command in closing this loop. But a wash-out should be added because any reasonable slow change in the yaw rate during the intentional turning of an aircraft should not be suppressed. A first-order high pass filter was added for the wash-out. The cutoff frequency of this filter should be chosen in the frequency range lower than the dutch roll frequency. For the two demonstration UAVs the cutoff frequency of 1 rad/s was chosen in the high pass filter.

The control gain of the yaw damper was selected based on the root locus plot. Figure C-1 (a) shows the root locus of the characteristic equation of the lateral dynamics of the Mini vehicle. From the root locus plot the gain is chosen where the damping is maximized. The

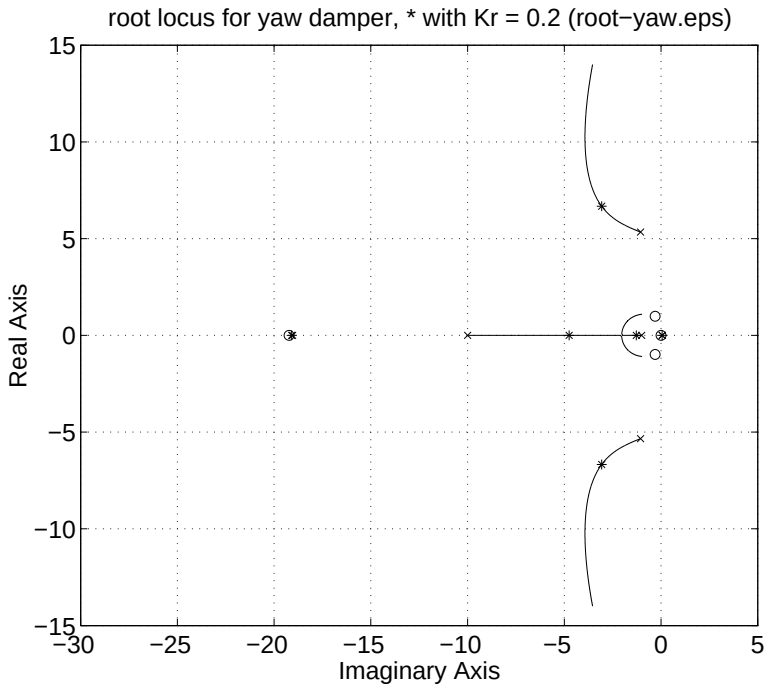

(a) Root locus for yaw damper design

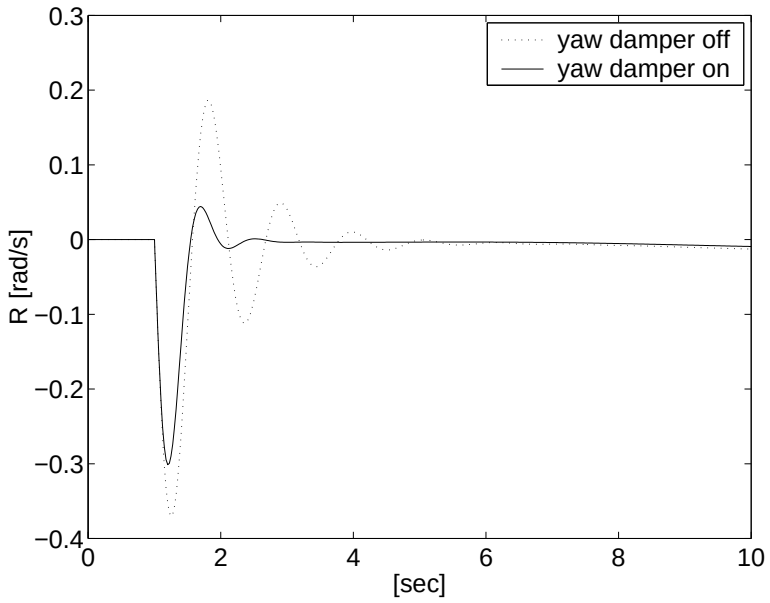

(b) Sideways gust step responses

Figure C-1: Yaw Damper

damping ratio is increased from 0.2 to 0.5, and the resulting pole locations are marked by '*' in the graph. Figure C-1 (b) shows the time responses of the vehicle yaw rate to the sideways step gust. The step disturbance input is imposed at 1 second in the simulations. The dotted line is for the case where the yaw damper is not included, and the solid line is for the case with the yaw damper included. The comparison from the simulation indicates that the damping characteristics is improved by the use of the yaw damper.

Bank Angle Controller

Bank angle controller is designed next. It starts with the airplane model that includes the yaw damper. For most aircrafts, the vehicle sideways acceleration is generated by banking the plane, which changes the direction of the lift vector. In many flight conditions, it can be shown that the sideways acceleration is approximated to be simply proportional to the bank angle with a factor of the gravity constant. In other words, the amount of the lateral acceleration of an airplane can be controlled by controlling the amount of bank angle. Thus bank angle controller could serve as an inner loop control, and an outer loop guidance law can be closed around it.

A proportional-integral(PI) compensator is used for a bank angle controller. Figure C-2 shows the loop shaping with this controller. The bode plots for the plant $G(j\omega)$ and the loop transmission $K(j\omega)G(j\omega)$ are shown with the solid line and the dotted line respectively. With the chosen PI controller, the crossover frequency of the loop transmission is obtained at 2.5 rad/s with the associated gain margin of 6.2 and the phase margin of 74 degrees.

Figure C-3 shows the simulation for step reference input of 10 degrees of bank angle command. The first plot is for the bank angle, and the second plot is for the associated aileron control surface deflection. The bank angle quickly rises to the command angle of 10 degrees in less than a second.

Finally, Figure C-4 shows the data from a flight test which was performed to check the bank angle controller. During this specific flight test it was set up such that only the lateral control were controlled by the computer. The pilot was still able to control the engine throttle and the elevator. In the test the reference command for the vehicle bank angle was changed from one of the copilot dials. The reference command is shown in the dashed line in the upper plot. The bank angle command was changed in the range between -20 and +20 degrees. The solid line shows the onboard bank angle estimate. The flight data indicates

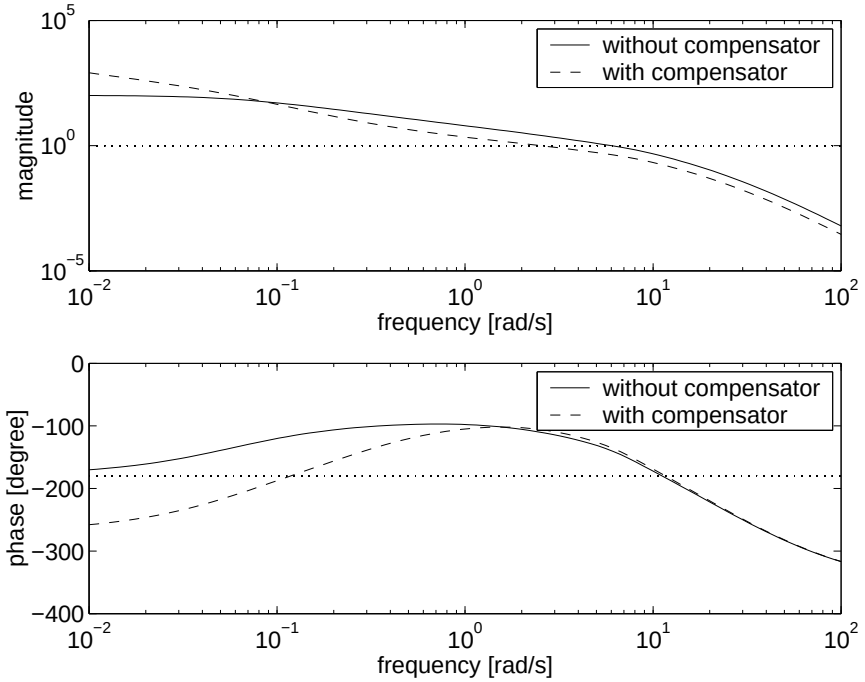

Figure C-2: Bode Plots for Bank Angle Controller

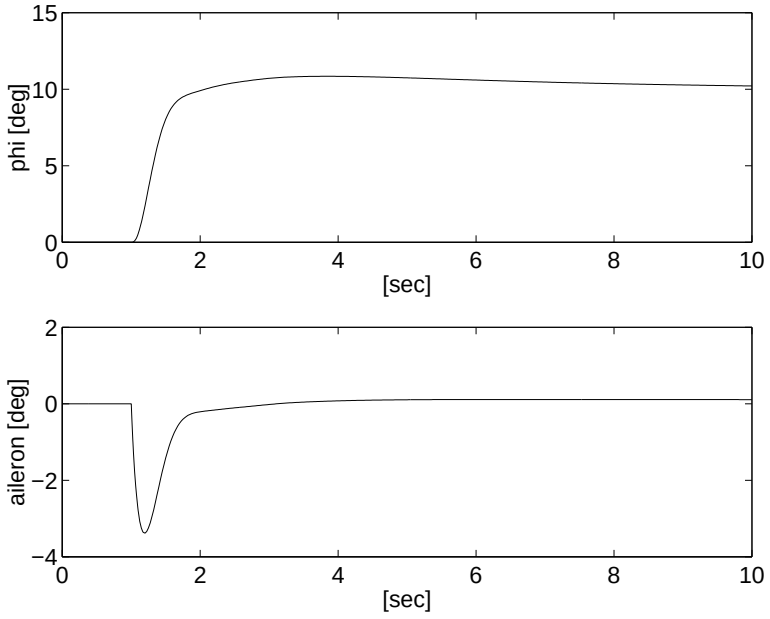

Figure C-3: Bank Angle Controller Simulation with 10 degrees of step bank angle command

that the bank angle follows its command quite well with the same level of performance indicated in the simulation. The bottom plot shows the corresponding command changes

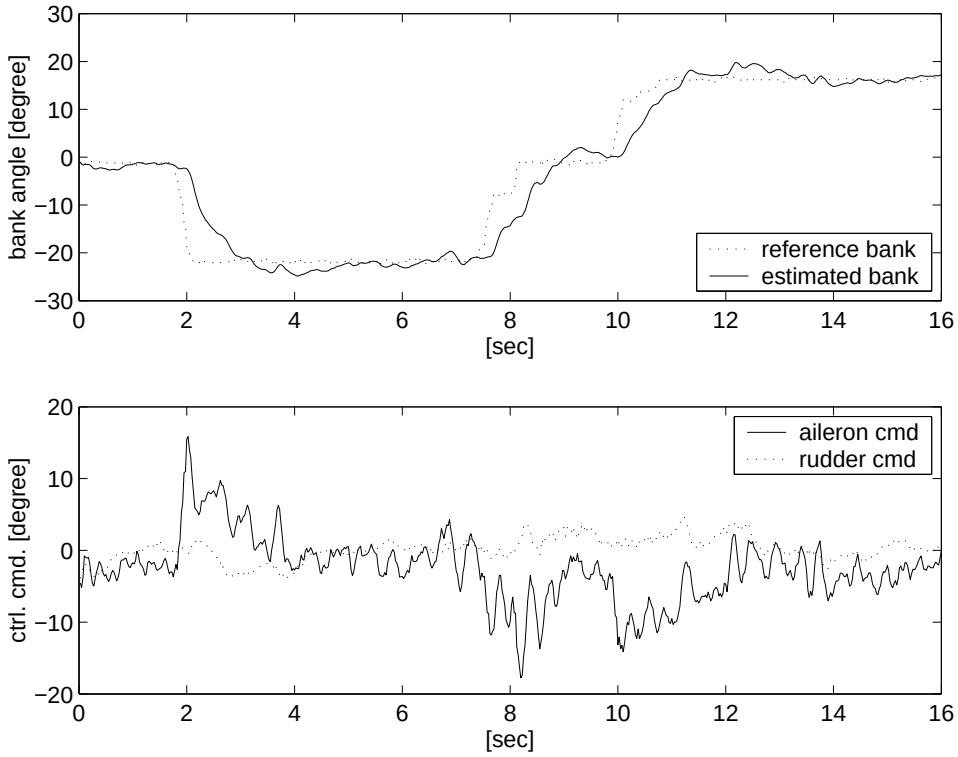

Figure C-4: Flight Test Data for Bank Angle Controller

in the aileron. The change of the rudder deflection due to the yaw damper controller is also shown together although the yaw rate data is omitted here.

C.2 Longitudinal Controller

The aim of the longitudinal controller is to follow the speed and the altitude commands which are imposed by higher level guidance and planning algorithm described in Chapter 3 and 5. In the longitudinal airplane dynamics there is a significant coupling between the two control inputs(engine power, elevator) and the two main outputs(speed, altitude). Due to this directional interactions, decentralized diagonal controller configuration is not expected to perform well in this case [44, Skogestad & Postlethwaite]. Therefore, it was decided to deploy a multivariable control technique. Here a linear quadratic regulator(LQR) was used in order to take the advantage of the excellent robustness of LQR [50, Zhou]. In order to comply with the full state feedback condition for the LQR controller, the controller design was performed with a reduced order model with the basic airplane longitudinal dynamics. This means that the high frequency dynamics of the actuators and sensors are not included

in the design phase. But, those missing components are included later in the analysis phase.

In the following is presented the procedure of the LQR design. It starts by considering the basic linearized longitudinal model.

$$\dot{x}_1 = A_1 x_1 + B_1 u$$

where

$$x_1 = [v_t \ \alpha \ \theta \ q]^T, \quad u = [pow \ \delta_e]^T$$

$$A_1 = \begin{bmatrix} \text{-0.17} & 13.9 & \text{-9.81} & 0 \\ \text{-0.04} & \text{-6.3} & 0 & 0.93 \\ 0 & 0 & 0 & 1 \\ 0.081 & \text{-70.6} & 0 & \text{-4.95} \end{bmatrix}, \ B_1 = \begin{bmatrix} 4.15 & 0 \\ 0 & \text{-0.21} \\ 0 & 0 \\ \text{-1.9} & \text{-72.4} \end{bmatrix}$$

Next, remembering that the altitude rate v_h can be expressed in the linearized dynamics as

$$v_h = V_{trim}(-\alpha + \theta) = -22\alpha + 22\theta$$

the integrated variables are introduced for the tracking of the speed and altitude rate commands. Their dynamics are expressed as

$$\dot{e}_{v_{t_i}} = v_{t_{cmd}} - v_t$$

$$\dot{e}_{v_{h_i}} = v_{h_{cmd}} - v_h = v_{h_{cmd}} - (-22\alpha + 22\theta)$$

The augmented dynamics can now be written as

$$\dot{x} = Ax + Bu$$

where

$$x = [v_t \ \alpha \ \theta \ q \ e_{v_{t_i}} \ e_{v_{h_i}}]^T, \ u = [pow \ \delta_e]^T$$

$$A = \begin{bmatrix} \text{-0.17} & 13.9 & \text{-9.81} & 0 & 0 & 0 \\ \text{-0.04} & \text{-6.3} & 0 & 0.93 & 0 & 0 \\ 0 & 0 & 0 & 1 & 0 & 0 \\ 0.081 & \text{-70.6} & 0 & \text{-4.95} & 0 & 0 \\ \text{-1} & 0 & 0 & 0 & 0 & 0 \\ 0 & 22 & 22 & 0 & 0 & 0 \end{bmatrix}, \ B = \begin{bmatrix} 4.15 & 0 \\ 0 & \text{-0.21} \\ 0 & 0 \\ \text{-1.9} & \text{-72.4} \\ 0 & 0 \\ 0 & 0 \end{bmatrix}$$

Based on the augmented model, LQR design is performed next. For the quadratic performance index

$$J = \frac{1}{2}\int_0^\infty x^T Q x + u^T R u \; dt$$

Bryson rule [2, Bryson] gives a good starting point for the choice of the design matrices Q and R. The rule uses diagonal matrices whose diagonal elements are in the form of $1/(z_{j_{max}})^2$ for each variables j. By trial and error using Matlab lqr.m function, the final chosen combination for the Mini vehicle is

$$z_{v_{t_{max}}} = 0.75,\ z_{\alpha_{max}} = 5/57.3,\ z_{\theta_{max}} = 10/57.3,\ z_{q_{max}} = 0.3,\ z_{vt_{i_{max}}} = 4,\ z_{v_{h_{i_{max}}}} = 1.5,$$

$$z_{pow_{max}} = 0.15,\ z_{\delta_{e_{max}}} = 2.5/57.3$$

When all the other ignored dynamics(such as engine, servo, sensor models, and flexible tail boom effect for OHS Parent vehicle) are included, the combination of the Q and R matrices results in the following loop transmission(LT) properties at the engine and the elevator control inputs

engine LT : $\omega_{crossover}$=0.98 rad/s, PM=54, GM=11.4

elevator LT : $\omega_{crossover}$=3.04 rad/s, PM=69, GM=10.2

The phase margin and the gain margin are not in general a good measure for the robustness in a MIMO system [44, Skogestad & Postlethwaite]. But in the design phase during the iteration for choosing the matrix Q and R, the crossover frequency and the two margins were checked until these values become good enough. The robustness of this controller comes from the nature of an LQR controller.

The corresponding control gain matrix for the Mini vehicle is found to be

$$K = \begin{bmatrix} 0.1892 & 0.4003 & -0.5857 & -0.0419 & -0.0360 & -0.0280 \\ 0.0077 & 0.5340 & -0.7719 & -0.1137 & -0.0031 & 0.0279 \end{bmatrix}$$

This gives the following reaction properties summarized in Table C.1. It should be noted that both engine power and elevator are simultaneously used to control the speed or the altitude rate. Specifically, in gaining the flight speed, the control reactions are such that the engine power is increased and the elevator is deflected downward. This combination is a good feature to prevent an airplane from slowing down to a stall speed.

This linear quadratic controller was used for both vehicles in both rendezvous phases as a low level controller. Different guidance loops were closed around it depending on the rendezvous phases.

Deviations			*Controller Responses*		*Primary Control*
			Throttle(0∼1)	Elevator	
$v_{cmd} - v$	:	+1 m/s	+0.2	0.5 deg. down	both
α	:	+1 deg.	-0.007	0.5 deg. up	elevator
θ	:	+1 deg.	+0.01	0.8 deg. down	elevator
q	:	+1 rad/s	+0.04	5.7 deg. down	elevator
$\int v_{cmd} - vdt$	:	+1 m/s × 10s	+0.4	1.7 deg. down	both
$\int \dot{h}_{cmd} - \dot{h}dt$	:	+1 m/s × 10s	+0.3	17 deg. up	both

Table C.1: Inspection of Longitudinal LQR Gains (example Mini)

During phase I the altitude command is provided from the higher level path planning algorithm. In order to follow the altitude command an additional outer controller is cascaded around the linear quadratic controller. This outer loop controller generates the altitude rate command.

In the design of the outer loop controller, the classical design technique is used. The combination of a lead compensator(with 33 degrees of phase lead) and a PI controller is used. Figure C-5 shows the bode plots for the plant and the associated loop transfer functions in the design of the altitude hold controller. It indicates that the gain crossover frequency is chosen at 0.74 rad/s, with the associated phase margin of 50 degrees and the gain margin of 2.44.

The entire longitudinal controller with the LQR and the outer loop altitude controller is now analyzed in terms of its capabilities in controlling the speed and the altitude. Figure C-6 shows the performance of the disturbance rejection capability for the Mini vehicle in the longitudinal dynamics. It plots the transfer functions from each disturbance source (longitudinal direction wind U_g and the vertical direction wind W_g) to each of the control output (altitude error and speed error) variables. The transfer functions shown in the plots are the ones that also include the wind shaping low pass filter with τ=2 seconds. Furthermore, the inputs for the wind were scaled with the magnitudes of 5 m/s and 2.5 m/s for $|U_g|$ and $|W_g|$ respectively. The reason for the choice of 2.5 m/s is from the assumption that if there is a wind parallel to the ground with a speed of 5 m/s, and if the airplane is

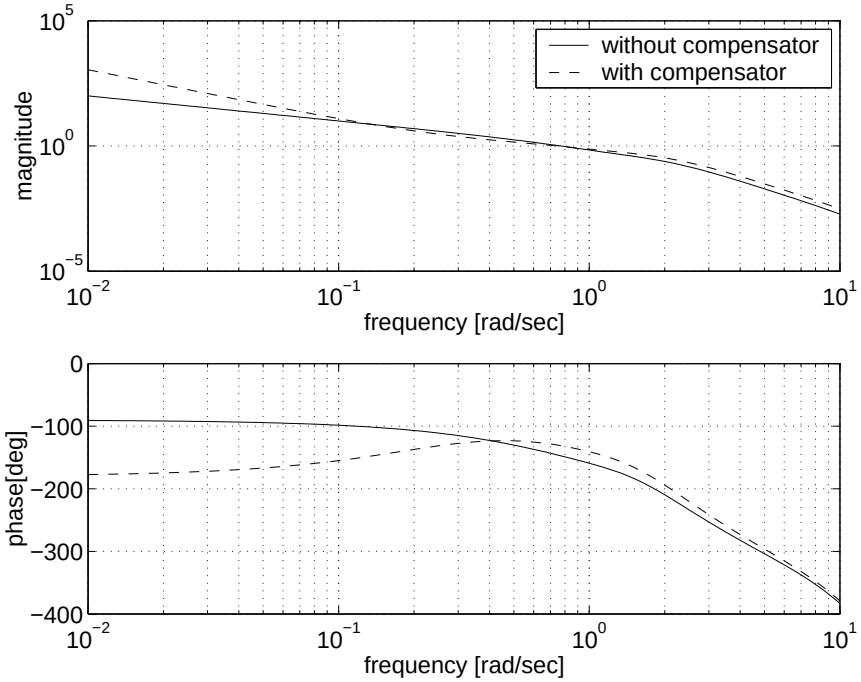

Figure C-5: Bode Plot for Altitude Controller Design

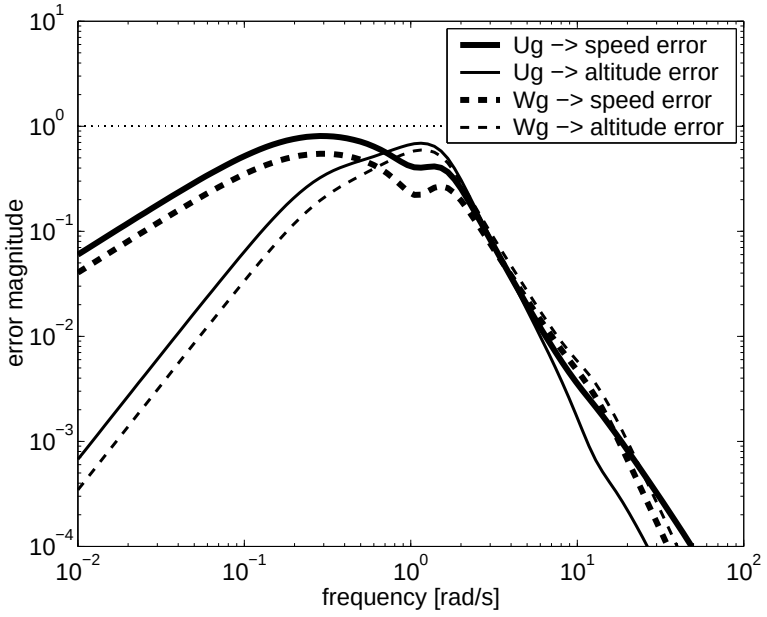

Figure C-6: Wind Disturbance Rejection of Longitudinal Controllers (Note - wind speed of $|U_g| = 5$ m/s , $|W_g| = 2.5$ m/s are used.)

banked at 30 degrees, then the wind component in the vehicle z-axis will be 2.5 m/s (=5 m/s $\times \sin 30^o$). The fact that the magnitudes of the associate transfer functions are less than unity in all the frequency range indicates that the aircraft will remain in the boundaries of 1 m and 1 m/s respectively under the 5 m/s of the wind condition.

A similar analysis was also performed on the OHS Parent vehicle. The procedure done for the Parent UAV was the same except that the effect of flexible tail section was also included for the OHS Parent vehicle. About 2 m of altitude error and 1 m/s of speed error boundaries were obtained under the same type of wind conditions.

Figure C-7 (a) shows the simulation for the command following for speed step reference change from 0 to 3 m/s while holding the altitude. It shows that the speed changes to 3 m/s with a rise time of 3 seconds while the altitude is maintained within ± 1 meter.

The plots in Figure C-7 (b) are for the simulation of step reference altitude command change from 0 to 5 m while holding the speed. To perform this command, the engine power is increased and the elevator is deflected upward initially, then they come back to their original position. The speed was held within the boundary between ± 1 m/s.

Figure C-8 (a) shows the simulation of the gust response with U_g=5 m/s. Plus sign denotes tail-wind. Speed does not exceed 0.6 m/s and altitude drop is less than 0.4 m. Figure C-8 (b) shows the simulation for downward gust W_g=2.5 m/s. Speed doesn't change more than 0.4 m/s and altitude doesn't drop more than 0.3 m

Flight test results regarding the longitudinal control are provided in Chapter 6.

C.3 Implementation of Smooth Transition and Anti-Windup

Smooth transition is important in switching back and forth between two different controllers or in the switching moment when computer control is engaged from pilot control mode. Anti-Windup capability is also important in the implementation of a control system. Under a saturation in control input under strong steady disturbance or a large set-point changes, the error is windup if there is an element of integral control, and will show a large control action even after the disturbance is removed or the set-point is reached.

Assume the control law can be expressed as

$$u = K_I e_I + K_{rest}(e_{rest})$$

where the integral control action is extracted. Also assume that there is an upper and lower

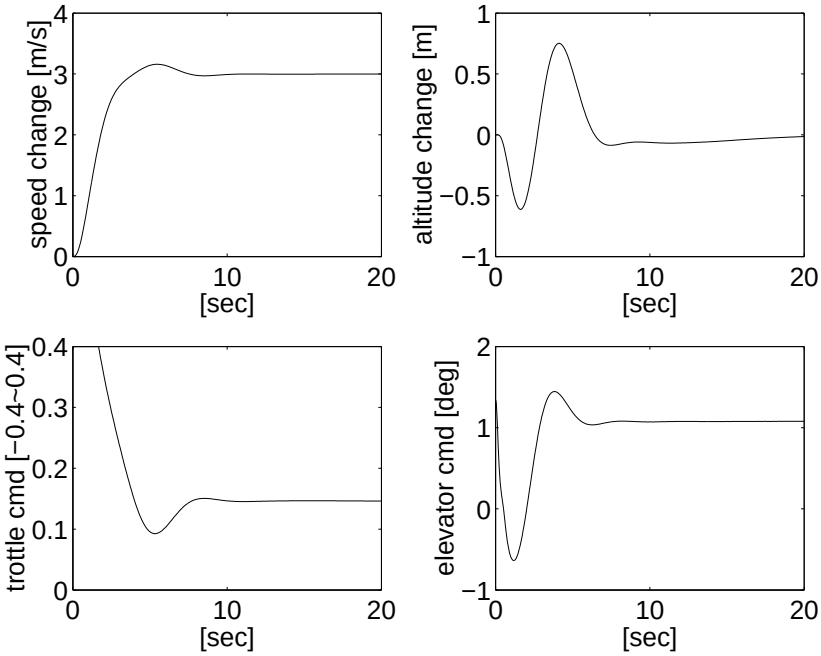

(a) speed change : 3 m/s

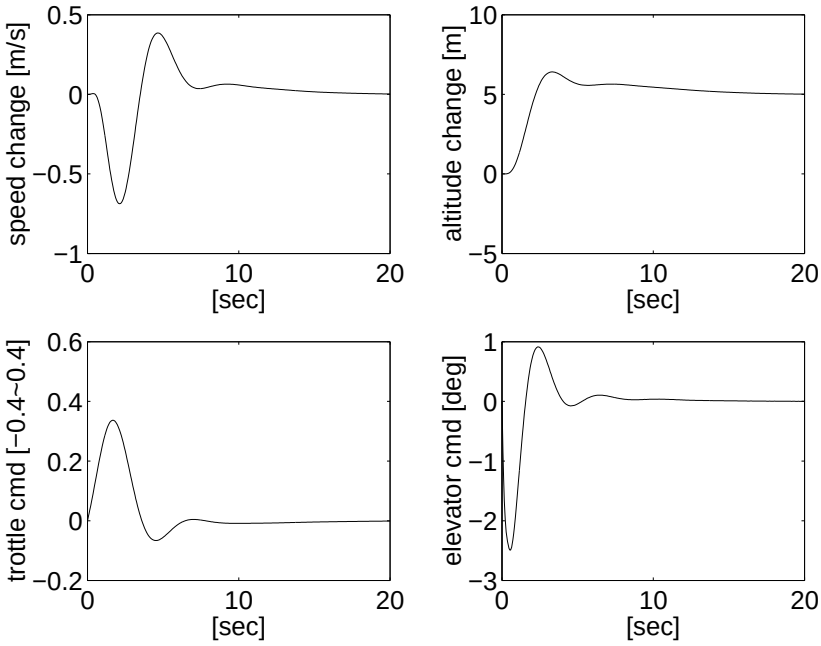

(b) altitude change : 5 m

Figure C-7: Longitudinal Controller Simulation for Command Following

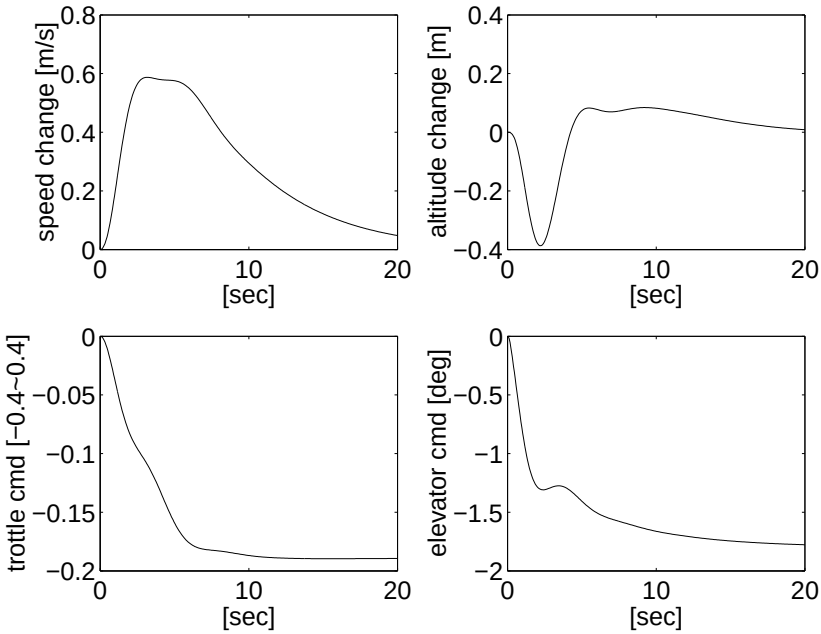

(a) tail-wind, U_g : 5 m/s

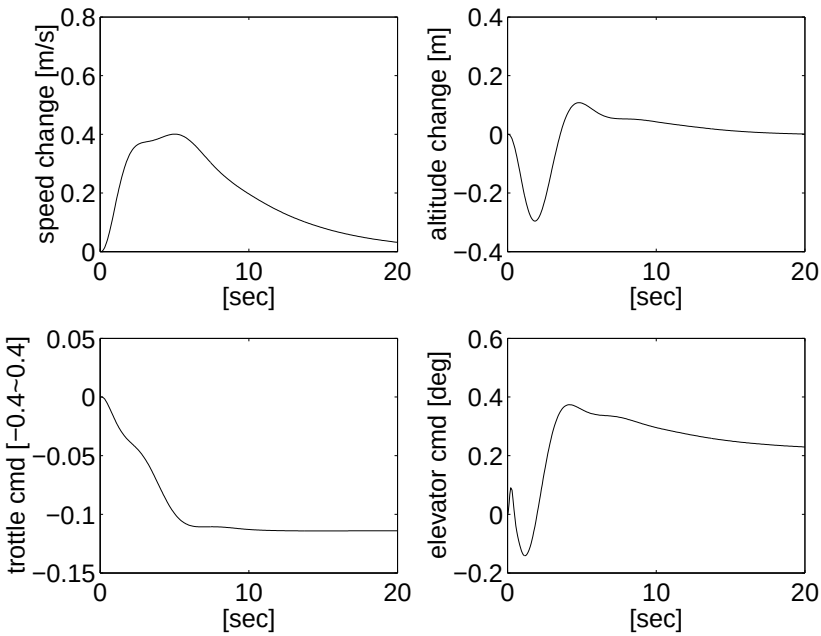

(b) down-wind, W_g : 2.5 m/s

Figure C-8: Longitudinal Controller Simulation for Wind Disturbance

limit in the control input u. Then, the logic used for smooth transition and anti-windup is outlined in the following steps [46, Gavrick].

At each control input computation

step 1 : compute

$$u = K_I e_I + K_{rest}(e_{rest})$$

step 2 : clip u if necessary between u_{max} and u_{min}. Let this value be $u_{clipped}$

step 3 : reset the integral variable e_I such that

$$\begin{aligned} K_I e_I + K_{rest}(e_{rest}) &= u_{clipped} \text{ for anti-windup} &&: e_I = K_I^{-1}(u_{clipped} - K_{rest}(e_{rest})) \\ \text{or} \quad &= u_{previous} \text{ for smooth transition} &&: e_I = K_I^{-1}(u_{previous} - K_{rest}(e_{rest})) \end{aligned}$$

step 4 : Control input is $u_{clipped}$ for anti-windup or $u_{previous}$ for smooth transition.

In words, for smooth transition, the integral variable is reset such that the control input doesn't change before and after the transition. For anti-windup the integral action is stopped when the control input reaches its saturation limit.

Appendix D

Other Estimation Filters

D.1 Estimation of Position/Velocity/Acceleration using GPS

A stand-alone GPS sensor gives both position and velocity information in north, east, and altitude directions. These two physical quantities are obtained by independent methods. The position is computed by combining more than 4 pseudo-ranges from the GPS satellites, and the velocity is measured by Doppler effect between the GPS receiver and the satellites. As noticed in Table A.1 in Section A.2, many GPS receivers provide high quality velocity information. The key idea of the filter introduced in this section is to use the high quality velocity measurement to improve the position estimates.

The other purpose of this filter is to obtain the unbiased acceleration estimates in the local inertial frame, which are combined in Chapter 4 with the rate gyros in removing the bias in the gyros.

Figure D-1 summarizes the Kalman filter [49, Zarchan & Musoff][14, Gelb] implemented for the GPS outputs in the north, east, and altitude directions. The three identical Kalman filters are used separately in each direction. The external inputs to this Kalman filter is the two GPS measurements - position and velocity. The filter dynamics is simply the kinematic relations between the position, velocity, acceleration, etc. It should be noticed that the order of the filter dynamics is extended to the fourth order, where up to the jerk, the derivative of the acceleration, is included as state variables. The reason for this is that in the airplane motion, the vehicle lateral acceleration is directly related with the bank angle. Consequently, the derivative of the acceleration, jerk, is related with the roll rate, which is correlated over time. Thus, it is appropriate to impose the process noise on the derivative

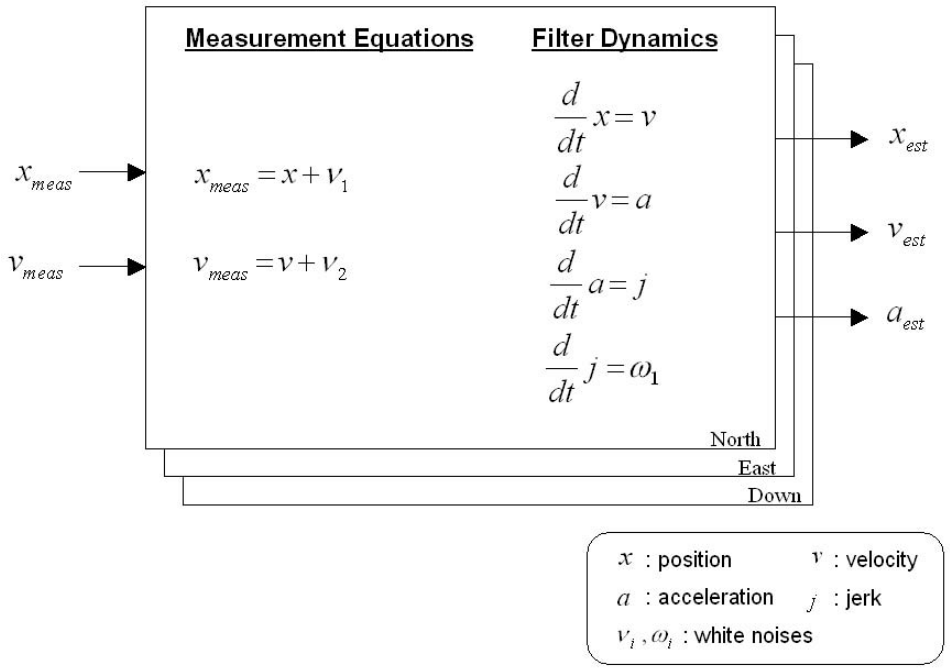

Figure D-1: Estimation of Position/Velocity/Acceleration using GPS

of the jerk.

The GPS Kalman filter designed above was tested with the pendulum test setup described in Section A.2. Figure D-2 shows the result where the pendulum was moved by a person in an oscillatory fashion rather regularly with the average frequency of about 0.4 Hz . The top graph in the figure shows the position data in altitude direction, where the position changes obtained from the potentiometer measurement, from the GPS raw output, and from the Kalman filter output are plotted together. A few observation can be made. First, there is about 0.4 seconds of delay in the GPS receiver itself which is seen by the comparison with the potentiometer data. Second, between the GPS raw data and the GPS Kalman filter estimates there is about 0.05 to 0.1 seconds of time delay. Lastly, a rather noisy GPS raw measurement is filtered smoothly by the Kalman filter. The middle graph shows the velocity from the GPS receiver and the Kalman filter. There is not a distinguishable difference between the two. The bottom plot shows the acceleration estimate from the Kalman filter. Since it is essentially the numerical differentiation of the GPS velocity information, this estimate is noisy.

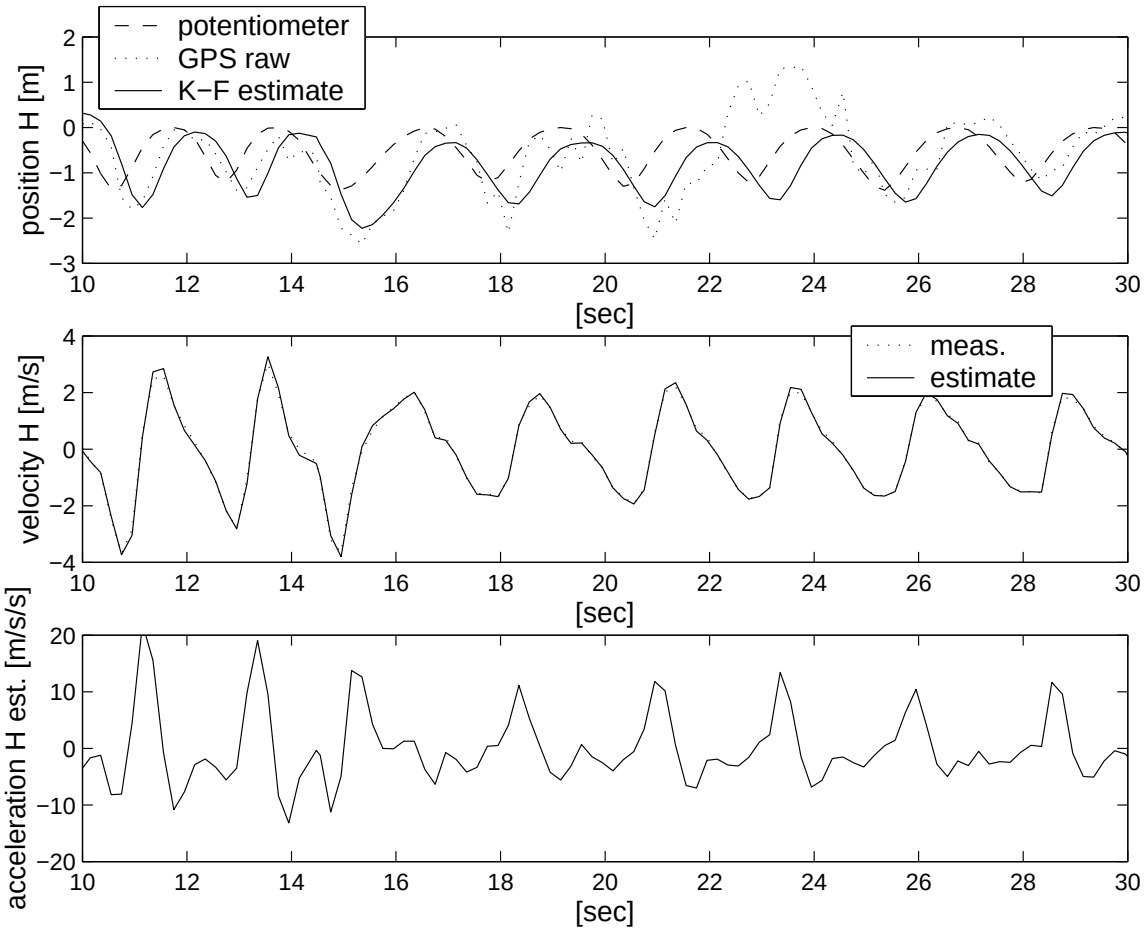

Figure D-2: GPS Kalman Filter with the Pendulum Setup

D.2 Estimation of Pitch Angle

Figure D-3 shows a complementary filter that was used for the estimation of pitch angle. The high frequency component is obtained by the pitch rate gyros with the bank angle correction. The relation $\dot{\theta} = q\cos\phi$ is an approximation that comes from one of the kinematic equations in Section B.2. The signal is integrated and high-pass-filtered to remove the drift associated with the integration. The low frequency component of the pitch angle is obtained by the gravity-aiding. It uses the property that the accelerometers are sensitive to gravity direction. The combination of the x and z axis accelerometers is used. Bank angle correction is also needed.

$$\theta = \tan^{-1}\left(-\frac{A_x}{A_z}\cos\phi\right) \qquad \text{at low frequencies}$$

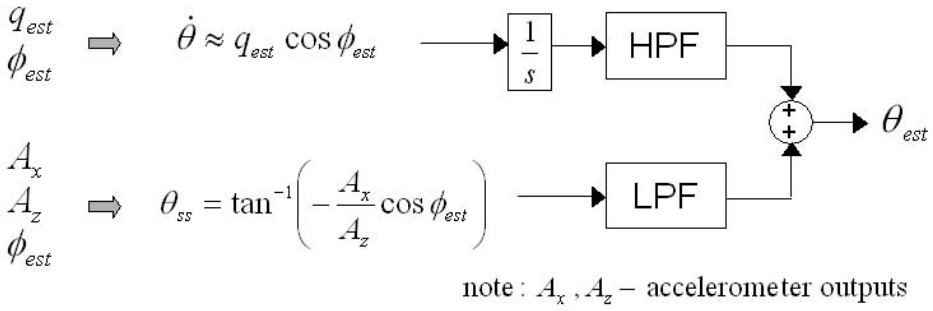

Figure D-3: Complementary Filter for Estimation of Pitch Angle

Here, A_x and A_z are accelerometer outputs. This signal is filtered with a low pass filter. The first order high and low pass filters were used in the complementary filter. The choice of the cutoff frequency is based on the vehicle dynamics and gyro performance. The 5 seconds of time constant was used.

D.3 Estimation of Altitude Rate and Altitude

GPS receiver gives an altitude and altitude rate information. But the chosen receiver has a pure time delay of about 0.4 seconds. The relation between the phase margin(PM) of a controller and the time delay with which the system can still remain stable is given in [44, Skogestad & Postlethwaite] by

$$delay = \frac{PM}{\omega_c}$$

where ω_c is the cutoff frequency of the loop transfer function. For PM=60 degrees($\approx$ 1 rad), and $\omega_c = 1\sim2$ rad/s, the maximum allowable time delay for stability is about 0.5$\sim$1.0 second. For this reason a faster estimation is recommended. To increase the bandwidth of the estimation of these variables the other sensors are combined to form complimentary filters.

Figure D-4 shows a complementary filter for altitude rate estimation. The low frequency part is estimated by the GPS receiver while the high frequency is mainly obtained from the accelerometers. First the vehicle body axis acceleration(a_x, a_y, a_z) is obtained from the accelerometers and gravity correction. Then an angular transform is performed to get the acceleration component in the altitude direction. This signal is integrated and high pass filtered. The time constant of the two filters should be larger than the GPS sensor delay.

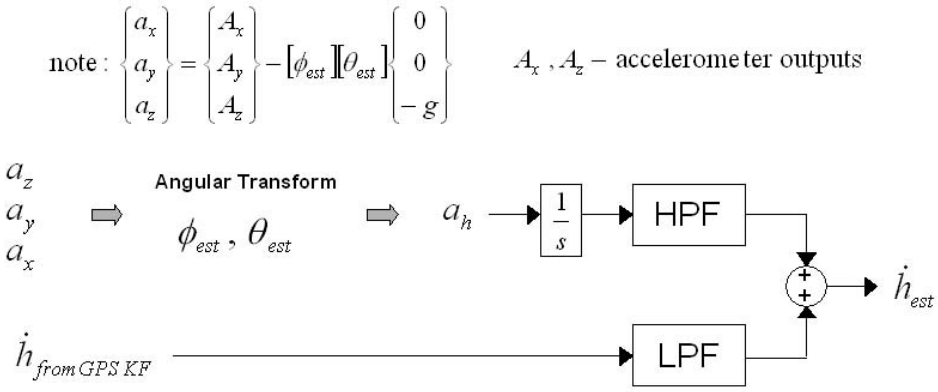

Figure D-4: Complementary Filter for Estimation of Altitude Rate

But it shouldn't be too large. Otherwise the noise from the accelerometer leaks through. The time constant of 3.0 second was used.

Due to the same reason of the GPS receiver delay, altitude estimation is augmented with the altitude pressure sensor. Figure D-5 shows the associated complementary filter, where the low frequency comes from the GPS and the high frequency from the pressure sensor.

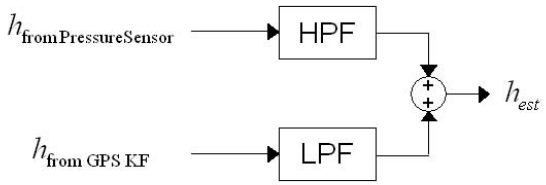

Figure D-5: Complementary Filter for Estimation of Altitude

D.4 Estimation of Angle of Attack

The angle of attack is required in the longitudinal LQR controller. A simple way was used. The angle of attack is related with the z-axis accelerometer output. By the equation

$$a_z = -\frac{\bar{q}S}{m}\left\{C_{L_\alpha}\alpha + C_{L_q}\frac{\bar{c}}{2V_1}q + C_{L_{\delta_e}}\delta_e\right\}$$

obtained in the linearized dynamics, the angle of attack was derived.

Appendix E

Line-of-Sight Rate Computation

This section describes how the line-of-sight rate is estimated using the optical sensor and other onboard estimates. Figure E-1 shows the definitions of some angles required to derive line-of-sight rates, $\dot{\lambda_s}$, $\dot{\lambda_h}$. The direct outputs of the optical sensor are angles to the target.

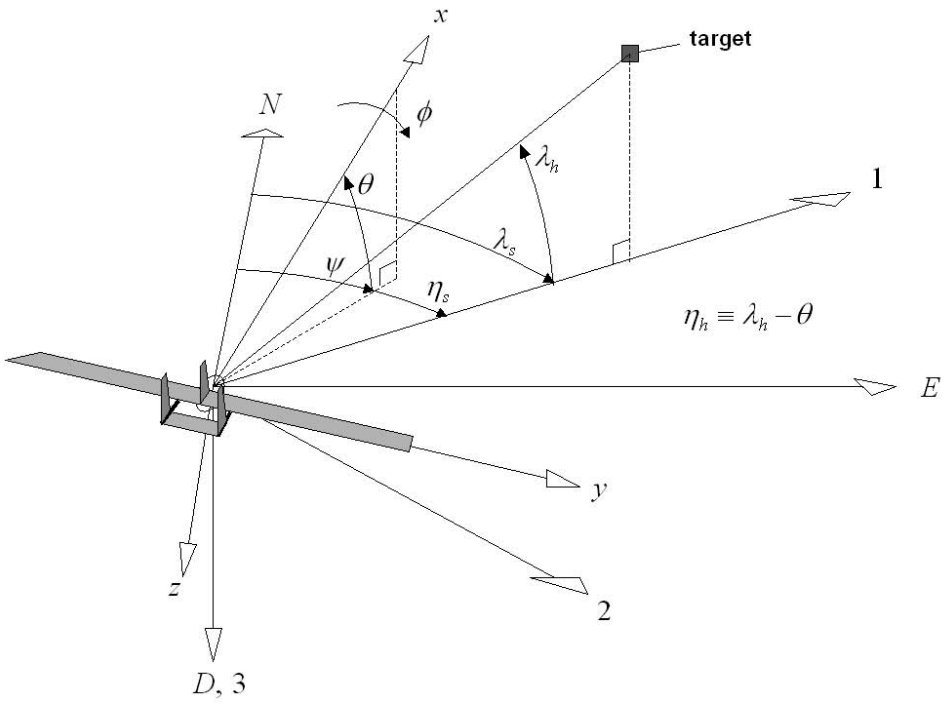

Figure E-1: Definition of Angles Regarding Phase II Optical Sensor Aided Proportional Navigation (Note - λ_s, λ_h: LOS angles, η_s, η_h: angles to target, the outputs of optical sensor, ϕ, θ, ψ: Euler angles of the Mini vehicle)

In order to get line-of-sight-rates referenced to inertial frame, the following steps need to be

followed. It is assumed here that the camera is mounted exactly aligned with the vehicle body axis.

Step 1 :

From the optical sensor outputs, a unit vector($\vec{\mu}$) pointing to the target from the camera can be considered. This unit vector is coordinatized into vehicle body axis (x,y,z) in Figure E-2. At the next sampling step, a new unit vector, $\vec{\mu}_{new}$ is obtained and it is discretely

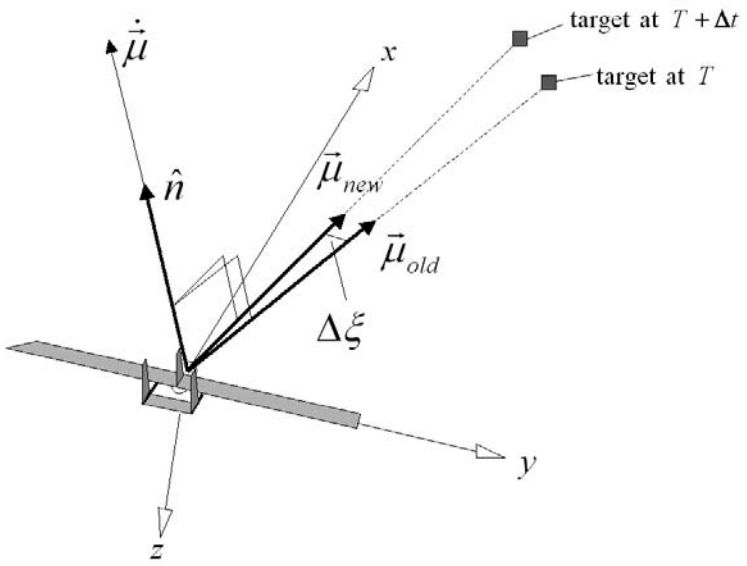

Figure E-2: Definition of Angles Regarding the Optical Sensor Output. (Note : $\vec{\mu}$ is a unit vector pointing to target. $\hat{n}$ is also a unit vector perpendicular to $\vec{\mu}_{old}$ and $\vec{\mu}_{new}$.)

differentiated to get the angular rate, $\dot{\vec{\mu}}$, which is still coordinatized into the x,y,z vehicle body frame.

$$\dot{\vec{\mu}} = \frac{\Delta\xi}{\Delta t}\hat{n}$$

where

$$\hat{n} = \frac{\vec{\mu}_{old} \times \vec{\mu}_{new}}{|\vec{\mu}_{old} \times \vec{\mu}_{new}|}$$

and

$$\Delta\xi = \arccos(\vec{\mu}_{old} \cdot \vec{\mu}_{new})$$

Thus,

$$\dot{\vec{\mu}} = \frac{\arccos(\vec{\mu}_{old} \cdot \vec{\mu}_{new})}{\Delta t} \cdot \frac{\vec{\mu}_{old} \times \vec{\mu}_{new}}{|\vec{\mu}_{old} \times \vec{\mu}_{new}|}$$

Step 2 :

The angular rotation of the aircraft should be compensated using the angular rate estimates. The line-of-sight rate coordinatized into the body frame is obtained.

$$\left\{\dot{\vec{\lambda}}\right\}_{x,y,z} = \dot{\vec{\mu}} + \begin{Bmatrix} P \\ Q \\ R \end{Bmatrix}$$

Step 3 :

Finally, the angular transformation, $[\phi]^{-1} \rightarrow [\theta]^{-1} \rightarrow [\eta_s]$ gives $\dot{\lambda}_h$ and $\dot{\lambda}_s$.

$$\left\{\dot{\vec{\lambda}}\right\}_{1,2,3} = [\eta_s][\theta]^{-1}[\phi]^{-1}\left\{\dot{\vec{\lambda}}\right\}_{x,y,z}$$

and

$$\dot{\lambda}_h = \left\{\dot{\vec{\lambda}}\right\}_2, \ \dot{\lambda}_s = \left\{\dot{\vec{\lambda}}\right\}_3$$

Computation of Angles to Target, $\eta_s,\ \eta_h$ for Simulation

This section gives the relations needed to compute the outputs of the optical sensor, η_s and η_h which is used in simulations. Let $\vec{r}$ be a relative position vector from the Mini's camera to the Parent's light source, and in local inertial frame it is

$$\{\vec{r}\}_{NED} = [\ r_N \quad r_E \quad r_D\ ]^T$$

Then, from Figure 5-8 LOS angles are given by

$$\lambda_h = \tan^{-1}\left(-\frac{r_D}{\sqrt{r_N^2 + r_E^2}}\right), \quad \lambda_s = \tan^{-1}\left(\frac{r_E}{r_N}\right)$$

Then, the angles to the target are obtained by

$$\eta_h = \lambda_h - \theta, \quad \eta_s = \lambda_s - \psi$$

If the camera is mounted pointing-up or pointing-down by θ_{camera}, it should be added to the vehicle pitch angle.

Appendix F

Flight Data - Phase I Trajectories

Two sets of Phase I flight tests were performed on 25 July 2002. The result of the first set is shown in Figure 6-5 and 6-6 in Section 6.2. The flight trajectories of the two vehicles in the second set of the Phase I flight test are shown in Figure F-1 and F-2. Again, the series of the plots show the position of the OHS Parent vehicle in letter 'O' and that of the Mini vehicle in letter 'M' on the east-north 2 dimensional map at every 10 seconds. In the plots, the three straight lines of the Parent flight path near the circle in the left side of the map are due to the communication loss from the Parent to the Mini. The plots show the positions of both Mini and OHS Parent stored in the disk space of the Mini onboard computer. In the presence of the communication loss the planning algorithm and the combined control system are robust enough to achieve the required synchronization when the two vehicles join on the circle at around 100 [sec]. The actual autonomous flight lasted longer than is shown in the figures. The two vehicle configured a formation flight while they were following the circle path together with a specified separation command.

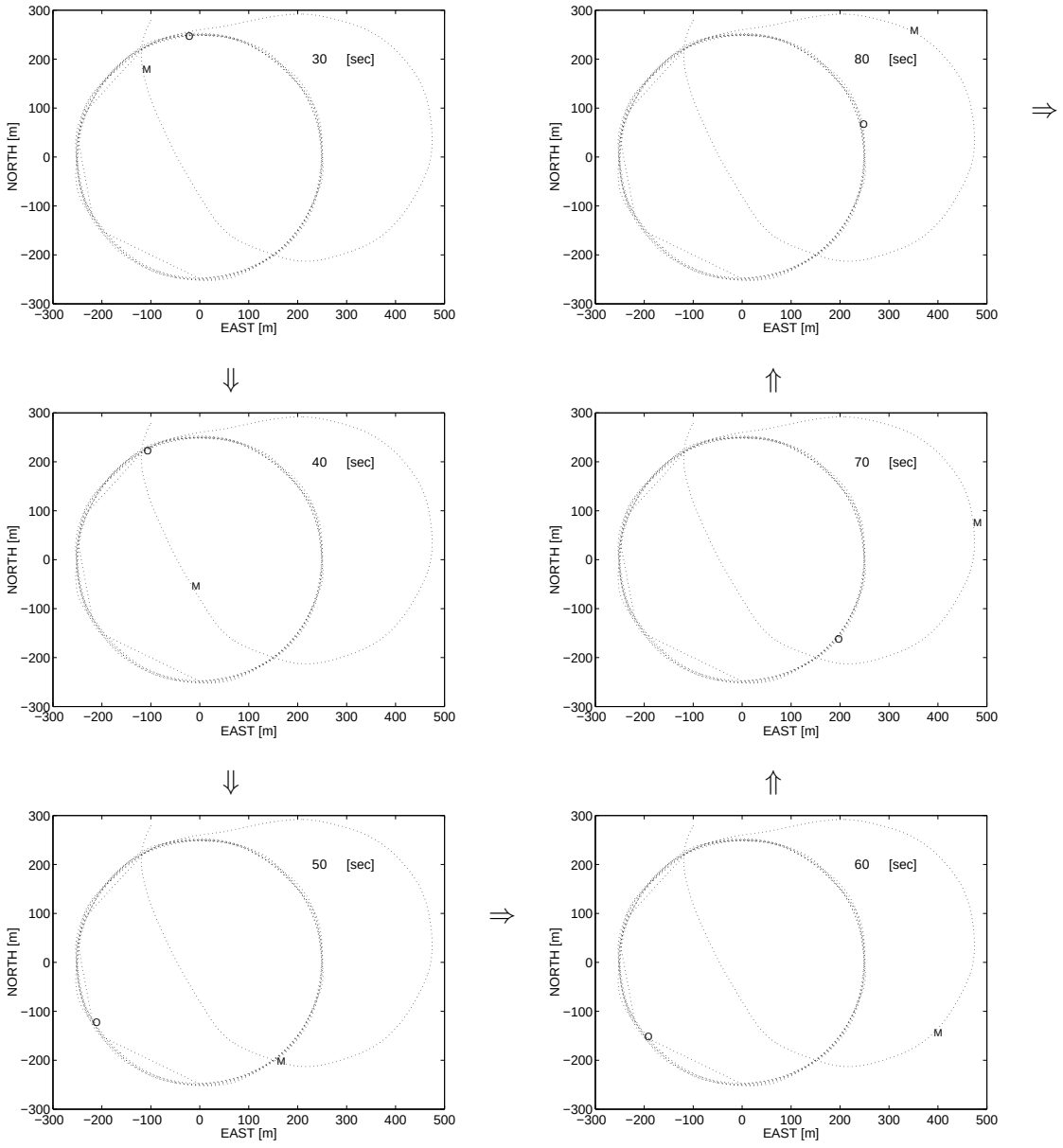

Figure F-1: Flight Data - Phase I Trajectories of OHS and Mini (O:OHS, M:Mini)

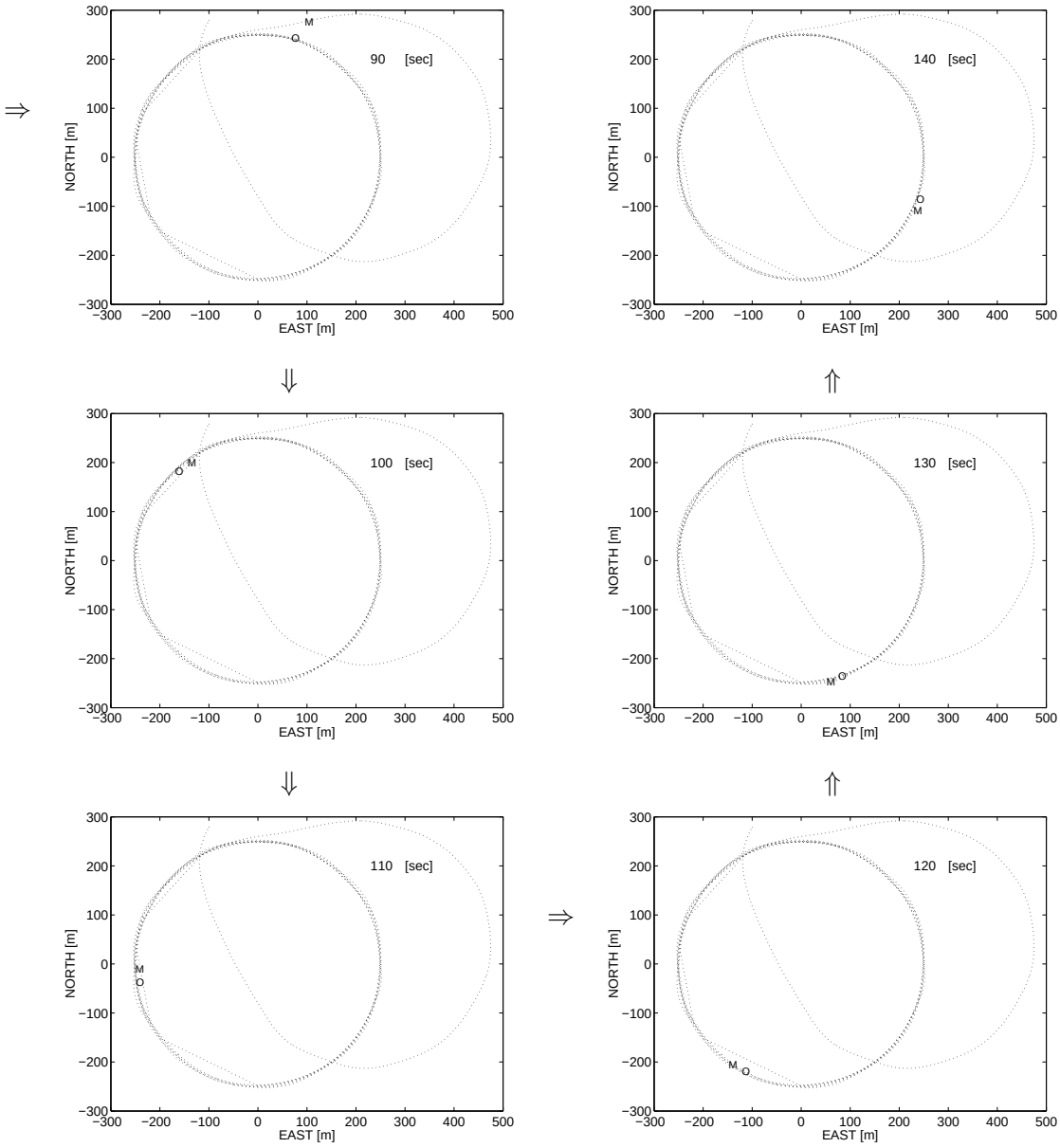

Figure F-2: Flight Data(cont'd) - Phase I Trajectories of OHS and Mini (O:OHS, M:Mini)

Bibliography

[1] Pcuav web page, http://web.mit.edu/aeroastro/pcuav/.

[2] Jr. Arthur E. Bryson. *Control of Spacecraft and Aircraft*. Princeton University Press, 1994.

[3] Astrom and Wittenmark. *Computer Controlled Systems - Theroy and Design*. Prentice Hall, 1997.

[4] John H. Blakelock. *Automatic Control of Aircraft and Missiles*. Wiley-Interscience, 1991.

[5] Frank L. Lewis Brian L. Stevens. *Aircraft Control and Simulation*. A Wiley-Interscience Publication, 1992.

[6] A.E. Bryson. Optimal programming problems with inequality constraints i: Necessary conditions for external solutions. *AIAA Journal*, pages 2544–2550, Nov. 1963.

[7] Averil B. Chatfield. *Fundamentals of High Accuracy Inertial Navigation*, volume 174. Progress in Astronautics and Aeronautics, 1997.

[8] J. Clemow. *Missile Guidance*. Temple Press Unlimited, London, 1960.

[9] C.E. Cohen. *Attitude Determination, GPS:Theory and Application, ed Parkinson and Spilker*, volume 163. AIAA Progress in Astronautics and Aeronatuics, 1996.

[10] Louis L. Whitcomb David A. Smallwood. Toward model based trajectory tracking of underwater robotic vehicle: Theory and simulation. *In Proceedings of IEEE/MTS Oceans*, pages 1106–1114, November 2001.

[11] Mark Drela. 16.110 - flight vehicle aerodynamics. MIT, 2002. Lecture Notes.

[12] Eric Corban Eric Johnson, Anthony Calise. A six degree-of-freedom adaptive flight control architecture for trajectory following. *AIAA Guidance, Navigation, and Control Conference and Exhibit*, (AIAA-2002-4776), 2002.

[13] Meir Pachter Gano B. Chatterji. Modified velocity pursuit guidance law with crosswind correction for missile against surface targets. *AIAA Guidance and Control Conference*, pages 1566–1571, 1991.

[14] Arthur Gelb. *Applied Optimal Estimation*. MIT Press, 1974.

[15] M. Guelman. Guidance of asteroid rendezvous. *Journal of Guidance*, 14(5):1080–1083, 1991.

[16] M.E. Warren H.L. Pastirck, S.M. Seltzer. Guidance laws for short-range tactical missiles. *Journal of Guidance and Control*, 4(2):98–108, 1981.

[17] V.A. Yakubovich I.A. Makarov, I.E. Zuber. *The Trajectory Tracking Problem for Autonomous Steering and Related Topics*, volume 2 of *TRANSACTIONS*. French-Russian A.M. Liapunov Institute for Applied Mathematics and Computer Science, Moscow, Russia, 2001.

[18] Antonio Pascoal Carlos Silvestre Isaac Kaminer, Eric Hallberg. Trajectory tracking for autonomous vehicles: An integrated approach to guidance and control. (AIAA-97-3625), 1997.

[19] D.J. Yost J.E. Kain. Command to line-of-sight guidance: A stochastic optimal contorl problem. *Journal of Spacecraft*, 14(7):438–444, 1977.

[20] D.L. Jensen. Kinematics of rendezvous maneuvers. *Journal of Guidance*, 7(3):307–314, 1984.

[21] Jr. John D. Anderson. *Fundamentals of Aerodynamics, 2nd ed.* McGraw-Hill, Maryland, 1991.

[22] Charles F. Price John J. Deyst. Optimal stochastic guidance laws for tactical missiles. *Journal of Spacecraft*, 10(5), 1973.

[23] Van Olinger John Kinzer. Naval ucav update. *Assoication of Unmannd Vehicle Systems International Conference*, July 2003.

[24] Damien Jourdan. Trajectory design and vehicle guidance for a mid-air rendezvous between two autonomous aircraft. Master dissertation, MIT, Department of Aero/Astro, Feb 2003.

[25] J.A.C Kentfield. Upwash flowfields at the tails and aircraft with outboard horizontal stabilizers. *Conference Paper, AIAA 98-0757*, Jan 1998.

[26] Jason Kepler. Parent child unmanned aerial vehicles and the structural dynamics of an outboard horizontal stabilizer aircraft. Master dissertation, MIT, Department of Aero/Astro, jun 2002.

[27] Tamas Keviczky and Gary J. Balas. Software enabled flight control using receding horizon techniques. *AIAA Guidance, Navigation, and Control Conference and Exhibit*, (AIAA2003-5671), August 2003.

[28] Richard P. Kornfeld. *The Impact of GPS Velocity Based Flight Control on Flight Instrumentation Architecture*. Ph.D dissertation, MIT, June 1999.

[29] Eugene Lavretsky. F/a-18 autonomous formation flight control system design. *AIAA Guidance, Navigation, and Control Conference and Exhibit*, August 2002.

[30] A.S. Locke. *Guidance*. D. Van Nostrand Co., Princeton, 1955. Chap.12.

[31] Andrew Luers. Flow control techniques in a serpentine inlet: An enabling technology to increase the military viability of unmanned air vehicles. Master's thesis, MIT, 2003.

[32] Jason Mukherjee. *Automatic Control of an OHS Aircraft*. Ph.D dissertation, University of Calgary, 2000.

[33] Richard M. Murray. Trajectory generation for a towed cable system using differential flatness. *IFAC World Congress*, 1996.

[34] Richard M. Murray Muruhan Rathinam. Configuration flatness of lagrangian systems underactuated by one control. *Control and Decision Conference*, 1996.

[35] Marius Niculescu. Lateral track control law for aerosonde uav. *33th AIAA Aerospace Sciences Meeting and Exhibit*, (AIAA 2001-0016), Jan 2001.

[36] Michael Bosse Paul DeBitetto, Christian Trott. The draper laboratory small autonmous aerial vehicle. *AIAA/IEEE Digital Avionics Systems Conference*, 1996.

[37] Shih-Che Hsu Pin-Jar Yuan. Rendezvous guidance with proportional navigation. *Journal of Guidance*, 17(2):409–411, 1994.

[38] Richard Poutrel. Global positioning system navigation and digital communications for cooperating unmanned air vehicles. Master dissertation, MIT, Department of Aero/Astro, jun 2002.

[39] Daniel P. Raymer. *Aircraft Design: A Conceptual Approach*. AIAA Education Series, Washington, D.C, 1989.

[40] R.W. Rishel. Optimal terminal guidance of an air to surface missile. *AIAA Guidance, Control and Flight Dynamics Conference*, (67-580), Aug. 1967.

[41] R. Rogers. *Applied mathematics in integrated navigation systems*. AIAA Education Series, 2000.

[42] Jan Roskam. *Airplane Flight Dynamics and Automatic Flight Controls*. Roskam Aviation and Engineering Corporation, Kansas, 1979.

[43] N.A. Shneydor. *Missile Guidance and Pursuit - Kinematics, Dynamics and Control*. Horwood Publishing Limited, 1998.

[44] Sigurd Skogestad and Ian Postlethwaite. *Multivariable Feedback Control - Analysis and Design*. Wiley, 1996.

[45] Francois Urbain. Vehicle design, flight control avionics design, and flight test for the parent child unmanned aerial vehicle. Master dissertation, MIT, Department of Aero/Astro, Jun 2001.

[46] B. Mettler V. Gavrilets, I. Martinos and E. Feron. Control logic for automated aerobatic flight of miniature helicopter. *AIAA Guidance, Navigation and Control Conference, Monterey, CA*, August 2002.

[47] Brain Whalley. The nasa/army autonomous rotorcraft project. *American Helicopter Society 59th Annual Forum*, 2003.

[48] Paul Zarchan. *Tactical and Strategic Missile Guidance*, volume 176 of *Progress in Astronautics and Aeronautics*. AIAA, third edition edition, 1997.

[49] Paul Zarchan and Howard Musoff. *Fundamentals of Kalman Filtering - A Practical Approach*, volume 190 of *Progress in Astronautics and Aeronautics*. AIAA, 2000.

[50] Kemin Zhou. *Essentials of Robust Control*. Prentice Hall, 1998.